Coalescence, clustering, and chaotic stirring: The role of Lagrangian coherent structures in the mixing and unmixing of scalars.

by

K.R. Pratt

B.S., The Pennsylvania State University, 2010

M.S., The Pennsylvania State University, 2012

A thesis submitted to the

Faculty of the Graduate School of the

University of Colorado in partial fulfillment

of the requirements for the degree of

Doctor of Philosophy

Department of Civil Engineering

2016

This thesis entitled:
Coalescence, clustering, and chaotic stirring: The role of Lagrangian coherent structures in the mixing and unmixing of scalars.
written by K.R. Pratt
has been approved for the Department of Civil Engineering

_____
Prof. John Crimaldi

_____
Prof. James Meiss

_____
Prof. Roseanna Neupauer

_____
Prof. Peter Hamlington

_____
Prof. Harihar Rajaram

Date _____

The final copy of this thesis has been examined by the signatories, and we find that both the content and the form meet acceptable presentation standards of scholarly work in the above mentioned discipline.

Pratt, K.R. (Ph.D., Civil, Environmental, and Architectural Engineering)

Coalescence, clustering, and chaotic stirring: The role of Lagrangian coherent structures in the mixing and unmixing of scalars.

Thesis directed by Prof. John Crimaldi

Turbulent flows are renowned for their ability to efficiently dilute scalars due to rapid mixing. The structure of turbulent flows that leads to efficient mixing, however, has also been shown to organize scalars in specific regions of the flow. Due to structured stirring, initially distant reactive scalars that are separated by a third non-reactive fluid have been shown to organize in regions at times shorter than that required for dilution, leading to reaction enhancement. This thesis examines the coalescence of initially distant scalars using numerics, analytics, and experiments to infer the role that Lagrangian coherent structures (LCS) play in the coalescence process. In addition, scalar coalescence and clustering on an effectively compressible free-surface (such as the surface of the ocean) is examined to quantify whether non-divergence-free effects increase the likelihood of reaction enhancement. We show that LCS are responsible for coalescence in incompressible flows due to coherent stretching that attracts distant filaments. In non-divergence-free flows, the LCS has an additional dilatation component that 1) facilitates the coalescence process, which increases the likelihood of reaction enhancement, and 2) leads to the formation of clusters from initially well-mixed scalars. The instantaneous structure of turbulent flows, whether in an incompressible or compressible environment, is essential in facilitating the coalescence of initially distant scalars, which leads to reaction rates that can far exceed those from random diffusive mixing.

Dedication

Twelve years ago, for my 17th birthday, a friend gave me "The Essence of Chaos" by Edward Lorenz. From that moment on, the butterfly effect captured my imagination. To this day, that book sits on my desk, a reminder of how small life events can lead to such unimaginable places. To think of all the people, all the chance encounters, the strokes of luck and misfortune, that led me to where I am today. In the midst of random chance, however, there are those that have guided me, a lighthouse in the sea of chance. This thesis is dedicated to those people. To all the teachers and professors that inspired me along the way. For showing me the beauty of scientific ideas, of mathematics, of music, of stories, of art. To my adviser, John Crimaldi, for believing in me all those years ago when you hired a meteorology student with no engineering experience. Over the previous 4 years, you have taught me how to be a scientist, to be rigorous and observant. This thesis is your brainchild; I hope it makes you proud. To Katie, for all of the memories of the previous 7 years. Your strength has kept me going, when all I wanted to do was fall. Together, we can do anything. To my older brother, whose constant tinkering taught me one of the most important traits I possess as a scientist today, the ability to tinker without fear of failure. To my younger sister, for keeping your older brothers grounded, lest we get too big of a head. To my mom and dad, who gave everything to ensure that their children would live a better life than they did. You used what little money you had to send me to college, so that I could pursue my dreams, in effect putting your dreams on hold. The fact that the child of blue-collar parents with no college education has reached the pinnacle of higher education is a testament to you. This thesis is your thesis.

Acknowledgements

The ideas and work in this thesis are the product of so many people that graciously gave their time. First and foremost, my advisor, John Crimaldi. John was involved in every step of the scientific process, from formation of ideas to presentation. This thesis would look very different without him. I would also like the thank all of the collaborators who made our work better. Thank you to Jim Meiss for his insights on LCS and chaotic mixing, and all of the work that he put into our LCS paper (Chapter 3 of this thesis). Thank you to Aaron True, for solidifying the experimental portion of our clustering paper (Chapter 4) by helping with PIV. I couldn't have done it without you. Thank you to Miguel Calpe for helping to code, wire and setup the turbulence tank. The work you did was impressive, and I cannot thank you enough.

Thank you to my committee; Peter Hamlington, Hari Rajaram, Roseanna Neupauer, and Jim Meiss. Thanks for taking the time to serve on my committee and for all of your helpful guidance.

Contents

Chapter

Tables

Table

Figures

Figure

Chapter 1

Introduction

> At present I absolutely want to paint a starry sky. It often seems to me that night is still more richly coloured than the day; having hues of the most intense violets, blues and greens. If only you pay attention to it you will see that certain stars are lemon-yellow, others pink or a green, blue and forget-me-not brilliance. And without my expatiating on this theme it is obvious that putting little white dots on the blue-black is not enough to paint a starry sky.
>
> -Vincent Van Gogh

Anyone that has ever looked at a field of wheat blowing in the wind understands that turbulence has structure. Living near the wheat fields of Provence in the south of France during the height of his career, Van Gogh understood this more than anyone at the time. What he observed in the waving fields of wheat, he envisioned in the night sky above him. In his quest to reproduce the essential components of nature, it was the structure of the world around him that mattered most. This is a thesis about structure.

In the chapters that follow, we discuss the structure of turbulent flows and why this structure is important for the transport of scalars. Much of this thesis is focused on the transport and reaction of initially distant scalars. In this scalar topology, two reactive scalars are separated by a third non-reactive fluid, and in order for reactions to occur, fluid stirring must bring these distant scalars together. This is a process we refer to as the *coalescence* of initially distant scalars. In turbulent flows, concentrations are decaying at an exponential rate due to chaotic stirring. Therefore, as coalescence processes are occurring, concentrations can vary dramatically depending upon the time that it takes for filaments to coalesce. Turbulence is often viewed as a random

collection of eddies where chaotic stirring leads to the efficient dilution of scalars. In this view, coalescence will eventually occur between initially distant scalars due to random mixing. **The main hypothesis of this thesis is as follows: Turbulent flows, known for their ability to efficiently dilute scalars, have the competing effect of organizing initially distant scalars at timescales shorter than that required for dilution, leading to reaction enhancement**.

This thesis did not start as a blank canvas. Over the previous decade, the Crimaldi group has been investigating the coalescence of initially distant scalars. In 2004, Crimaldi and Browning [1] used coral broadcast spawning as a model problem to motivate the idea of structured stirring. Convenential thought looked at turbulence as a hinderance to broadcast spawning because of its ability to quickly dilute concentrations of egg and sperm. Crimaldi and Browning's hypothesis was that while turbulence diluted scalars in the long term, it also allowed for the coalescence of scalars in the short term. Using analytics and simple numerical vortex flows, they showed that the instantaneous stirring processes were essential in bringing high concentration filaments together, resulting in enhanced reaction rates compared to a time-averaged plume that lacked structure. Four years later, Crimaldi et al. [2] expanded upon the prior work by looking at the effect of Peclet number on the ability of vortex induced stirring to bring distant filaments together. They found that peak reaction rates increased as $Pe^{1/3}$. In addition, the time to reach the peak reaction decreased as $Pe^{-2/3}$.

In 2011, Soltys and Crimaldi [3] developed a novel experimental method to observe the coalescence of two intially distant scalars. This method was used in Soltys and Crimaldi (2015) [4] to study the mixing of two isolated scalars being released from parallel jets. They found that structured stirring within the turbulent jets led to positive scalar covariances downstream as the distant filaments were drawn towards attracting regions in the flow; positive scalar covariances are indicative of scalar coalescence. In 2014, Crimaldi and Kawakami studied reaction enhancement downstream of a stationary cylinder using DNS. Two scalars were released continuously into the flow upstream of the cylinder and began to coalesce in the downstream wake. The presence of the cylinder greatly enhanced reaction rates compared to scenarios where the cylinder was not present due to structured

Table 1.1: Variety of techniques used in the thesis.

	Chapter 2	Chapter 3	Chapter 4	Chapter 5
Numerical	X	X	X	X
Experimental			X	
Analytical	X	X		X
Scalar Topology	Initially Distant	Initially Distant	Well-Mixed	Initially Distant
Flow	-	Incompressible	Compressible	Compressible

stirring occurring in the shed vortices downstream of the cylinder. Experiments were also performed downstream of a stationary cylinder using the two-color PLIF technique developed by Soltys and Crimaldi. Results confirmed the numerical study that the presence of a cylinder greatly enhances reaction rates compared to the no cylinder case.

Throughout this thesis, a variety of techniques are used to evaluate the importance of structured stirring; including numerics, experiments, and analytics. Bernard Avishai once said, "The danger from computers is not that they will eventually get as smart as men, but we will meanwhile agree to meet them halfway." To avoid this pitfall, this thesis attempts to combine theory, computation, and experiment in order to arrive at conclusions that are as sound as possible. The techniques used in each chapter are broken down in Table 1.1.

In Chapter 2, we begin with the most basic case of coalescence of initially distant scalars via the process of diffusion. In diffusion, there is no structure that organizes the coalescence of scalars as they dilute. It is simply overlap through random mixing. Therefore, the extent of reaction enhancement will be solely determined by the distance separating the scalars.

In Chapter 3, we discuss the coalescence of scalars due to structured stirring in a chaotic flow. This chapter will focus on Lagrangian coherent structures (LCS) and how they facilitate the coalescence of initially distant scalars for a variety of chaotic flows. In the case of scalar dispersion, we show that the Lagrangian frame of reference, a frame of reference that moves with the fluid parcels, is the ideal way to view turbulent structure. Oftentimes, the word eddy is used to invoke turbulence structure, with turbulence being viewed as a collection of rotating eddies of different sizes that interact with one another in a complex manner. The structures that are seen in waving

wheat, for example, are eddies that sweep along the plant canopy and bend the stalks of wheat as they pass. This view of eddies is inherently Eulerian in nature, as their structure is based on what the velocity field looks like at one instant of time. For scalars that are being advected through a turbulent flow, however, an Eulerian structure has little meaning, as the time history of stretching and folding must be accounted for.

In Chapter 4, we focus on the behavior of scalars that float on the surface of a three-dimensional fluid, such as the free-surface of the ocean. Scalars that are buoyant are forced to stay on the free-surface and are therefore exposed to an effectively compressible velocity field. This compressible velocity field allows for initially well-mixed scalars to suddenly unmix and *cluster*, a reversal of the typical arrow of time in which turbulence acts to mix scalars. In this chapter, we will examine the role of LCS in the unmixing of initially well-mixed scalars using both experiments and numerics.

In Chapter 5, we discuss how non-divergence-free behavior on a free-surface effects the likelihood of scalar coalescence for scalars that were initially distant. The dilatation component of the LCS that is responsible for *clustering* also influences the *coalescence* of initially distant scalars. The final chapter will tie the thesis together, and compare the likelihoods of reaction enhancements for diffusion, turbulent stirring, and turbulent stirring in non-divergence-free flows. The goal of this thesis is to convince the reader that the structure of turbulent flows should not be treated as collection of eddies that interact in a random manner. Rather, turbulence has an inherent structure that leads to order.

Chapter 2

Diffusion as a Means of Scalar Coalescence

2.1 Turbulent Diffusion of a 2D Point Source

In order to appreciate why instantaneous structure is important for scalar coalescence, we must first understand what this coalescence looks like in a world without structure, what Van Gogh would call "little white dots on the blue-black", where the random shuffling of diffusion reigns. Turbulence is renowned for its ability to quickly dilute initially strong concentrations of scalars. Observe the whisps of smoke emanating from the tip of a cigarette, and this will be made clear. Oftentimes, the complex spatial and temporal structures of the instantaneous flow are neglected and transport is treated as a diffusion process. In this implementation, the molecular diffusivity is simply replaced with a turbulent diffusivity that is many orders of magnitude larger. The dilution of a 2D point source, for instance, can be represented as

$$C_1(x, y, t) = \frac{M}{4\pi D_t t} \exp\left(\frac{-x^2}{4D_t t} - \frac{y^2}{4D_t t}\right), \tag{2.1}$$

where C_1 is the concentration of the scalar, M is the mass, D_t is the turbulent diffusivity, t is time, and x, y are spatial dimensions. In this structure-less world, concentrations decay exponentially as material spreads in concentric circles outwards. This picture of turbulent dispersion is not wrong; but it represents the ensemble average. In the real world of turbulent flows, the initially concentrated patch would be stretched into long filaments which then fold and stretch again, like a taffy machine at the corner candy shop. The scalar clearly possesses structure as its concentrations are diluted. By taking the ensemble average of this behavior, structure is lost and we are left with

a radially diffusing scalar with concentrations that decay at an exponential rate.

2.2 Coalescence of Initially Distant Scalars by Diffusion

This thought experiment can now be extended to two scalars that are separated by some distance d. As the scalars diffuse outwards, there will be a region of overlap between the two scalars in which reactions can occur (bottom of Fig. 2.1). By the time these scalars overlap, however, concentrations have been significantly diluted and reactions ($R = kC_1C_2$) are correspondingly low. Would this same behavior be observed if we considered the instantaneous structure of turbulent flows? Previous numerical and experimental work from the Crimaldi group have hinted that it would not. The same structures that are responsible for dilution may also be responsible for local coalescence, drawing two distant filaments into the same region of space while concentrations are still large. We refer to this process as structured stirring, with representative snapshots shown in the top plot of Fig. 2.1.

As a measure of the strength of coalescence between scalars, a normalized reaction rate can be computed. This metric will be used to quantify coalescence throughout the remainder of the thesis, so it will be useful to internalize it now. Reactions between scalars are computed using second order kinetics, with the reaction rate given by

$$R(x,t) = kC_1(x,t)C_2(x,t) \tag{2.2}$$

where k is the reaction rate constant, and C_1 and C_2 are the concentrations of the two scalars. We calculate reactions only in the low-Damköhler number limit, when reaction timescales are sufficiently slow relative to advective timescales that the reactions do not measurably deplete the associated reactants. [2] Because of the bounded domain, it is convenient to normalize the reaction rates using the steady-state rate

$$R_{ss} = kC_{1,ss}C_{2,ss}, \tag{2.3}$$

where $C_{i,ss}$ is the spatially constant, well-mixed concentration as $t \to \infty$, i.e., $C_{i,ss} = \frac{1}{A_D}\int C_i(x,0)dA$, where A_D is the area of the full domain. Reaction rate enhancement is then defined to be the ratio

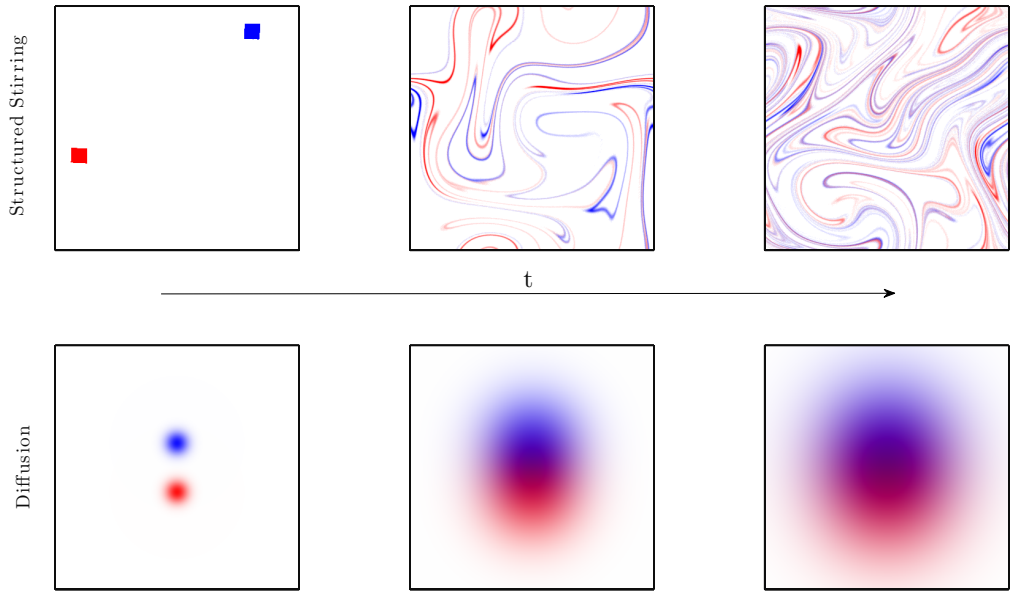

Figure 2.1: Top) Structured stirring of two initially distant scalars (red and blue) with time progressing from left to right. Purple indicates regions where the two scalars have coalesced. Bottom) Diffusion of two initially distant scalars.

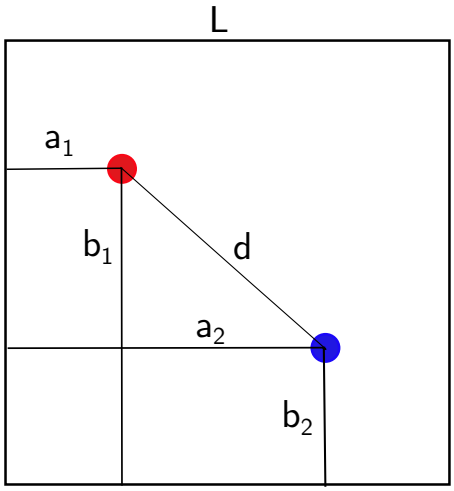

Figure 2.2: Schematic for the placement of two initially distant scalars in a bounded domain.

of the instantaneous, spatially averaged reaction rate to (2.3):

$$R^*(t) = \frac{1}{R_{ss} A_D} \int R(x,t) dA. \tag{2.4}$$

R^* can be physically interpreted as the extent to which the instantaneous reaction rate (averaged across the domain) exceeds or equals the reaction rate of scalars that are completely well-mixed across the domain. An R^* value greater than 1 indicates that the spatially averaged, instantaneous reaction rate is greater than what would be observed if scalars were uniformly mixed throughout the domain while a number less than 1 indicates that the instantaneous reaction rate is less than what would be observed if scalars were uniformly mixed throughout the domain. The question we wish to answer in this chapter is as such: Is there some separation distance for pure diffusion beyond which reaction enhancement cannot occur?

For two initially distant scalars that are separated by a distance d in a closed, bounded domain, an analytical equation can be written for concentration dilution;

$$\begin{aligned} C_1(x,y,t) = \frac{M}{4\pi D t} \Bigg[\sum_{k=-\infty}^{k=\infty} \exp\left(\frac{-(x-(2kL+a))^2}{4Dt}\right) + \exp\left(\frac{-(x-(2kL-a))^2}{4Dt}\right) \Bigg] \\ \Bigg[\sum_{k=-\infty}^{k=\infty} \exp\left(\frac{-(y-(2kL+b))^2}{4Dt}\right) + \exp\left(\frac{-(y-(2kL-b))^2}{4Dt}\right) \Bigg] \end{aligned} \tag{2.5}$$

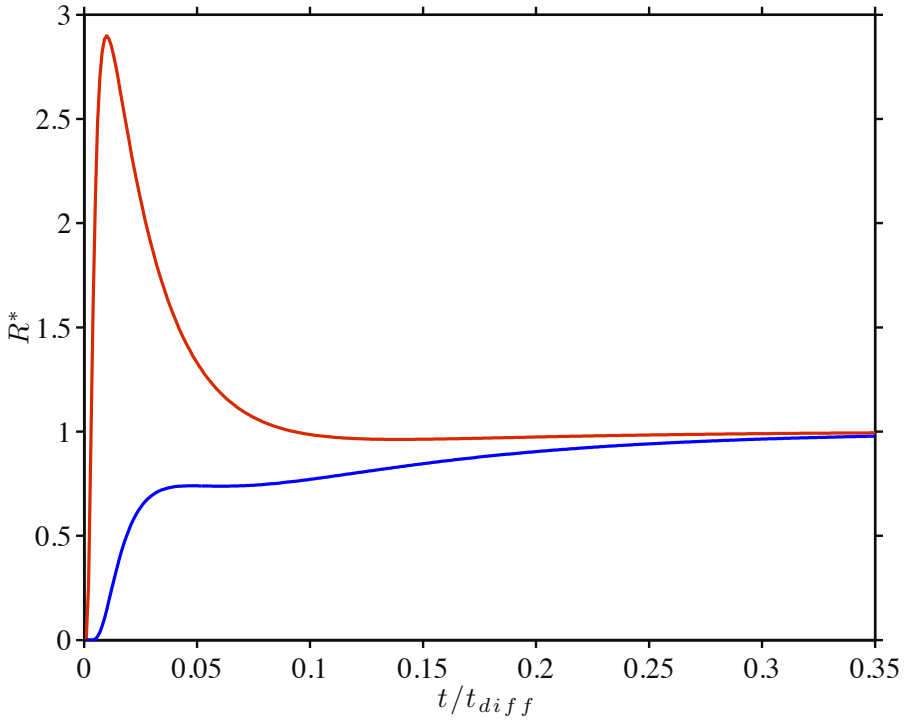

Figure 2.3: Normalized reaction rates vs. time for two seperation distances; $d/L_{max} = .28$ (red) and $d/L_{max} = .57$ (blue)

where L is the length of the domain, a is the distance of the scalar from the left wall, b is the distance of the scalar from the bottom wall. Two scalars are then placed some distance apart (Fig. 2.2) and reaction rates are computed numerically. For this study, $L = 10$. Therefore, the maximum separation distance in a square domain with $L = 10$ is $L_{max} = \sqrt{(L/2)^2 + (L/2)^2)}$. Curves of R^* for various separation distances are plotted in Fig. 2.3. For the red curve, where the separation distance between scalars was equal to $d/L_{max} = .28$, the peak reaction reached $R^* \approx 3$, indicating a reaction enhancement three times greater than the well-mixed reaction rate. The blue curve, however, where the separation distance between scalars was equal to $d/L_{max} = .57$, did not exhibit reaction enhancement as the reaction curve showed a monotonic increase to the well-mixed state $R^* = 1$. Therefore, for pure diffusion, there is some separation distance beyond which reaction enhancement cannot occur.

The left plot of Fig. 2.4 shows the peak reaction rate that is observed as a function of scalar separation distance. When scalars are initially close together, R^* values are large. For example, a separation distance of $d/L_{max} = .02$, corresponds to a peak reaction rate equal to $R^* \approx 1000$. The separation at which reaction enhancement no longer occurs is at $d/L_{max} = .48$. The slope of the line in the loglog plot of Fig. 2.4 is equal to -2. This indicates that the relationship between peak reaction rates and separation distance can be written as

$$R^* \propto \left(d/L_{max}\right)^{-2}. \tag{2.6}$$

Logically, the next question that should be posed is, "What is the likelihood of two points placed randomly in the domain being a certain distance apart?". This likelihood is not uniform for all separation distances. The right plot of Fig. 2.4 shows the likelihood of two points placed randomly in the domain being separated by a given distance. The linear increase from $d/L_{max} = 0$ to $d/L_{max} = .48$ has a simple explanation. The number of possible locations a second point can occupy in order to be a given distance from the first randomly placed point goes as the circumference of the circle surrounding the first point. As separation distances are increased, the circumference of the circle grows linearly with distance. The separation distance that has the highest probability of

being observed is equal to $d/L_{max} = .706$, a distance at which reaction enhancement cannot occur. In fact, for 63 percent of initial conditions, reaction enhancement cannot occur. The solid black line in the right plot of Fig. 2.4 corresponds to the distance at which there is no longer reaction enhancement.

Knowing 1) the probability density function for separation distances of two randomly placed points, and 2) the relationship between separation distance and reaction enhancement, we can derive an equation for the pdf of observing reaction enhancement in a pure diffusive flow. We simply need to transform the separation distance pdf. This is done as,

$$g(R^*) = f\big(d^*(R^*)\big)\frac{dd^*}{dR^*} \tag{2.7}$$

With $f(d^*) \propto d^*$ and $R^* \propto d^{*-2}$ and using the transformation above, the probability density function of observing reaction enhancement for two randomly placed scalars is

$$g(R^*)_{2D} \propto R^{*-2}. \tag{2.8}$$

The likelihood of reaction enhancement, therefore, is a power law with a slope of -2. A similar derivation can be done using 3D diffusion. That derivation will not be shown here, but using the same transformation and the fact that $f(d^*) \propto d^{*2}$ and $R^* \propto d^{*-3}$, the likelihood of reaction enhancement is

$$g(R^*)_{3D} \propto R^{*-2}. \tag{2.9}$$

Using the information from above, a cumulative density function (cdf) can be constructed that gives the likelihood of observing a reaction rate greater than a given amount (Fig. 2.5). The blue curve of Fig. 2.5 shows the likelihood of reaction enhancement for 2D diffusion while the red curve shows the likelihood for 3D diffusion. For the random placement of scalars, the likelihood of observing reaction enhancement in 2D and 3D diffusion was approximately 37 and 30 percent, respectively. As reaction rates increase, the likelihood of observing rates greater than that amount decreases as R^{*-2}. This methodology will be used in future chapters to quantify the likelihood of reaction enhancement due to structured stirring in turbulent flows. In this opening chapter, we've

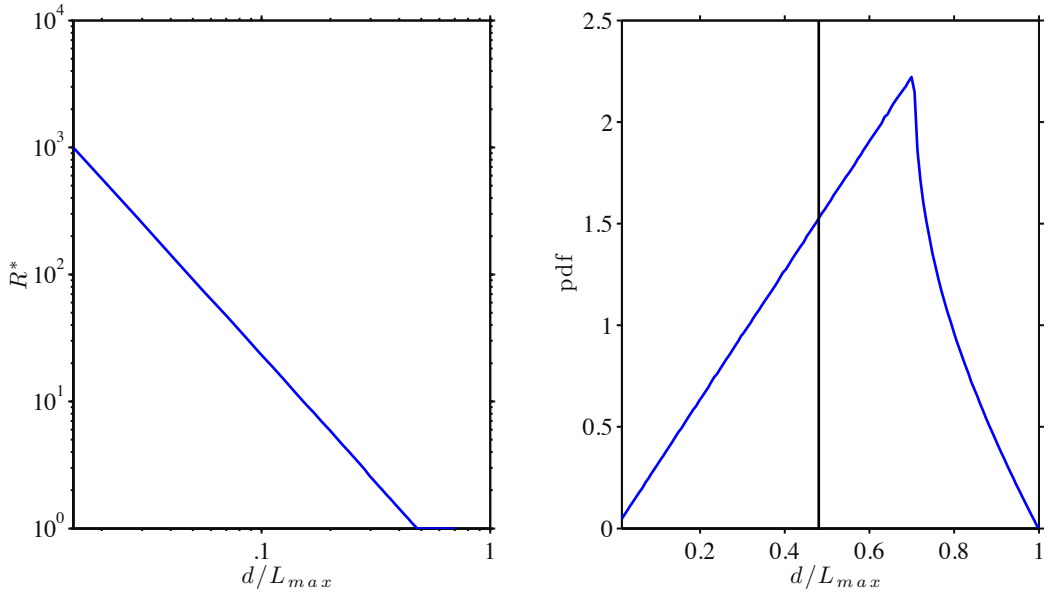

Figure 2.4: left) Peak normalized reaction rates vs. seperation distance. right) Likelyhood of observing a given seperation distance for two randomly placed points.

discussed the coalescence of initially distant scalars through isotropic diffusive behavior. The main take home message is that, unless the scalars are initially close, diffusion cannot lead to enhanced reactions. The peak reactions in these cases correspond to the reaction that would be observed if scalars were uniformly well-mixed in the domain. The remainder of this thesis will deal with turbulent stirring and quantifying how the structures of turbulent flows facilitate the coalescence of initially distant scalars. In the next chapter, we discuss the coalescence of initially distant scalars in structured chaotic flows, and investigate the role of Lagrangian coherent structures in facilitating the coalescence process.

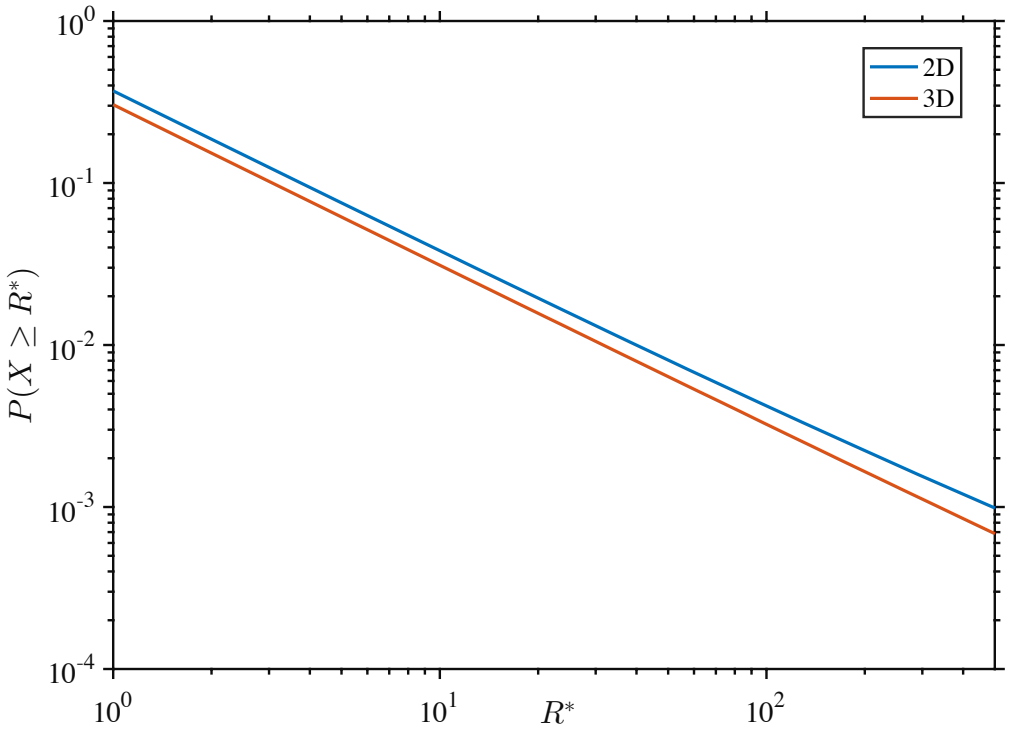

Figure 2.5: Cumulative density function (cdf) detailing the likelyhood of observing reaction enhancement for randomly placed initial conditions. Blue curve gives the likelyhood for 2D and red curve gives the likelyhood for 3D.

Chapter 3

Reaction Enhancement of Initially Distant Scalars by Lagrangian Coherent Structures.

3.1 Abstract

Turbulent fluid flows have long been recognized as a superior means of diluting initial concentrations of scalars due to rapid stirring. Conversely, experiments have shown that the structures responsible for this rapid dilution can also aggregate initially distant reactive scalars and thereby greatly enhance reaction rates. Indeed, chaotic flows not only enhance dilution by shearing and stretching, but also organize initially distant scalars along transiently attracting regions in the flow. To show the robustness of this phenomenon, a hierarchical set of three numerical flows is used: the periodic wake downstream of a stationary cylinder, a chaotic double gyre flow, and a chaotic, aperiodic flow consisting of interacting Taylor vortices. We demonstrate that Lagrangian coherent structures (LCS), as identified by ridges in finite time Lyapunov exponents, are directly responsible for this coalescence of reactive scalar filaments. When highly concentrated filaments coalesce, reaction rates can be orders of magnitude greater than would be predicted in a well-mixed system. This is further supported by an idealized, analytical model that was developed to quantify the competing effects of scalar dilution and coalescence. Chaotic flows, known for their ability to efficiently dilute scalars, therefore have the competing effect of organizing initially distant scalars along the LCS at timescales shorter than that required for dilution, resulting in reaction enhancement.

3.2 Introduction

The stirring and subsequent mixing of passive scalars in turbulent or chaotic flows is of vital importance for a variety of natural and anthropogenic systems. Whether it is the stirring of plankton on the free surface of the ocean, [6] or the mixing of reactive gases in a combustion chamber, [7] turbulent stirring plays a significant role in the transport and dispersion of scalars. Chaotic dynamics provides a general framework to study the advection of scalars and the theory of mixing, areas that had previously been studied on a case-by-case basis. [8] The fundamental processes responsible for the complexity of chaotic advection are the repeated stretching and folding of fluid elements. Stretching leads to exponential divergence of nearby fluid parcels (evidenced by positive Lyapunov exponents), while folding gives rise to chaotic stirring. The resulting large concentration gradients of the advected scalars then leads to enhanced diffusive mixing.

Chaotic stirring has been studied extensively as an efficient means of quickly diluting concentrated scalars. [9, 8] A blob of dye, for example, will quickly be stretched into thin filaments as it is advected in a chaotic flow, leading to an exponential decay of concentration with time. Though many studies have focused on the mixing of single scalars, few have looked at the complex interactions that can occur for a pair of reactive species in a turbulent/chaotic environment. Most of the latter studies focus on initial conditions where the reactive scalars share an interface. [10, 11, 12, 13] In this case, molecular diffusion results in immediate onset of reaction between the scalars and advection leads to increasing reaction rates as the interface between scalars is lengthened and sharpened by stretching. [14] Toroczkai et al.[14] showed that the unstable manifold of a time-periodic von Kármán vortex street was a region of localized enhanced reaction, as the interface of material B (which was advected in a background of fluid A) was lengthened along the unstable manifold. Similar behavior was also found later for a chaotic flow consisting of four vortices. [15] In these studies, the reactions along the unstable manifold were entirely driven by the stirring of material B, since it was contained in a uniform background of A. In many natural systems, reactive scalars do not initially share an interface, and it is fluid stirring that initiates a

reaction. [16, 1] In this topology (where two reactive scalars are separated by a third non-reactive fluid), the initial reaction rate is zero, and stirring leads to reaction only if it causes the initially segregated scalars to come into contact. The presence of repelling regions in the flow, for example, can keep scalars segregated for long periods of time [17], and this can significantly decrease any reaction enhancement because of dilution in the chaotic flow.

3.2.1 Enhanced Reaction of Initially Distant Scalars

Both numerical [2, 5] and experimental [18] studies have shown that the stirring of initially distant scalars may result in their eventual overlap. When the concentration of the filaments is not too low, these coalescence events have been shown to lead to reaction rates much greater than would be predicted by a well-mixed system, a process that we refer to as *reaction enhancement*. Crimaldi et al. [2] considered a simple point vortex and showed—both numerically and analytically—that the vortical strain can result in reaction rates greatly exceeding that of pure diffusion. Next, Crimaldi and Kawakami[5] studied coalescence events downstream of a stationary cylinder that shed periodic vortices. Here, the strain between the counter-rotating downstream vortices resulted in the coalescence of filaments that were initially separated upstream of the cylinder. The coalescence of concentrated filaments is due to the structured stirring from a superposition of vortices, which creates regions of coherent strain and results in the stretching and coalescence of nearby filaments. The mechanisms that lead to this coalescence, however, have not yet been studied. In the current paper, we will elaborate on these mechanisms and quantify the resulting enhanced reaction rates.

3.2.2 Lagrangian Coherent Structures

The visualization of coherent structures within turbulent flows dates back to the time of Leonardo da Vinci. [19] In flowing water, da Vinci saw eddies of many different sizes that interacted with each other in a complex manner, a prelude to the work of Richardson and the energy cascade. The coherent structures, in this view, were Eulerian in nature: turbulent structure was viewed as an instantaneous snapshot of a scalar field that highlights persistent, coherent regions. A component

of vorticity, for example, was often used to track regions of persistent rotation, which can then be characterized as coherent. More recently, the Lagrangian viewpoint has become a useful tool to uncover coherent structures that persist across space and time. By adopting a frame of reference that moves with fluid parcels, we gain a natural means of describing the transport of passive scalars in fluids that have a complicated time history of stretching and folding. [20]

Lagrangian coherent structures (LCS) have been defined as material lines or surfaces in fluid flows that either enhance or inhibit mixing. [21] These time-evolving surfaces have been described as the hidden skeleton of a flow because of how they mold the complex patterns of a passive tracer. [22, 23, 24] Haller showed that such material surfaces could be either attracting or repelling, analogous to the invariant unstable and stable manifolds of hyperbolic orbits in time-periodic chaotic systems. [20] Fluid parcels in the neighborhood of such surfaces are either attracted or repelled at an exponential rate. Repelling LCS (rLCS) act as transport barriers in fluid flows. These have been studied, for example, in a geophysical context to time the release of pollutants near a coastline in order to make them predominantly wash out to sea. [25] By contrast, attracting LCS (aLCS), analogous to unstable manifolds, are attracting surfaces for a passive scalar. For example, larvae on the ocean surface have been shown to aggregate from different source regions onto an aLCS. [26] Not surprisingly, marine predators have also been shown to track aLCS in the ocean in order to locate food patches. [27] The role of stable and unstable manifolds for active process in chaotic flows, such as reactive scalars that share an interface, have also been discussed extensively in the literature. [24, 28]

One standard technique to locate the repelling and attracting surfaces in fluid flows, is the Finite-Time Lyapunov Exponent (FTLE). The FTLE is a scalar field that can be estimated by seeding the domain with a uniform grid of tracer particles and advecting these particles either forward or backward in time. After an integration time T, the rate at which neighboring particles have separated is calculated for each grid point, as described in Shadden et al. [29] Forward integration yields the repelling surfaces by finding the local maximum rate of separation, while backward integration gives attracting surfaces by finding the maximum rate of contraction. The

integration time—for example a typical turnover time—must be selected by the physics of the flow to determine features of interest. Lagrangian coherent structures can be extracted from the FTLE field by locating its ridge lines. It is important to note, however, that ridges in an FTLE field can erroneously identify regions of high shear that are not true attracting or repelling LCS. [22] Indeed the FTLE ridge approach to detect hyperbolic LCS has been described as heuristic in a review by Haller. [30] Occasionally, these ridges can miss LCS due to finite numerical resolution and in other cases the finite-time LCS can be misaligned from the unstable/stable manifold. However, in this study we are mainly interested in locating the approximate stable/unstable manifolds, which correspond to localized surfaces of straining and deformation, and this is precisely what strong ridges in the FTLE usually indicate. As we will see below, FTLE ridges correctly locate regions of enhanced reaction in the flows that we will study.

3.3 Methodology

Reactions between initially distant scalars form through some combination of stirring at large scales and diffusion at small scales. We consider reactions that obey second order kinetics, with the reaction rate given by

$$R(x,t) = kC_1(x,t)C_2(x,t) \tag{3.1}$$

where k is the reaction rate constant, and C_1 and C_2 are the concentrations of the two scalars. The location and magnitude of the resulting reactions depends on the details of the flow field. In this paper, we demonstrate that Lagrangian coherent structures provide a template for locations where reactions are likely to occur. To demonstrate the generality of the correspondence between LCS and reaction zones, we will study three models. Each has a 2D incompressible flow and is dominated by vortex interactions.

The first flow is the periodic vortex wake behind a stationary cylinder, the second is the time-periodic double gyre, and the third consists of an interacting set of Taylor vortices. This last flow is both aperiodic and chaotic, and is most representative of a 2D turbulent velocity field.

3.3.1 Flow Field Descriptions

3.3.1.1 Cylinder Wake

The first flow is the laminar cylinder wake from Crimaldi and Kawakami [5] where a uniform flow with speed u_0 impinges on a circular cylinder with diameter a. When $Re = u_0 a/\nu = 100$, this leads to the periodic shedding of vortices with a period $T_0 = 9.3$, downstream of the cylinder. Representative streamlines for this flow are shown in Fig. 3.1. In order to separate the underlying vortex motion from the ambient flow (Fig. 3.1a), streamlines are also computed for $\mathbf{u} = (u - 0.95u_0, v)$ (Fig. 3.1b). Immediately downstream of the cylinder, counter-rotating vortices are periodically shed leading to localized Lagrangian chaos. [31] The separatrix region between these vortices is an area of significant fluid straining. [32] Particle paths further downstream are not chaotic; nevertheless, the separatrices persist and are asymptotic to stable and unstable manifolds of a steady flow.

A pair of reactive scalars (red/light gray and blue/dark gray) with constant concentration over a width w and lateral separation s, are continuously released upstream of the cylinder at $x = -2.4a$ (as shown in Fig. 3.6). The scalars obey an advection-diffusion equation with diffusivity D. The velocity and scalar fields were computed numerically using a finite-element discretization of the Navier-Stokes and reactive transport equations within the COMSOL Multiphysics package. Details are given by Crimaldi and Kawakami. [5]

3.3.1.2 Double Gyre

The second flow is a simplified dynamical model of a double gyre (Fig. 3.2), an incompressible flow consisting of two counter-rotating vortices that alternately expand and contract periodically. The flow exhibits Lagrangian chaos and has been used in many previous studies as a test-bed for Lagrangian diagnostics. [29, 33] The velocity field is given by

$$\begin{aligned} u &= -\pi U \sin(\pi f(x)) \cos(\pi y), \\ v &= \pi U \cos(\pi f(x)) \sin(\pi y) \frac{\partial f}{\partial x}, \end{aligned}$$

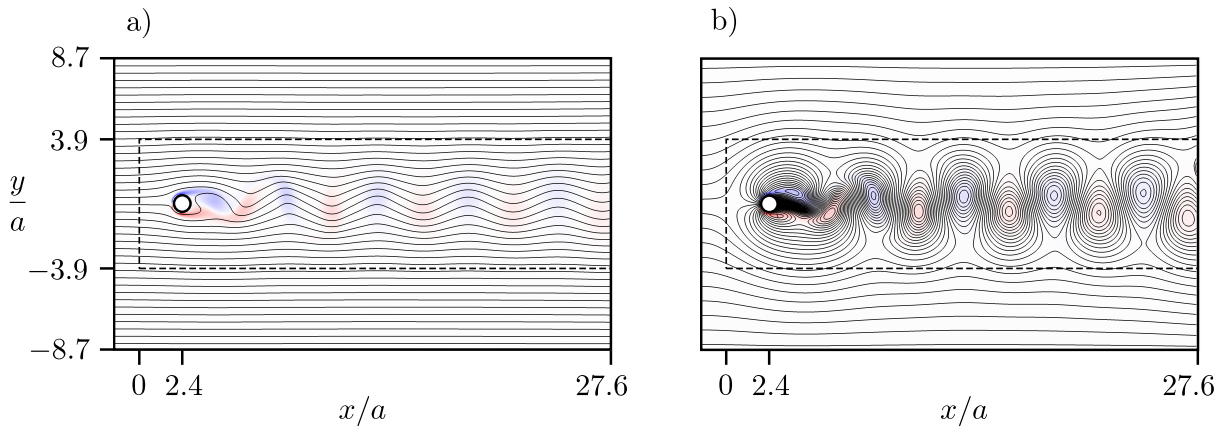

Figure 3.1: a) Streamlines $\mathbf{u} = (u, v)$ and vorticity for the cylinder wake at Re=100. b) In order to separate the underlying vortex motion from the ambient flow, the streamlines are computed for $\mathbf{u} = (u - 0.95u_0, v)$. Regions of positive (red/light gray) and negative (blue/gray) vorticity are superimposed on the streamlines. The dashed box in a) and b) denotes the cropped subregion shown in Figs. 5 and 6.

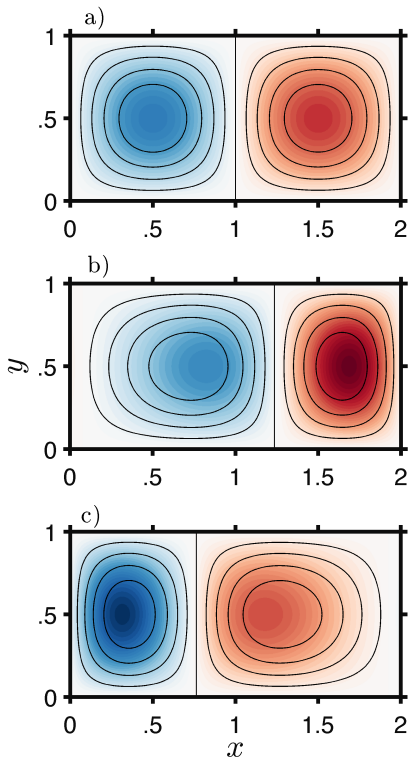

Figure 3.2: Streamlines and vorticity (colors) for the double-gyre flow at quarter-period intervals. a) $t = 0, T_0/2, T_0$. b) $t = T_0/4$. c) $t = 3T_0/4$.

where

$$f(x,t) = x\left[1 + \epsilon \sin(2\pi t/T_0)(x-2)\right].$$

For the computations below, we choose velocity magnitude $U = 0.1$, perturbation amplitude $\epsilon = 0.25$, and oscillation period $T_0 = 10$. Scalar concentrations are computed using a Lagrangian particle tracking method as discussed in Crimaldi et al. [2] and are advected using a second-order improved Euler scheme.

3.3.1.3 Interacting Taylor Vortices

The third example, in the tradition of Aref, [34] consists of a collection of interacting Taylor vortices; it serves as a simple model for 2D incompressible turbulence. From a dynamical systems perspective, the system of interacting Taylor vortices is the most complex used in this study, as it is both aperiodic and chaotic. A Taylor vortex centered at the origin has tangential velocity

$$u_\theta = Ur \exp\left(-\frac{r^2}{2r_0^2}\right),$$

where U is the strength of the vortex, r is the distance from its center, and r_0 is the radius of the core. This is one member of a family of exact vortex solutions to the Navier-Stokes equations. [35] This shielded vortex, shown in Fig. 3.3, has a relatively compact rotational core which then transitions to a nearly irrotational, sheared outer region. In our model, the center of each Taylor vortex is advected by a superposition of the velocities from the remaining vortices, but each vortex has fixed shape and strength. The vortices move in a square with domain size $10r_0$, and periodic boundary conditions are imposed. For this model, 36 vortices are placed randomly in the domain, as shown in Fig. 3.4a; each vortex has radius $r_0 = 1$ and strength $U = \pm 0.5$. The sign of U determines the rotation direction—clockwise or counterclockwise—and it is chosen randomly; in our simulation there were 14 positive and 22 negative vortices. The superposed velocity field of the vortices at $t = 0$, as well as a contour plot of the total vorticity, is shown in Fig. 3.4b. Vortices are advected (by the superposed velocity at the vortex center) using a second-order improved Euler scheme. Scalar concentrations are computed in the same manner as the double gyre.

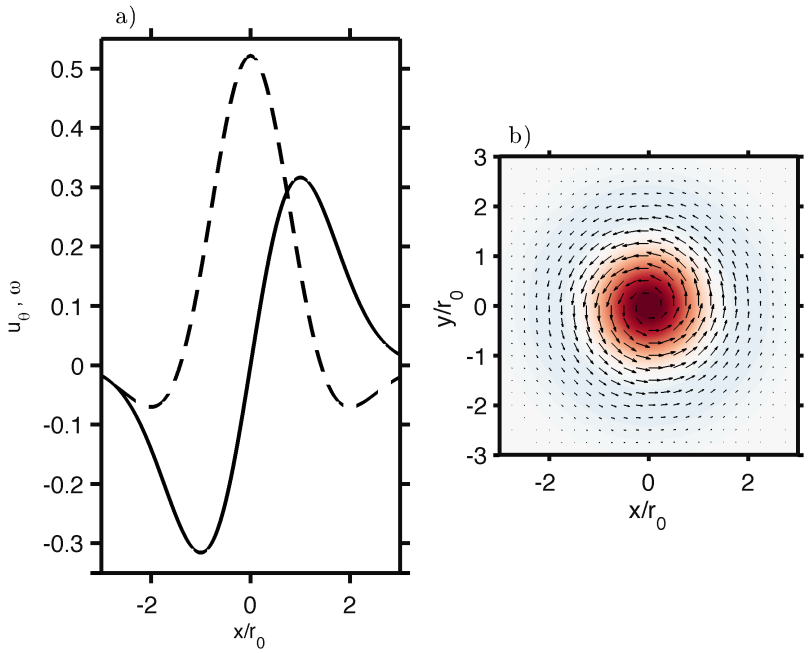

Figure 3.3: Single Taylor vortex: a) velocity (solid line) and vorticity (dashed line) on a slice through the core; b) velocity vectors overlaid onto the vorticity field (colors).

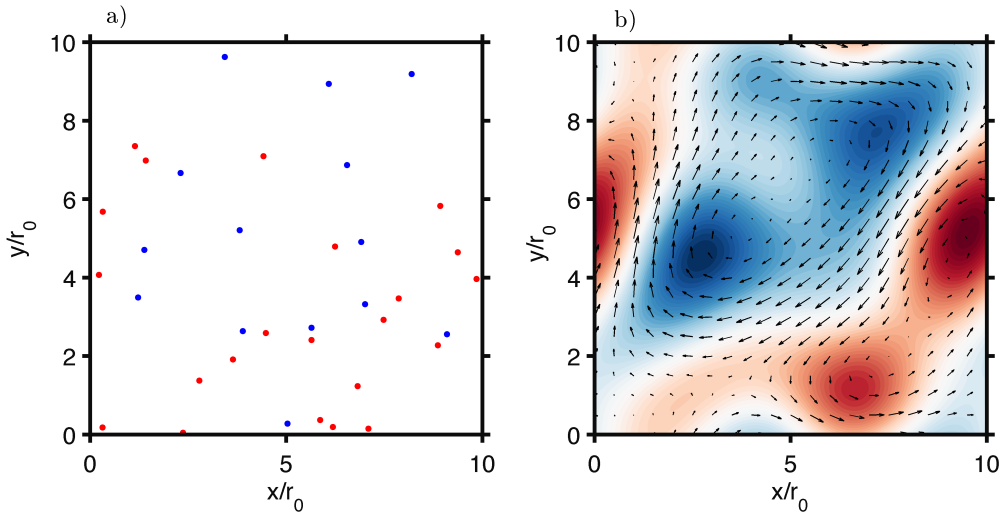

Figure 3.4: a) Initial locations and direction of rotation (red/light gray is positive, blue/dark gray negative) for the 36 vortices used in the Taylor vortex flow. b) Velocity field and vorticity for the superposition of the Taylor vortices in (a).

3.3.2 Calculating Finite Time Lyapunov Exponents

Backward finite-time Lyapunov exponents were computed for the three flows following the method of Shadden et al. [29] A flow map $\phi_{t_0}^{t_0-T}$ is generated by advecting an initially uniform array of points (350 $\times$ 1200 for the cylinder flow, 201 $\times$ 401 for the double gyre, and 401 $\times$ 401 for the Taylor vortices) backwards from $t = t_0$ over an integration time T. In this study, T ranged between 2 and 2.5 periods or turnover times of the flow in order to resolve the appropriate dynamics (for a discussion of the appropriate choice for T in reacting flows, see the end of this chapter). Approximate derivatives of $\phi_{t_0}^{t_0-T}$ with respect to initial conditions are computed using centered finite differences to generate the so-called right Cauchy-Green deformation tensor

$$\Delta = \frac{d\phi_{t_0}^{t_0-T}(\mathbf{x})}{d\mathbf{x}}^{*} \frac{d\phi_{t_0}^{t_0-T}(\mathbf{x})}{d\mathbf{x}}.$$

Finally, the FTLE is computed as

$$\sigma_{t_0}^{T}(\mathbf{x}) = \frac{1}{2T} \ln\Big(\lambda_{max}(\Delta)\Big), \tag{3.2}$$

where $\lambda_{max}(\Delta)$ is the maximum eigenvalue of Δ. The topological ridge lines of the spatial distribution of the FTLE field correspond to aLCS, a region of strain which attracts nearby particle trajectories.

3.4 Results

3.4.1 LCS as a Template for Reaction

3.4.1.1 Cylinder Wake

The FTLE field for the periodic cylinder wake computed using Eq. (5.1) is shown in Fig. 3.5. Since the far downstream wake is not chaotic, increasing T does not grow the manifolds as it would for chaotic systems, but it does sharpen the ridges.

Spatial distributions of scalar concentrations and corresponding reaction rates for the cylinder wake are shown for three different scalar releases in Fig. 3.6. The left column shows concentrations

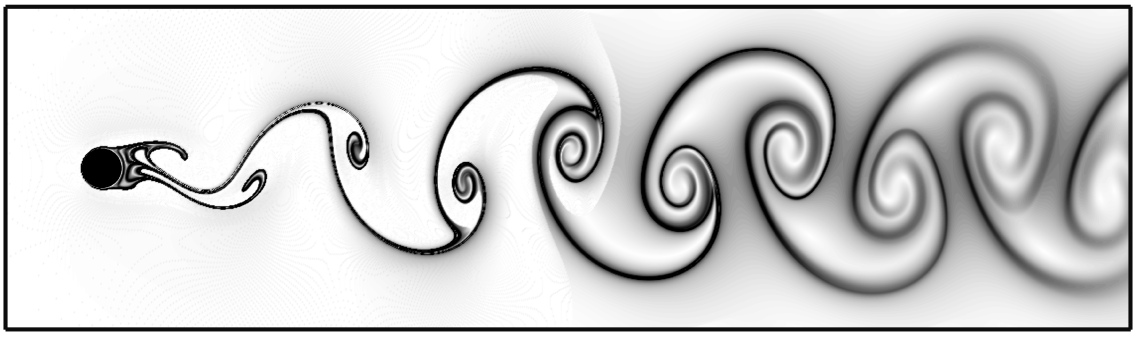

Figure 3.5: FTLE field at a single phase of the cylinder wake for $T = 25$, approximately 2.5 times the shedding period, $T_0 = 9.3$.

of C_1 (blue/dark gray) and C_2 (red/light gray) for three sets of parameters at $t = 80$. The two scalars are initially separated upstream of the cylinder and they begin coalescing in the wake as stirring and diffusion act to bridge the initial separation. The right column shows resulting reaction rates R (purple/dark gray) from Eq. (5.3), superimposed on the FTLE field for the same flow phase (light gray).

Note that though the FTLE field is solely a function of the flow (and integration time T), the spatial distribution of the concentration and reaction rates depends upon both the flow and the details of the scalar diffusivity and release positions. Nonetheless, the FTLE ridges serve as a template for the reaction locations. Though the presence of an LCS does not guarantee that there will be a local reaction, where there is a reaction, it invariably corresponds to a ridge. The larger initial scalar separation in Fig. 3.6(a) delays the onset of reaction until further downstream relative to (b), for which initial separation is smaller. As a consequence, there are locations near the cylinder for case (a) where there is no reaction on the LCS, while for case (b) the reaction migrates upstream along the LCS. These two cases also have different scalar diffusivities (as quantified by the Schmidt number $Sc = \nu/D$). Reaction filaments always have finite widths, whereas the LCS is, in principle, simply a curve. When the diffusivity is larger, as in case (a), the reaction filament is wider and extends further spanwise from the centerline of the LCS. For the set of parameters, Fig. 3.6(c), the scalars are both released to one side of the cylinder; this demonstrates that even

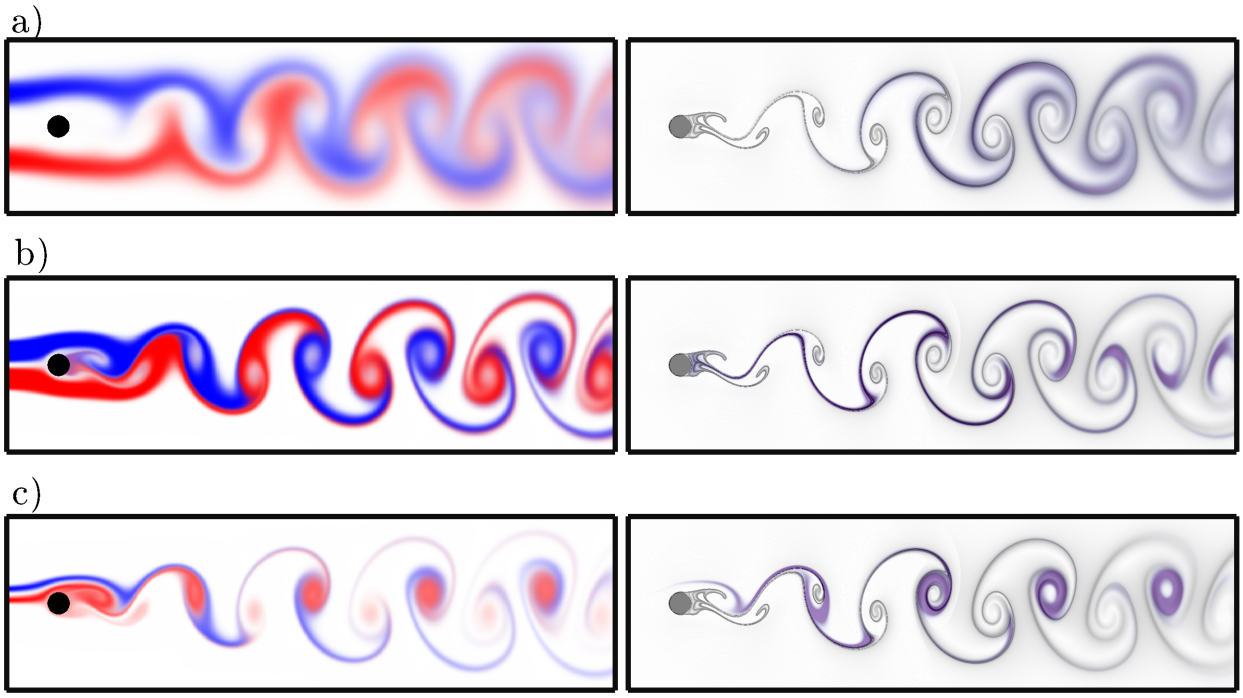

Figure 3.6: The left column shows scalar concentrations (red/light gray and blue/dark gray) and the right shows reaction rates (purple/dark gray) superimposed on the corresponding FTLE field (light gray) for the cylinder wake. a) $s = 2a$, $w = a$, and Schmidt number $Sc = 1$. b) $s = 0.25a$, $w = a$, and $Sc = 10$. c) An asymmetric scalar release with $s = 0.25a$, $w = a$, and $Sc = 10$.

asymmetric scalar release conditions result in reaction zones that are constrained to the ridges of the FTLE.

3.4.1.2 Double Gyre

Figure 3.7 shows the evolution of the scalar concentrations and corresponding reaction rates for the double gyre flow for four sequential times. As in Fig. 3.6, the left column shows scalar concentrations, and the right column shows corresponding reaction rates superimposed on the FTLE field. The first row shows the initial conditions; because the scalars are separated, there is no reaction. As time evolves, scalars begin coalescing and reacting on the LCS. The figures in the second row shows that by $t = 2.5T_0$, multiple red (light gray) and blue (dark gray) filaments have been attracted to the same manifold and that reaction has begun near the unstable periodic orbit on the upper boundary. Continual stretching along the unstable manifold of this saddle brings these filaments into closer contact, further enhancing the reaction, as shown in the third and fourth rows. As in the previous case, reactions do not occur everywhere on an LCS ridge, but where reactions do occur, they are centered on these ridges.

3.4.1.3 Taylor Vortices

Representative scalar concentrations and corresponding reaction rates for this flow are shown at four different times in Fig. 3.8. Even for this more complex flow, stirring of the two initially distant scalars leads to coalescence and initiation of reactions on the LCS.

3.4.2 Reaction Rate Enhancement

The results of the previous section show qualitatively that Lagrangian coherent structures serve as spatial templates for reactions in a range of 2D flows. We now turn to a quantitative investigation of the reactions rates. Because Crimaldi and Kawakami [5] previously reported reaction rates for the cylinder wake case, we limit ourselves herein to the double gyre and Taylor vortex flow. For simplicity, and because we are interested fundamentally in the role of structured

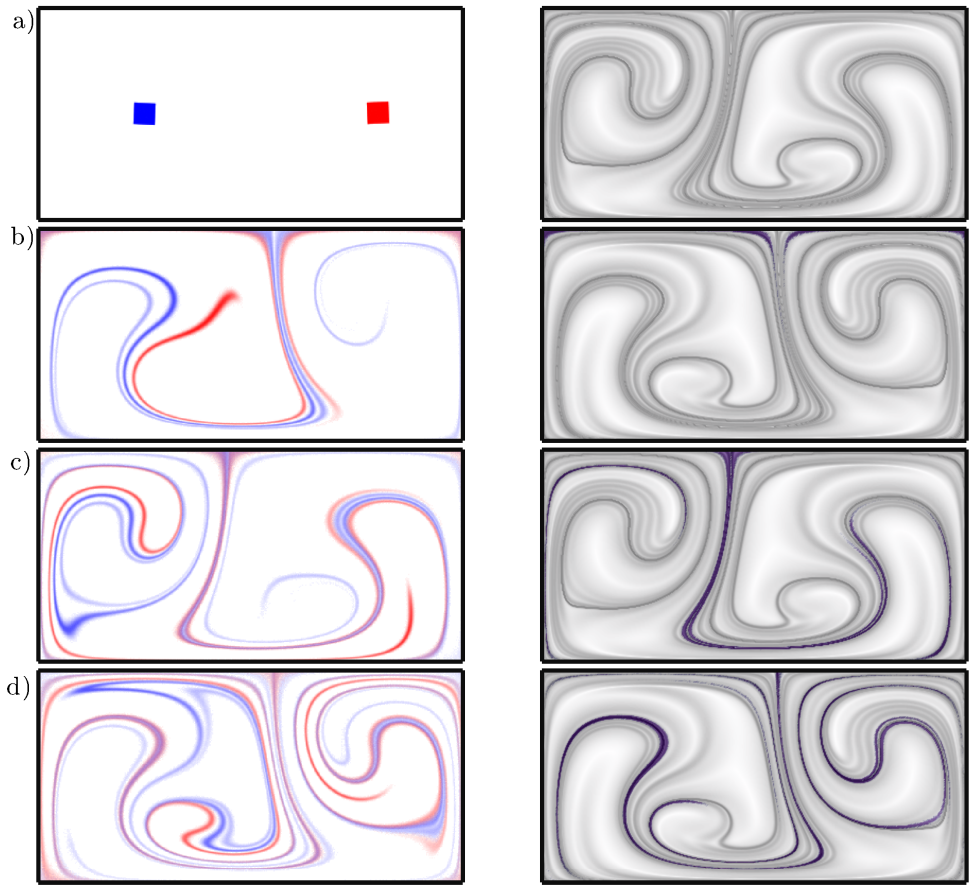

Figure 3.7: Scalar concentrations (left) and reaction rates superimposed on the corresponding FTLE field (right) for the double gyre at a) $t = 0$, b) $t = 2.5T_0$, c) $t = 3T_0$, and d) $t = 3.5T_0$. Note that the flow phase alternates between rows. The blue/dark gray dye is initially centered at $(x, y) = (0.5, 0.5)$ and red/light gray dye at $(1.6, 0.5)$.

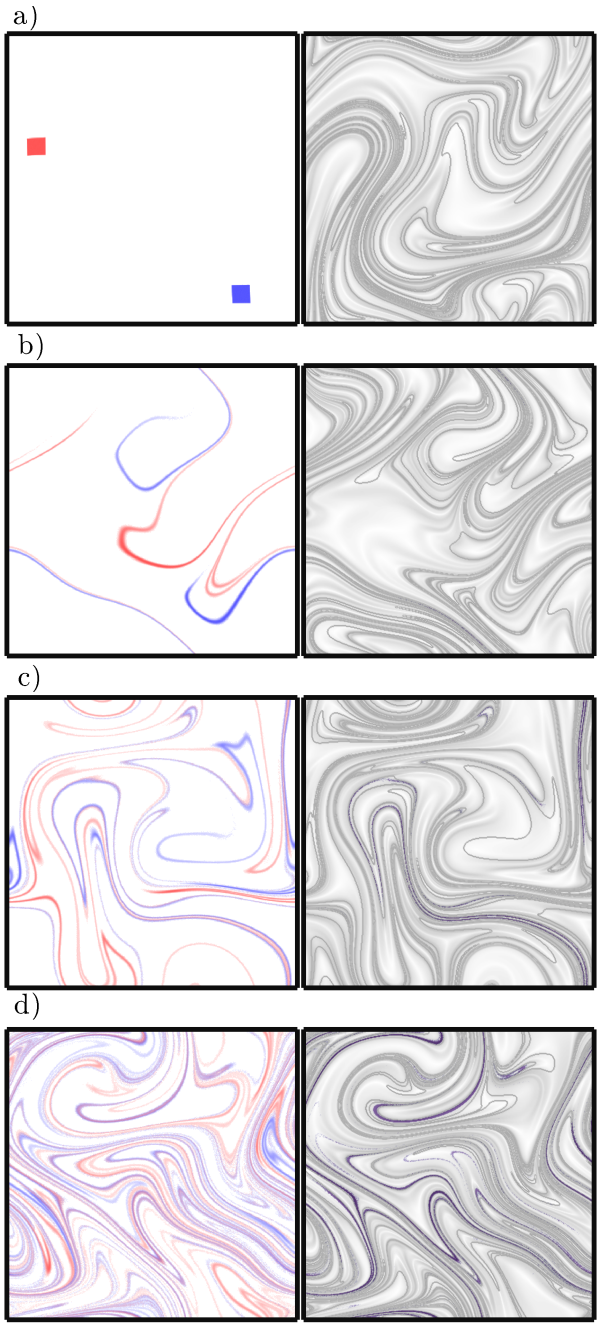

Figure 3.8: (left) Scalar concentrations (red/light gray) and blue/dark gray) and (right) reaction rates (purple/dark gray) superimposed on the corresponding FTLE field (light gray) for the Taylor vortex flow at a) $t^* = 0$, b) $t^* = .483$, c) $t^* = .724$, and d) $t^* = .965$, where $t^* = t2\pi\sqrt{e}/U$ is the time scaled by the turnover time at the core radius r_0.

stirring in promoting reactant coalescence to enable reactions, we calculate reactions only in the low-Damköhler number limit (see App. 3.7), when reaction timescales are sufficiently slow relative

to advective timescales that the reactions do not measurably deplete the associated reactants. [2] Because both the double gyre and Taylor vortex flows have bounded domains, it is convenient to normalize the reaction rates using the steady-state rate

$$R_{ss} = kC_{1,ss}C_{2,ss}, \tag{3.3}$$

where $C_{i,ss}$ is the spatially constant, well-mixed concentration as $t \to \infty$, i.e., $C_{i,ss} = \frac{1}{A_D}\int C_i(x,0)dA$, where A_D is the area of the full domain. The reaction rate enhancement factor is then defined to be the ratio of the instantaneous, spatially averaged reaction rate to (5.4):

$$R^*(t) = \frac{1}{R_{ss}A_D}\int R(x,t)dA. \tag{3.4}$$

To compute the reaction rate enhancement in our models, we begin with a pair of point sources placed randomly in the domain. As is natural for a chaotic systems, $R^*(t)$ is highly sensitive to the initial locations of the sources. Representative values of R^* as a function of time are shown in Fig. 3.9(a) for the double gyre, and in Fig. 3.9(b) for the Taylor vortex flow. In each case, since the scalars are separated at $t = 0$, $R^*(0) = 0$, and since the diffusivity is non-zero, $R^*(t) \to 1$ as $t \to \infty$. However, there are two qualitatively different types of behavior. For some initial conditions, R^* rises monotonically to unity, while for others, R^* may sometimes greatly exceed unity at intermediate times. An example of each behavior is shown for both flows in Fig. 3.9. In all cases, there is an initial time during which R^* remains effectively zero while the scalars are being stretched and folded, but have not yet substantially overlapped. Depending upon the initial locations of the scalars, the concentrated filaments of the two scalars may coalesce on an FTLE ridge at a relatively early time; in this situation, R^* rises to a peak before decaying back to unity. The magnitude of the peak depends on the rapidity of the coalescence (and therefore on the residual concentration). In cases with no reaction enhancement, the coalescence of filaments took longer to occur, and thus the concentrations on the filaments is significantly diluted. Indeed, the exponential stretching characteristic of a chaotic flow also reduces concentrations exponentially.

Because the behavior and magnitude of R^* is sensitive to initial conditions, it is convenient to use a Monte Carlo approach to quantify the likelihood of observing reaction enhancement. To

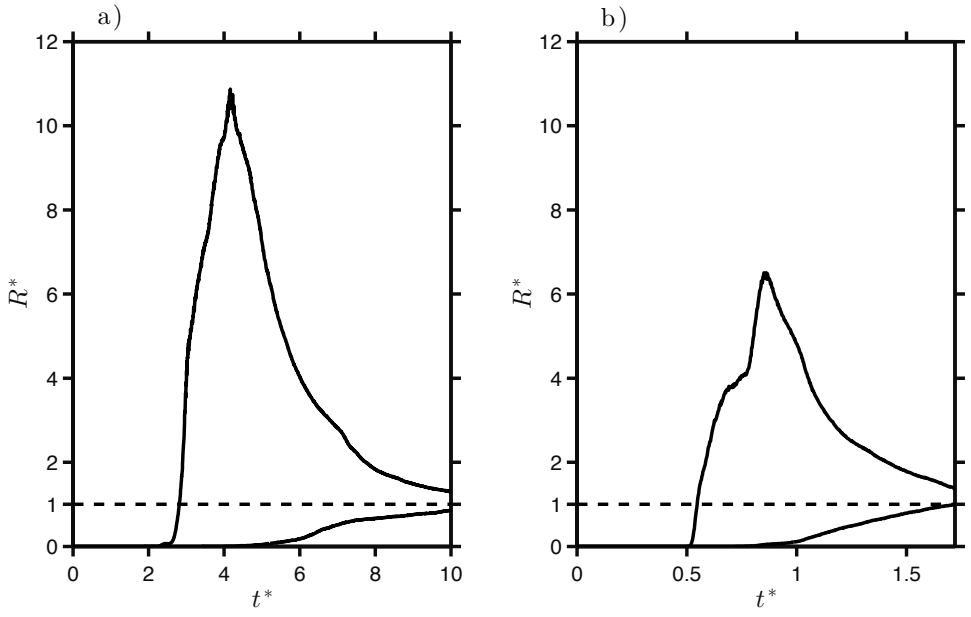

Figure 3.9: Representative values of R^* as a function of time for (a) the double gyre and (b) Taylor vortex flows, each shown for two initial conditions. For these simulations $L_B = 0.01$ for (a) and $L_B = .07$ for (b), and the dye was initialized to a square with sized L_B. For the double gyre, time is nondimensionalized by the oscillation period T_0. For the Taylor vortex flow, time is nondimensionalized by $2\pi\sqrt{e}/U$, the turnover timescale at the core radius r_0.

do this, we vary the initial location of the point sources and determine the peak value of R^* during each simulation. The cumulative density function (CDF) of maximum R^* values where the initial scalar locations were placed randomly within the domain is shown in Fig. 10 (labeled "Random"). The CDF gives the probability that a given initial condition results in a maximum reaction rate greater than a chosen R^*. For example, about 3% of the trajectories give $R^*_{max} \geq 10$. The data are not normally distributed and contain a fat, algebraic tail. The dashed line in Fig. 3.10 corresponds to a power-law fit to the PDF,

$$P(R^*_{max} = x) \sim x^{-\beta}, \quad \beta = 1.9, \tag{3.5}$$

obtained from a Smirnov goodness-of-fit test. [36] Note that this power law tail implies that the mean and variance of the PDF do not exist. Though a majority of the simulations do not result in significant enhanced reaction, about 65% of them had $R^*_{max} > 1$. Reaction enhancement, therefore, is a significant feature of flows with attracting Lagrangian coherent structures.

3.4.3 The Role of Repelling LCS in Reaction Rate Enhancement

In the previous sections, we observed that over an initial period the reaction rate is essentially zero. During this interval, the scalars are stretched and folded but have not yet begun to coalesce on the FTLE ridge. The length of this time lag depends sensitively on the initial locations of the scalars. In Franco et al.[17], the importance of both the repelling and attracting LCS were studied for a vortex shedding event behind a circular cylinder. These authors found that repelling LCS located upstream of the cylinder influenced which regions of the fluid were entrained into the attracting structures downstream. In addition, the role of repelling manifolds, sometimes referred to as burning invariant manifolds in chemical reaction literature, have been shown to act as barriers for reaction front propagation. [37]

Since repelling LCS give approximate stable manifolds, they can separate regions of the fluid, [24] and thus inhibit reactions between our initially distant scalars. A longer reaction initiation lag can be due to the separation of the scalars by a repelling LCS at $t = 0$. The longer this initial

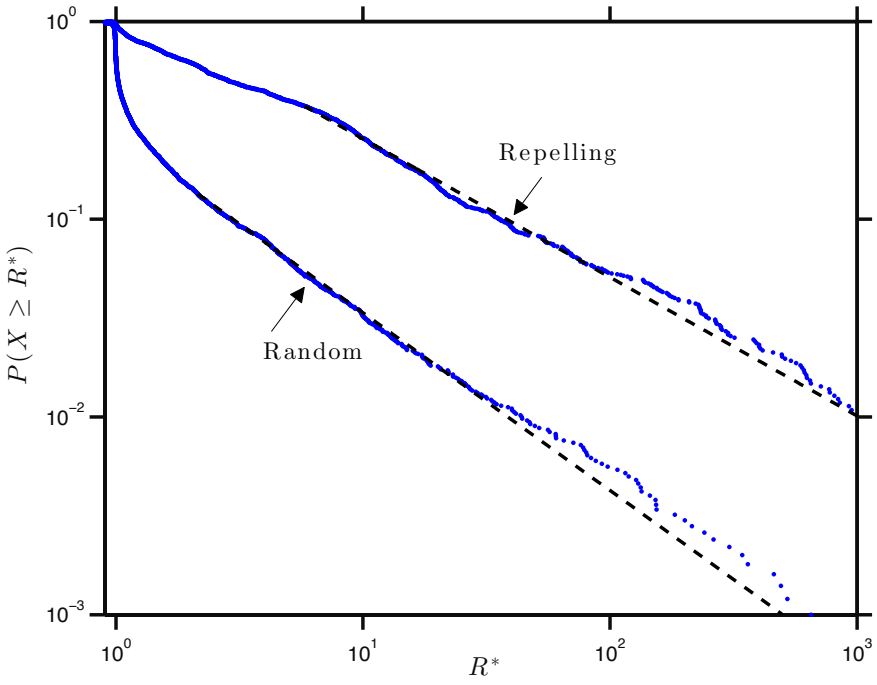

Figure 3.10: Cumulative density functions of maximum R^* for the double gyre flow (dots), along with power-law fits to the CDFs using Eq. 5 (dashed lines). Results are shown for two types of initial conditions: 5000 simulations with initial scalar locations placed randomly in the domain (labeled "Random"), and 2000 simulations with initial scalar locations placed randomly on the repelling LCS (labeled "Repelling").

time lag, the lower the concentrations will be due to dilution, which leads to a lower likelihood of observing reaction enhancement. To show the impact of the repelling LCS on reaction enhancement, another Monte Carlo simulation was run for the double gyre flow, but with initial scalars placed randomly on the repelling manifolds at $t = 0$, rather than randomly throughout the domain. In this case, there is a higher probability that the scalars are on the same local branch of a stable manifold, and this will encourage early coalescence. Indeed, we observe that the reaction enhancement CDF for this case decays more slowly ($\beta = 1.7$), than that for scalars placed randomly in the domain ($\beta = 1.9$), as shown in Fig. 3.10 with the results labeled "Repelling. This figure also shows that, in the repelling case, there is almost an order of magnitude greater likelihood of observing reaction enhancement.

3.5 An Analytical Model

We now proceed to use simple scaling arguments, similar to those presented in Károlyi et al. [12], Tel et al. (2005) [24] and Neufeld (2009) [28], to develop an analytical model that explains the large range of reaction enhancements seen in Fig. 3.10. From Figs. 3.6–3.8, it is clear that large reaction rates occur due to coalescence of concentrated scalar filaments on the LCS. However, a hallmark of chaotic flows is rapid dilution of diffusive scalar concentrations. Thus, the same structured stirring that produces filament coalescence also promotes dilution of filament concentrations. In order for reaction enhancement ($R^* > 1$) to occur, scalars must coalesce at an early enough time so that their concentrations are still sufficiently strong.

If diffusion is neglected, an initially localized passive scalar in a two-dimensional flow will stretch into a filament aligned in the direction of the local strain. When the flow is incompressible, there must be a corresponding contraction in a transverse direction such that area is preserved and the concentration remains constant. For diffusive scalars, the diffusive flux driven by strong transverse gradients eventually balances the stretching-induced contraction. Batchelor [38] used scaling arguments to demonstrate that for turbulent flows this equilibrium filament width (now

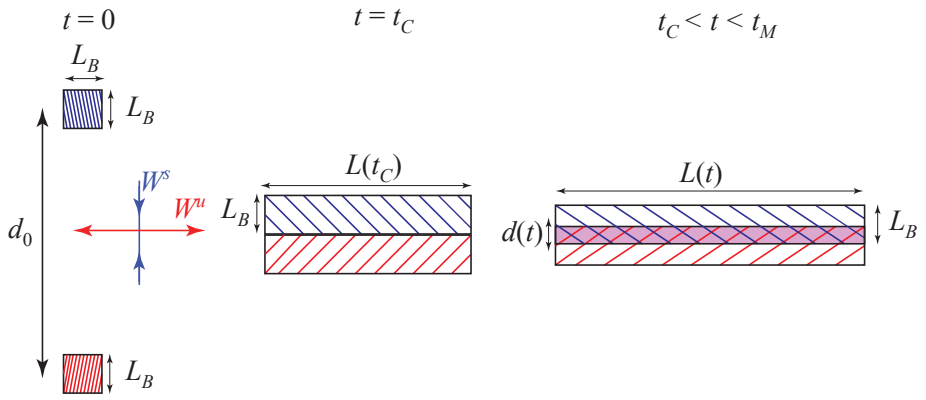

Figure 3.11: Schematic for the analytical model at three times showing two scalars (red/light gray and blue/dark gray) that start at $t = 0$ a distance d_0 apart along the stable direction W^s, coalesce at $t = t_C$, stretching along the unstable direction W^u, and subsequently overlap on an area A_o (purple/gray shading) for $t > t_C$.

known as the Batchelor scale) is

$$L_B \sim \sqrt{D\tau_\eta},$$

where D is the scalar diffusivity and τ_η is the Kolmogorov time. When the flow is chaotic, L_B is commonly estimated by replacing τ_η by λ^{-1}, where λ is the largest Lyapunov exponent, a metric of the mean strain rate; [39, 31] thus,

$$L_B \sim \sqrt{\frac{D}{\lambda}}. \tag{3.6}$$

A chaotic flow will cause a filament to stretch in the unstable direction with an exponentially growing length: on average, $L(t) \sim \exp(\lambda t)$. It simultaneously contracts along the stable direction, and so once it reaches the equilibrium width L_B, the concentration must decay exponentially as $\exp(-\lambda t)$ (ignoring any reactions). This filament behavior in chaotic flows has also been discussed in Károlyi and Tel (2005) [40] and Károlyi (2007). [11]

As a simple model, we consider two scalars with the same initial concentration, C_0, localized to squares of size $L_B \times L_B$ (Fig. 3.11). We will suppose, as the simplest model, that the flow is uniformly hyperbolic with a positive Lyapunov exponent λ, and that the stable and unstable directions are independent of the position of the Lagrangian element. Diffusion will maintain

the width of the scalars in the stable direction at the Batchelor scale; however, they will stretch exponentially along the unstable direction—we assume that this holds even for macroscopic lengths, ignoring the folding that also must occur. Thus the area occupied by each scalar is $A(t) = L_B^2 e^{\lambda t}$, and its concentration is

$$C_1(t) = C_2(t) = C_0 e^{-\lambda t}.$$

However, this exponential decay will stop when the exponential stretching causes the scalar to fill the entire domain, i.e., the area A_D. Thus the decay is valid up to a "mixing time" when $A(t_M) = A_D$ or to

$$t_M = \frac{1}{\lambda} \log \left(\frac{A_D}{L_B^2} \right). \tag{3.7}$$

We will assume that the scalars are initially separated a distance d_0 along the stable manifold (nominally the vertical direction in Fig. 3.11), but they are at the same unstable location (i.e., there is no horizontal separation in Fig. 3.11). Given the exponential contraction in the stable direction, the stable distance will decrease exponentially with time

$$d(t) = d_0 e^{-\lambda t}. \tag{3.8}$$

When $d(t) = L_B$, the scalars come into contact; this is the "coalescence time",

$$t_C = \frac{1}{\lambda} \log \left(\frac{d_0}{L_B} \right), \tag{3.9}$$

and the reaction is initiated. As the vertical distance between the centers of the scalars continues to decrease according to Eq. (5.7), they overlap, i.e., the purple/gray rectangle in Fig. 3.11. Generally, the overlap area is

$$A_o(t) = \begin{cases} 0, & 0 < t < t_C \\ L_B e^{\lambda t}(L_B - d(t)), & t_C < t < t_M \\ \frac{A_D}{L_B}(L_B - d(t)), & t_M < t \end{cases}.$$

The integrated reaction rate is thus $\int R(x,t) dA = k C_1(t) C_2(t) A_o(t)$. Since the steady state reaction

rate, Eq. (5.4), is $R_{ss} = k(C_0 L_B^2/A_D)^2$, then the normalized rate Eq. (5.5) becomes

$$R^*(t) = \begin{cases} 0, & 0 < t < t_C \\ e^{\lambda(t_M - t)}(1 - e^{-\lambda(t - t_C)}), & t_C < t < t_M \\ 1 - e^{-\lambda(t - t_C)}, & t_M < t \end{cases} . \tag{3.10}$$

This implies that $R^*(t)$ reaches a maximum at $t_{max} = t_C + \log 2/\lambda$, provided that $t_C \leq t_{max} \leq t_M$, with the peak value

$$R^*_{max} = \frac{1}{4} e^{\lambda(t_M - t_C)} = \frac{A_D}{2L_B^2} e^{-\lambda t_{max}}. \tag{3.11}$$

The enhancement is largest when the coalescence time is small, or equivalently when the initial separation distance d_0 approaches the Batchelor scale. The pre-factor A_D/L_B^2 in Eq. (3.11) represents the maximum possible enhancement for scalars that completely overlap at $t = 0$. If $R^*(t)$ has a peak at some positive time, $t_{max} > 0$, then the initial scalars have at most 50% overlap, $d_0 \geq \frac{1}{2} L_B$, and R^*_{max} is at most half of this theoretical maximum. Curves from Eq. (5.9) for seven values of t_C are shown in Fig 3.12 (solid lines) for the case that $A_D/L_B^2 = 2(10)^4$. The peak value (Eq. (3.11)) is also shown in Fig. 3.12 (dashed line) as a function of λt. A comparison of these curves with those in Fig. 3.9 shows that the competing effects of scalar coalescence and dilution, described by Eq. (5.9), give rise to the behavior that we observe in the simulations.

To test the validity of (5.9), we performed Monte Carlo simulations for both the double gyre and Taylor vortex flows. The scalars are given initially uniform concentrations on squares of size $L_B \times L_B$, with the diffusivity chosen so that $A_D/L_B^2 = 2(10)^4$. The scalars were placed along the repelling LCS in order to avoid elliptic islands in the flow. Initial overlap of the two squares was permitted (this corresponds to a negative coalescence time); however, in the vast majority of the initial conditions there was no overlap. For each simulation, the peak R^* value and the corresponding time t_{max} are noted. Results are shown in Fig. 3.13(a) for the double gyre and in Fig. 3.13(b) for the Taylor vortex. To compare with the analytical model, λ is estimated to be spatial mean of the FTLE; i.e., $\lambda = 0.13$ for the double gyre and $\lambda = 0.32$ for the Taylor vortex. The R^* values from the Monte Carlo data generally fall below the bound given by (3.11), though there

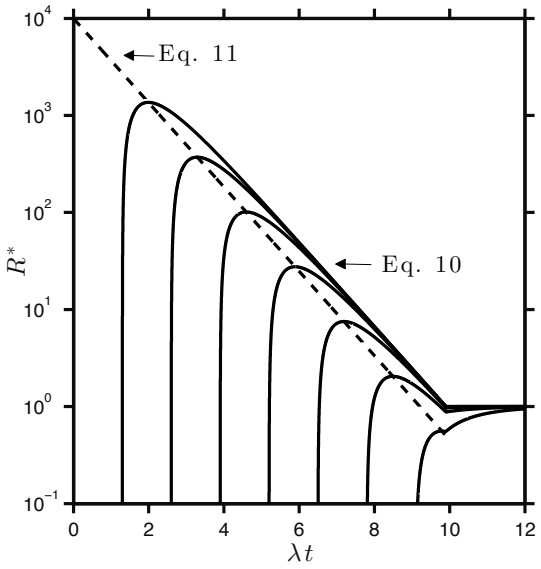

Figure 3.12: A series of normalized reaction rate curves from (5.9) (solid lines) for various coalescence times, t_C, with $\lambda t_M = 9.903$, corresponding to $A_D/L_B^2 = 2(10)^4$. The peak reaction rate (dashed line) is given by Eq. (3.11).

are a few points above, especially for larger values of λt_{max}. This is due, we believe, to scalars not being stretched at the maximal, idealized rate of the model. Indeed, the flows shown in Figs. 3.7-3.8 are certainly not uniformly hyperbolic, and their unstable manifolds fold in a complex way. This could give rise to concentrations larger than predicted by the model, since diffusive dilution is a much slower process than stretching induced dilution.

The large spread in R^* values (across four orders of magnitude) seen in Fig. 3.13 for small λt_{max} is probably due a variation in the filament overlap that can occur at these early times. In particular there there is no reason that the randomly placed scalars should be "vertically" aligned like we have assumed in the idealized model. In other words, they can approach the same unstable manifold from "different" stable manifolds—and therefore have lateral separation that reduces the overlap area. This spread in enhancement values is reduced for larger times since the magnitude of reaction enhancement decays at an exponential rate, as predicted by (3.11).

3.6 Discussion

Lagrangian coherent structures have been demonstrated to play a crucial role in bringing distant scalars together. This idea has a wide range of applicability, ranging from the biological sciences to combustion chemistry. This paper has shown that LCS can serve as templates for reaction zones and that the peak reaction rate enhancement appears to obey a universal, power-law distribution. This contrasts with a viewpoint sometimes expressed in the literature that maximum spatially averaged reaction rates occur when the system reaches a well-mixed state. [41] Under this latter view, optimizing reactions corresponds to maximizing mixing in the sense of rapid and uniform spread of Lagrangian scalars over the flow domain. However, our work has shown that coherent structures in fluid flows can result in enhanced reaction at intermediate time scales and that the spatially averaged peak can be orders of magnitude greater than the steady state rate. The mechanism responsible for this is the persistent straining of an attracting LCS that causes the contraction of the scalars onto filaments where the concentrations can be much larger than in a well-mixed system.

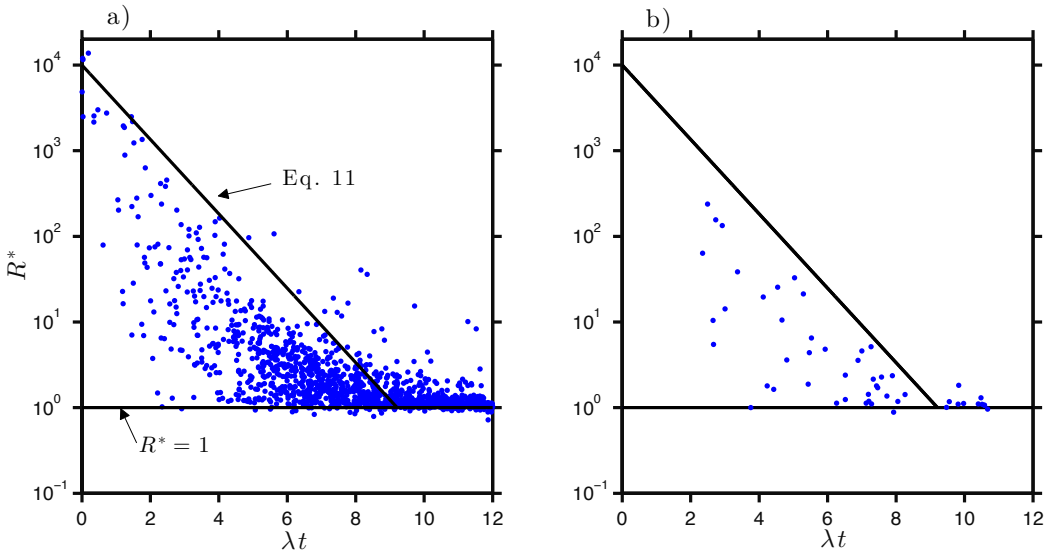

Figure 3.13: Peak reaction (R^*) and peak reaction times from double gyre (a)) and Taylor vortex (b)) from Monte Carlo simulations. The solid line shows (3.11) for $A_D = 2$, $L_B = 0.01$ with λ =0.13 for the double gyre, and $A_D = 100$, $L_B = 0.0707$ with λ =0.32 for the Taylor vortex.

3.7 Damköhler Number and the Integration Time for FTLE

The results in Sec. 4.4 show that LCS do indeed serve as templates for the enhanced reaction zones within chaotic/turbulent flows, regardless of initial scalar placement. Reactions are initiated when the scalars coalesce on the LCS and are then transported throughout the flow. As LCS begin to dissipate, however, it is possible that reactants that coalesced many turnover times ago will have not yet completely reacted. Such remnant reaction zones will no longer appear to be on the FTLE ridge. In such a slowly reacting system, the FTLE field needs to to be integrated for a time period appropriate to the reaction rate. Longer integration times will lengthen the approximate unstable manifolds and give a template for reaction zones over a timescale that can match that of the reaction. By contrast, in a highly reactive system, a shorter FTLE integration time is sufficient to capture the reaction zones. How long one grows the manifold, therefore, is entirely dependent upon the reactivity of the system.

Reactivity is quantified by the advective Damköhler number, which compares the advective timescale, t_a of the flow to the reaction timescale, t_r, of the scalars.

$$Da = \frac{t_a}{t_r}.$$

Using this definition, the Damköhler number becomes

$$Da = \frac{t_a k M}{L^2}, \tag{3.12}$$

where k is the reaction rate constant, M is the total mass of one of the scalars, and L is the initial separation distance between the two scalars.

By using this scaling, a $Da \ll 1$ indicates that reactants are not being degraded appreciably, $Da \sim 1$ signifies that reactants will be depleted within a few turnover times of the flow, and $Da \gg 1$ indicates significant depletion of reactants without appreciable advection. The choice of integration time, T, to compute the FTLE field should therefore match the reactive timescale; that is,

$$T \sim \frac{L^2}{kM}. \tag{3.13}$$

In any case, the flow will have appreciable effect on the reaction only when $Da \lesssim 1$.

In this study, we focused on the moment of coalescence and not on reaction kinetics; thus we set $Da = 0$ for all simulations: the scalars were not degraded, but only advected and diffused. The integration time $T \sim 2 - 2.5$ turnover times, was chosen to resolve only the coalescence events.

3.8 Acknowledgments

This work was supported by the National Science Foundation (NSF) under grants PHY-1205816 to JPC and DMS-1211350 to JDM. This work utilized the Janus supercomputer, which is supported by the NSF award CNS-0821794 and the University of Colorado Boulder. The Janus supercomputer is a joint effort of the University of Colorado Boulder, the University of Colorado Denver and the National Center for Atmospheric Research

Chapter 4

Clustering of Initially Well-Mixed Particles by Lagrangian Coherent Structures in Non-Divergence-Free Flows

> It doesn't make a difference how beautiful your guess is. It doesn't make a difference how smart you are, who made the guess, or what his name is. If it disagrees with experiment, it's wrong.
>
> -Richard Feynman

4.1 Abstract

Particles that float on the surface of a 3D incompressible turbulent flow are exposed to non-divergence-free properties that result in clustering and unmixing, a reversal of the typical arrow of time in which turbulence acts to mix and dilute scalars. Particle clustering is intrinsically a Lagrangian process that depends on the time history of the flow; this suggests that Lagrangian coherent structures (LCS) might serve as templates for cluster formation. In this study, non-divergence-free clustering is examined both experimentally and numerically to elucidate the role of LCS in the formation of particle clusters and voids. Experiments are performed in a 60 $\times$ 60 $\times$ 60 cm water-filled tank with a free-surface; turbulence is driven by random pulsing of 36 centrifugal pumps on the tank bottom. Clustering is quantified by imaging fluorescent, buoyant particles that are placed on the free-surface. Within clusters, concentrations are observed to increase by an order of magnitude, with the likelihood of observing enhanced concentrations increasing by two orders of magnitude. LCS, obtained from velocity fields utilizing particle image velocimetry, are shown to act as templates for the formation of clusters. Numerically, a non-divergence-free chaotic

model consisting of interacting Taylor vortices is utilized to investigate processes responsible for cluster formation seen in the experiments. The model results support the experimental finding that LCS act as templates for particle clusters. In addition, LCS are shown to possess a dilatation component in non-divergence-free flows that is responsible for unmixing. Lagrangian coherent structures, therefore, play a pivotal role in unmixing in non-divergence-free flows.

4.2 Introduction

Initially well-mixed buoyant particles that are confined to float on the surface of a 3D incompressible turbulent flow have been shown to cluster due to non-divergence-free behavior [64, 62, 63]. This non-divergence-free behavior results from the fact that particles are constrained to move within a single 2D plane of the 3D flow. Concentrations of scalars can increase significantly within the clusters, which can have a number of consequences, ranging from increased reaction rates to altered predator/prey relations for clustering biota. A simple example of this behavior on the free-surface of the ocean is the Langmuir circulation [66] where floating scalars (e.g., bubbles, seaweed) tend to flee from areas of upwelling (divergence zone) and aggregate in areas of downwelling (convergence zone), forming long streaks on the ocean surface.

The transport of particles in non-divergence-free flows differs significantly from that of scalars transported in divergence-free flows. In divergence-free flows, turbulence promotes scalar dilution through repeated stretching and folding of fluid elements that enhances molecular diffusion [8, 9]. Turbulence, therefore, is recognized for its ability to mix and dilute initial concentrations of scalars due to rapid stirring. The arrow of time for incompressible chaotic advection, however, can only point in one direction, as it is not possible for initially well-mixed passive scalars to unmix and form clusters [46].

There are two situations, however, that can result in particle unmixing. The first occurs in incompressible divergence-free flows in instances where scalars do not faithfully follow streamlines of the flow [61]. Inertial particles [48] and gyrotactic phytoplankton [49], for example, have been shown to exhibit clustering behavior, even though they are transported by a divergence-free flow.

The second situation involves particles that follow the streamlines of the flow but are transported by a compressible velocity field. Particles confined to the free-surface of an incompressible 3D flow, for example, are following the streamlines of a 2D compressible velocity field.

Previous studies have examined this latter behavior using both experiments and numerics. Cressman et al. [64] quantified clustering on the surface of a water-filled tank ($Re = 160$) using virtual particles in addition to using real particles to visually show increases in particle density. In addition, the mean square seperation between particles on the free-surface showed a reduced scaling exponent compared to the classical Richardson value. A later study expanded upon this using a similar technique to track the time evolution of the fractal dimension, and discussed how an initially uniform distribution of particles can aggregate and form a fractal structure [50]. A result of this clustering is an enhancement in particle concentrations, with concentration PDFs exhibiting a power law decay that is dependent on the scale of sampling [65]. These studies used velocity fields obtained experimentally using particle image velocimetry to advect virtual particles with zero size and mass. This study expands upon this previous work by quantifying clustering using real particles in experimental flows.

Numerically, Boffetta et al. [61] studied the effect of finite-time correlations of the surface velocity field on the formation of clusters. They found that the extent of clustering is influenced by time correlations of the flow, with an enhancement/reduction in clustering dependent upon the compressibility of the system. This was also experimentally verified in a subsequent study [52]. Recently, Lovecchio et al. [53] used DNS to study the time persistence of floating clusters in relation to the fluid time scales. They found that clusters outlive the Eulerian turbulent structures that produced them, indicating that the instantaneous divergence field alone is not sufficient to capture the formation of the cluster's fractal structure. To capture this long-time-scale of formation, a Lagrangian approach is warranted.

Huntley et al. [54] have shown that regions of dilatation (a Lagrangian based metric of quantifying area changes) can be correlated with cluster strength. In addition, they showed that the finite-time Lyapunov exponent (FTLE) field for non-divergence-free flows can be decomposed

into stretching and dilatation terms. This decomposition separates shape changing processes (due to stretching) from area changing processes (due to dilatation). The dilatation rate, therefore, can be used as a diagnostic to predict where clusters will form. Dilatation alone, however, cannot account for how stretching can change the shape of clusters after they have been formed. To capture the full dynamics of cluster formation, both stretching and dilatation may need to be accounted for. Recently, clustering of scalars in simple numerical compressible flows have been linked with the presence of Lagrangian coherent structures [68]. How this behavior translates to systems with chaotic time-dependent divergence fields is still unknown.

Lagrangian analysis has become a useful tool because of the ability to track coherent structures that persist across space and time. As previously discussed, clustering persists over time periods longer than the time scale of the Eulerian structures that initially formed them, such as areas of convergence in downwelling zones. Clusters will be formed by areas of convergence, but deformed by the persistent stretching and folding that occurs in chaotic, turbulent flows. Lagrangian coherent structures (LCS) are defined as material lines or surfaces that highlight the most repelling and attracting regions of the fluid flow [30]. Haller showed that these surfaces are analogous to the invariant unstable and stable manifolds of hyperbolic orbits in time-periodic chaotic systems [20]. Fluid parcels surrounding these surfaces can be either attracted or repelled from these surfaces at an exponential rate. These time-evolving surfaces have been described as the hidden skeleton of fluid flows because of how they mold the complex patterns of a tracer, incorporating the complicated time history of stretching and folding [23]. In addition, these surfaces evolve in time and play a major role in the enhancement or inhibition of mixing [21, **?**], including acting as a template for the coalescence of scalars that were initially separated [67]. Much of the previous work on LCS, however, has been done in an incompressible context. More recently, studies have computed LCS in effectively compressible contexts, such as the transport of inertial particles [69, 70, 71]. The aim of this study is to infer the role that Lagrangian coherent structures play in the clustering of scalars on an effectively compressible free-surface, which thus far has received little attention [54, 68].

A standard technique for locating these repelling and attracting surfaces, whether in a com-

pressible or incompressible context, is the finite-time Lyapunov exponent (FTLE). The FTLE is a scalar field that is computed by advecting a uniform grid of tracers either forward (for repelling surfaces) or backward (for attracting surfaces) in time over an integration time T. The resulting rate at which neighboring particles have contracted or separated is calculated at each grid point. LCS are extracted from this field by locating the ridge lines of the FTLE field. It should be noted, however, that the FTLE field can falsely locate regions of high shear that are not true LCS, and has been described as heuristic in a recent review by Haller (2015) [30]. Other issues include missing LCS due to numerical resolution, in addition to the finite-time LCS being misaligned from the unstable/stable manifold. In this study, however, we are interested in locating surfaces of persistent straining and deformation, which is what strong ridges of the FTLE indicate.

4.3 Experimental Technique

Clustering statistics of flourescent bouyant particles on a turbulent free-surface are collected in a laboratory turbulence facility. Particle flourescence is excited by a laser and imaged from above using a CCD camera. From discretized particle locations, clustering statistics are computed for both turbulent and quiescent cases. In addition, particle image velocimetry (PIV) is used to quantify the turbulence characteristics on and below the free-surface. Aspects of the experimental technique are discussed in turn below.

4.3.1 Turbulence tank

Experiments were performed in a $60 \times 60 \times 60$ cm water-filled glass tank that is open at the top such that there is a free-surface (Fig. 4.1). Turbulence is generated from below using a 6×6 randomly actuated synthetic jet array (RASJA) that has been shown previously to produce large regions of homogeneous and isotropic turbulence [57]. The RASJA is fired in a spatiotemporal random pattern (discussed in the next section) that creates 3D turbulence in the upper region of the tank, driving a turbulent free-surface flow. Each of the 36 vertical jets are independently driven by submerged centrifugal pumps (Rule 360 gph 12 V DC bilge pumps). The jet spacing is 10 cm

and the pump inlets and outlets are located 4 cm and 7 cm above the tank bottom, respectively. The distance between the jet orifices and free-surface is 49 cm; this is sufficiently large to allow jets to merge before they reach the free-surface, thereby eliminating upwelling events from single jets. The experiments were conducted with salt water (100 ppt) to provide sufficient buoyancy for the particles. The free-surface is skimmed before each experimental trial in order to keep the surface clean, as exposure to air and other contaminants have been shown to interfere with free-surface transport [64, 57].

4.3.2 Generation of turbulence

The RASJA design is based on that of Variano and Cowen [57], but smaller in size (6×6 vs. 8×8). The pumps are powered using a 20 A adjustable DC power supply, and individually switched using TTL signals generated using a LabView code paired with a digital output card (PCIe-6509). The TTL signals command MOSFET transistors (N-Channel) to supply DC power to the pumps.

We used the spatiotemporal jet driving pattern found to be optimal by Variano and Cowen (Fig. 4.2): Each jet operates independently of the others, and is triggered randomly for a duration (d_{on}) chosen from a normal distribution (f_{on} centered on $\mu_{on} = 1$ with standard deviation $\sigma_{on} = .25$) and then is turned off for a duration (d_{off}) drawn from a normal distribution (f_{off} centered on $\mu_{off} = 10$ with standard deviation $\sigma_{off} = 3$) . This process is then repeated by continuously sampling on/off times from these normal distributions for all 36 pumps.

4.3.3 Imaging of fluorescent particles for clustering analysis

The free-surface of the flow is seeded with buoyant particles that are subsequently imaged for clustering behavior. The particles (Cospheric UVPMS-BR-0.995) are fluorescent red polyethylene microspheres with a density of 0.995 g/cc and a diameter of 125 microns. Particles are sufficiently buoyant in the 100 ppt salt water that they remain on the surface for the entire range of turbulence intensities tested. Because the particles are hydrophobic, they are initially wetted with a small

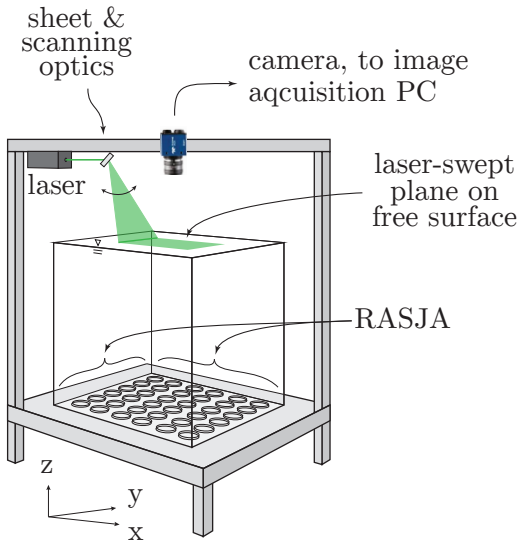

Figure 4.1: Schematic of tank design and laser/camera setup. A 60 × 60 × 60 cm water-filled glass tank is leveled on a steel frame. The RASJA, composed of 36 pumps, rests on the tank bottom. The laser (green) used to fluoresce particles on the free-surface is spread into a sheet and scanned along the free-surface. The camera used to image florescent particles is mounted 50 cm above the tank free-surface.

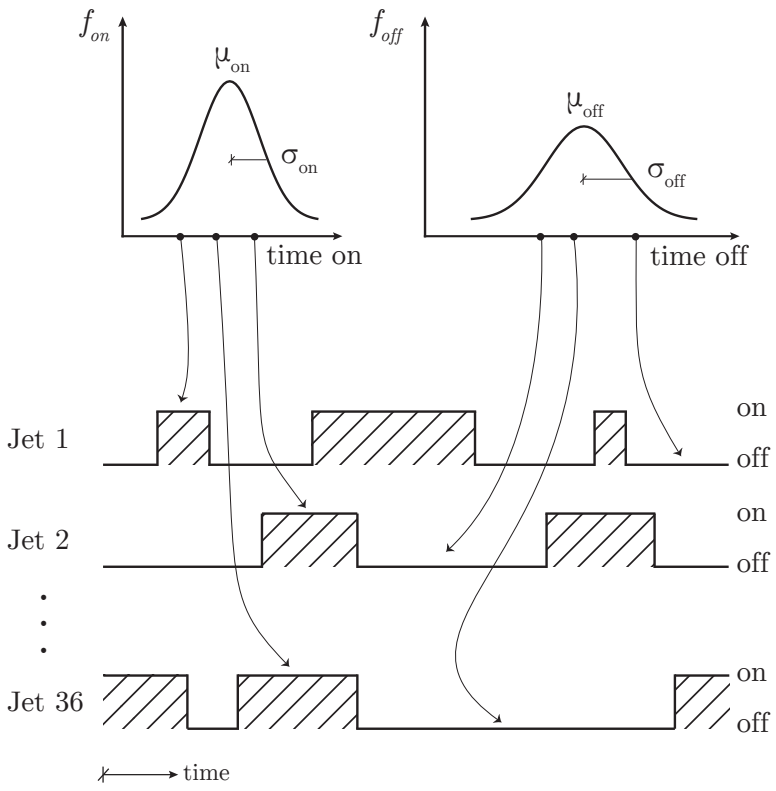

Figure 4.2: Algorithm for pump firing. On and off times are drawn randomly and independently for each pump from normal distributions f_{on} and f_{off}, respectively. f_{on} has mean $\mu_{on} = 1$ s and standard deviation $\sigma_{on} = .25$ s. f_{off} has mean $\mu_{off} = 10$ s and standard deviation $\sigma_{off} = 3$ s.

volume of surfactant (Cospheric Tween 80). Furthermore, to mitigate particle interactions due to surface tension, a small amount of miscible surfactant (25 mL of Dawn dish detergent) is added to the salt water in the tank. Clustering results were insensitive to the addition of surfactant beyond the small amount required to prevent clumping.

Particle fluorescence is excited using a 200 mW 514 nm CW laser. The beam is spread into a horizontal sheet using a cylindrical lens and then scanned along the free-surface by a scanning mirror (Fig. 4.1). Particles are imaged in a central 16 cm $\times$ 12 cm region to avoid wall effects. Images are captured at 1 Hz with an Imperx Bobcat 1410 CCD camera fitted with a 25 mm lens; a band pass filter is used to image only the particle fluorescence. The locations of these particles are discretized using a standard peak finding algorithm. A LabView program is used to synchronize the image acquisition with the light sheet scan.

Wetted particles are initially distributed on a quiescent free-surface. Images are taken in this quiescent state to show that the initial particle distribution is random. For each turbulence case, the RASJA device was activated and 120 images were collected after a 30-second transient period. This procedure was replicated 9 times for each case to produce ensemble clustering statistics and various statistics are computed using these discretized locations.

4.3.4 Quantifying clustering

We use two approaches for quantifying particle concentration distributions based on discrete particle locations. The first, Voronoï tesselation [58], is a scale-invariant approach that we use to compute concentration distributions that are independent of interrogation scale [49]. Voronoï tesselation produces polygons around each particle with a resulting concentration equal to the inverse polygon area. Tesselation polygons at the image boundary can have diverging vertices with an undefined area, and were excluded from the analysis. The second clustering approach, Monte Carlo concentration sampling [59], is a scale-dependant approach that we use to determine characteristic clustering scales. In the Monte Carlo approach, an interrogation region consisting of a circle of diameter d is placed randomly in the domain and the resulting particle concentration is

computed. The domain is interrogated repeatedly with this process until the computed concentration distribution is statistically converged. If a distribution of particles is indeed random, the probability density function of the resulting concentrations using this approach will produce a Poisson distribution [59, 60]. Deviations from randomness due to unmixing will result in a non-Poisson distribution.

The Monte Carlo concentration distributions can be used to compute the clustering index (CI) at a given circle size d

$$CI(d) = \frac{\sigma_c - \sigma_p}{\mu_p}, \tag{4.1}$$

where σ_c is the standard deviation of the clustered concentration distribution, and σ_p and μ_p are the standard deviation and mean from the Poisson concentration distribution. The clustering index for a range of d values is then computed, and the circle size that produces a maximum CI is identified as a characteristic scale of clustering.

4.3.5 Calculating finite-time Lyapunov exponents and the dilatation rate

Backward finite-time Lyapunov exponents are computed for both the experimental and numerical flows using the method of Shadden et al. [29]. A flow map $\phi_{t_0}^{t_0-T}$ is generated by advecting an initially uniform array of points (425 $\times$ 645 for the experimental flow and 401 $\times$ 401 for the Taylor vortex flow) backwards from $t = t_0$ over an integration time T. Approximate derivatives of $\phi_{t_0}^{t_0-T}$ with respect to initial conditions are computed using centered finite differences to generate the so-called right Cauchy-Green deformation tensor

$$\Delta = \frac{d\phi_{t_0}^{t_0-T}(\mathbf{x})}{d\mathbf{x}}^{*} \frac{d\phi_{t_0}^{t_0-T}(\mathbf{x})}{d\mathbf{x}}.$$

Finally, the FTLE is computed as

$$\sigma_{t_0}^{T}(\mathbf{x}) = \frac{1}{T} \ln\left(\lambda_{max}(\Delta)\right), \tag{4.2}$$

where $\lambda_{max}(\Delta)$ is the maximum eigenvalue of Δ. The topological ridge lines of the spatial distribution of the FTLE field correspond to attracting LCS, a region of strain which attracts nearby particle trajectories.

The Lagrangian dilatation rate is a metric that is equal to the average divergence experienced by a particle along its trajectory [54]. This corresponds to the rate at which material volumes are contracting or expanding over time. For incompressible flows, the dilatation rate is equal to zero, signifying an area preserving flow. Non-divergence-free flows, however, consist of regions of both expansion and contraction of fluid volumes, and therefore a non-zero dilatation rate. To compute the Lagrangian dilatation rate, a uniform grid of particles are advected backward in time for an integration time T and the integral is taken along the trajectory for each particle. The Lagrangian dilatation rate δ is then computed as

$$\delta(\mathbf{x}) = \frac{1}{T}\int_{t_0}^{t_0-T} \nabla \cdot \mathbf{u}(\mathbf{x}(\tau),\tau)d\tau. \tag{4.3}$$

In non-divergence-free flows, the FTLE field is equal to the average of the stretching and dilatation rates.

4.3.6 Particle image velocimetry

Planar particle image velocimetry (PIV) data were collected both on the free-surface (x-y plane) and within the water column (x-z plane) to characterize fluid turbulence at varying intensities. The tank was seeded with neutrally buoyant, low Stokes number particles (20 μm, 1.03 g/cc, polyamide microspheres, Dantec Dynamics PSP-20) at densities sufficient to populate interrogation subwindows with 8 - 10 particles at the given optical magnification. Particles were pre-wetted using a surfactant and mixed uniformly in the entire tank. A 200 mW CW laser (514 nm) beam was spread into a thin sheet ($\sim$1 mm) using a cylindrical diverging lens. For water column (x-z plane) data sets, the light sheet was oriented perpendicular to the free-surface illuminating a 10 cm deep plane beginning at the free-surface (13 cm wide). For free-surface (x-y plane) data sets, the light sheet illuminated a 12 cm by 16 cm plane on the free-surface centered in the tank to minimize wall effects. For all data sets, a CCD camera (IMPERX Bobcat 1410M, 1040 x 1392) imaged seeding particles in the light sheet at frame rates selected to optimize particle displacements (10 - 15 Hz depending on turbulence intensities) at one-quarter to one-half the width of an interrogation

subwindow for the given optical magnification.

15 minute image time series were postprocessed using DaVis software (8.2.3, Lavision, Inc.) first to improve particle fidelity via background subtraction and subsequently to compute planar fluid velocity fields. Fast-fourier transform (FFT) based cross-correlation analyses were used to compute particle displacements within interrogation subwindows between successive image frames. Multi-pass cross-correlation schemes with overlapping (50 - 75%) interrogation subwindows of decreasing sizes (264 pixels - 64 pixels) ensured statistically valid correlation peak finding and resulting particle displacement computations. The resulting velocity fields provided time-resolved measurements of fluid turbulence at varying intensities, quantifying both statistical and instantaneous turbulence characteristics.

4.4 Results

4.4.1 Characterization of turbulence in experimental facility

Table 4.1: Turbulence parameters for the three flow conditions in the experimental study.

Re_λ	Pump Voltage (V)	ϵ (cm^2/s^3)	λ (cm)	C
130	4	0.02	1.8	0.19
230	6	0.07	1.7	0.23
350	8	0.16	1.7	0.34

Clustering is investigated for three different turbulence conditions in the RASJA facility (Table 4.1). Turbulence is controlled by modulating voltage to the pumps, which controls the pump speed. Resulting turbulence can be characterized by the Taylor Reynolds number

$$Re_\lambda = \frac{u_{rms}\lambda}{\nu}, \tag{4.4}$$

where

$$\lambda = \sqrt{\frac{u_{rms}^2}{\overline{\left(\frac{du}{dx}\right)^2}}}, \tag{4.5}$$

and TKE dissispation rate (isotropic, homogeneous turbulence) [65]

$$\epsilon = 10\nu\overline{\left(\frac{du}{dx}\right)^2}. \tag{4.6}$$

Furthermore, the compressibility of the free-surface can be characterized by a nondimensionalized mean square divergence [64]

$$C = \frac{\overline{\left(\frac{\partial u}{\partial x} + \frac{\partial v}{\partial y}\right)^2}}{2\overline{\left(\frac{\partial u}{\partial x} - \frac{\partial v}{\partial y}\right)^2}}. \tag{4.7}$$

Higher Re_λ leads to increased compressibility on the free-surface.

Representative snapshots of the resulting turbulence field at $Re_\lambda = 130$ are shown in in a vertical plane intersecting the free-surface (Fig. 4.3) and a horizontal plane at the free-surface (Fig. 4.4). Due to experimental constraints, these snapshots were taken at different times. In both figures, arrows indicate instantaneous velocity vectors in the plane. In the vertical plane (Fig. 4.3) the vertical component of the velocity is depicted, where red indicates regions of upwelling and blue regions of downwelling. Closer to the free-surface, velocities have attenuated, but large regions of upwelling and downwelling are still evident. These regions drive the turbulence on the free-surface and are associated with areas of convergence and divergence, as shown at a different instant of time in Fig. 4.4. The associated divergence field is depicted, where green indicates regions of convergence and purple divergence. As expected, the divergence field on the free-surface is non-zero.

4.4.2 Clustering of initially well-mixed scalars: experimental

4.4.2.1 Quantifying scale-independent clustering with Voronoï tesselation

As mentioned in Section 4.3.4, the Voronoï tesselation provides a scale invariant method of calculating concentration enhancement. The clustering of initially well-mixed particles is shown in Fig. 4.5 at an instant in time. Particles are well-mixed in the quiescent case (left) and exhibit clustering when exposed to turbulent free-surface flow (right). Particle locations are shown in Fig. 4.5a and the corresponding Voronoï tesselations are overlaid on particle location in Fig. 4.5b. Particle

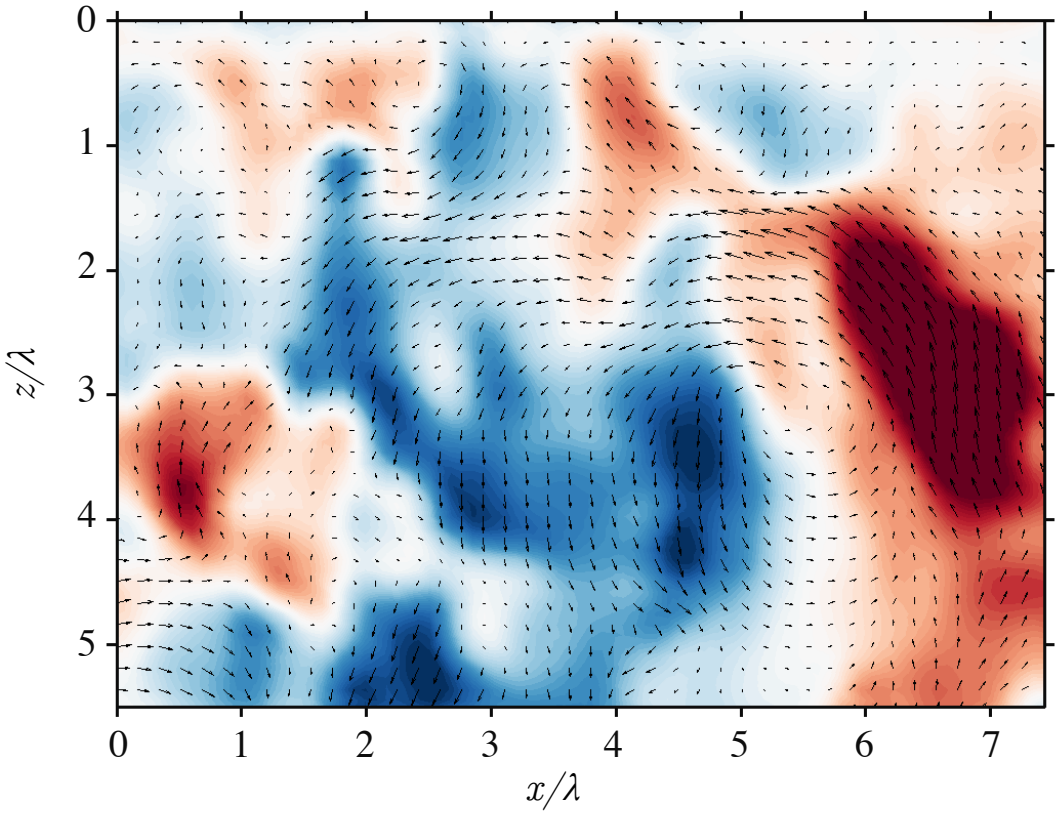

Figure 4.3: Representative instantaneous velocity field (vectors) and vertical velocity magnitude (colors) for a vertical slice extending downward from the free-surface at $Re_\lambda = 130$. Red indicates areas of upwelling while blue indicates areas of downwelling. Magnitudes range from -3 to 3 cm/s.

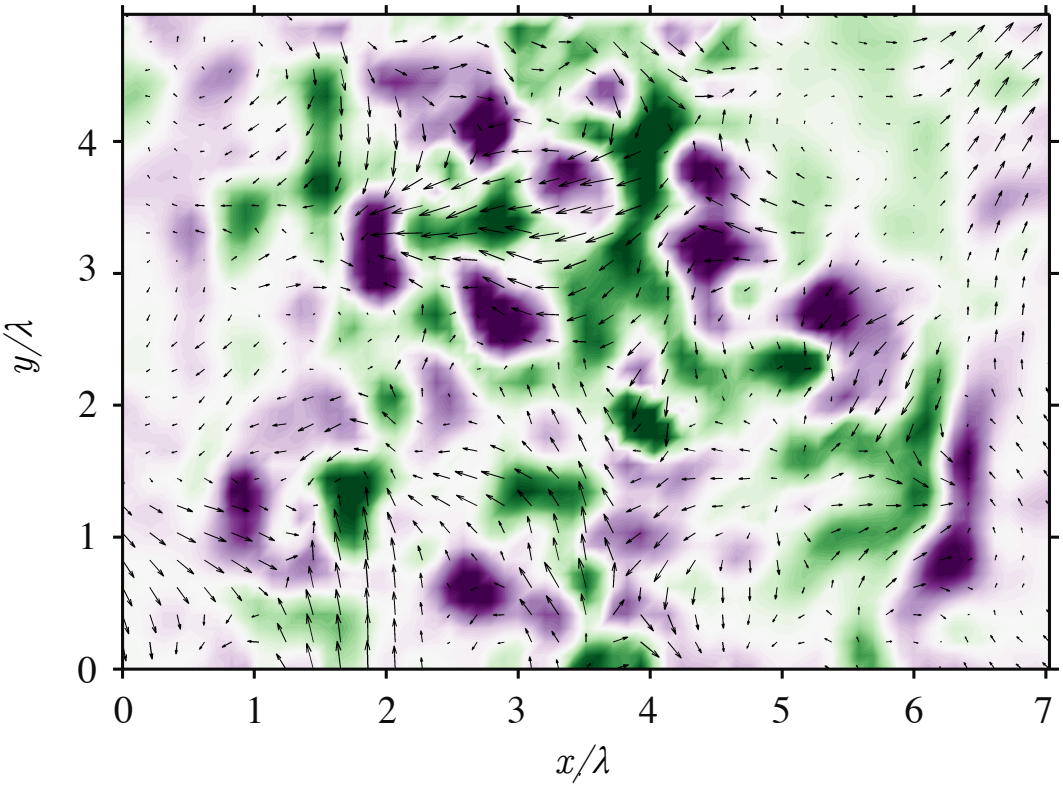

Figure 4.4: Representative instantaneous velocity field (vectors) and divergence field (colors) at the free-surface for $Re_\lambda = 130$. Green indicates regions of convergence while purple indicates regions of divergence. Magnitudes range from -1.25 to 1.25 s^{-1}.

concentrations from the Voronoï tesselations are shown in Fig. 4.5c. Contour values range from $C/C_0 = 0.5$ (light gray) to $C/C_0 = 6$ (black), where C_0 is the average well-mixed concentration. As the particles cluster due to non-divergence-free flow, corresponding concentrations within the clusters increase by an order of magnitude. These large areas of enhanced concentration (black) as well as voids (white) are evident on the turbulent free-surface.

The Voronoï tesselation is used to create probability density functions (PDF) of particle concentrations (Fig. 4.6a) for three turbulence levels (black lines) as well as the initially well-mixed case (blue line). There is an increased likelihood of observing both enhanced concentrations in the clusters ($C/C_0 > 1$), as well as reduced concentrations in the voids ($C/C_0 < 1$). The concentration enhancement can be quantified as the ratio of the turbulent PDFs to the quiescent PDF (Fig. 4.6b). Note that there is a 100-fold increase in the likelihood of observing both reduced and enhanced concentrations. It is evident that as turbulence intensities are increased, the extent of clustering also increases.

4.4.2.2 Quantifying scale-dependent clustering with Monte Carlo sampling

While the Voronoï tesselation presented in the previous section has the advantage of generating scale-independent particle concentrations, the scale at which clustering occurs may be of interest. To that end, we now employ the scale-dependent Monte Carlo approach discussed in Section 4.3.4 to compute particle concentration PDFs (Fig. 4.7a). PDFs are shown for the quiescent case (blue) and turbulent free-surface cases (gray and black). Although the total number of particles varied between flow cases, the diameter of the interrogation region (d) was adjusted for each case such that it contained an average of 17 particles. Also shown (but difficult to discern), is the analytical Poisson distribution corresponding to $\gamma = 17$; as expected this distribution almost exactly matches the quiescent data. This match indicates that the particles were indeed randomly distributed after being deposited on the free-surface. When the pumps are subsequently turned on, clustering is observed, as evidenced by the widening of the distributions, with increased probabilities of observing both enhanced/reduced concentrations. In addition, the width (standard deviation)

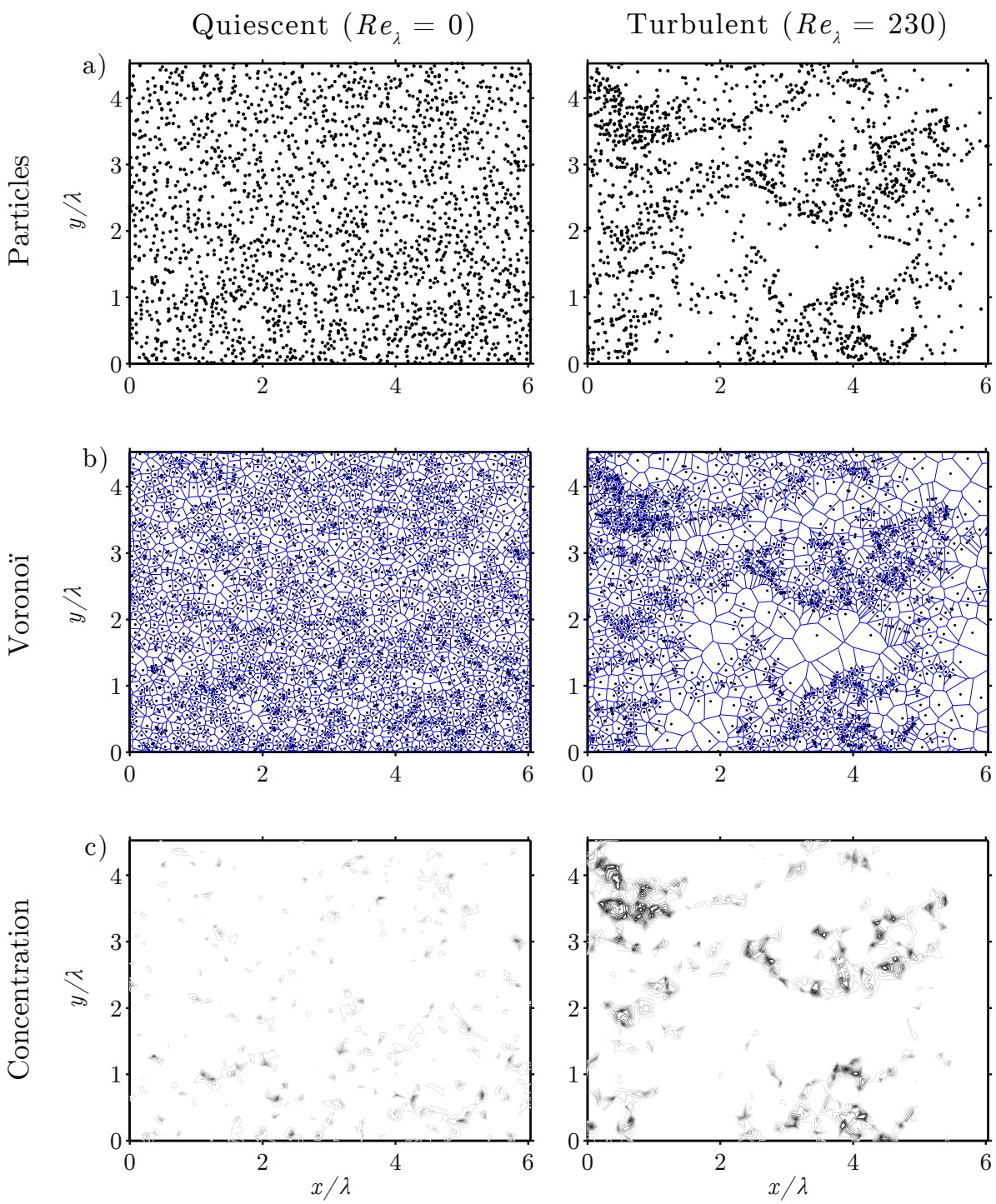

Figure 4.5: Particle location and concentration for the quiescent case (left column) and turbulent case (right column). a) Discretized particle locations (black) at a representative instant of time. b) Voronoï tesselation (blue) superimposed on the discretized particle locations at the same time as (a). c) Contours of concentration computed from Voronoï tesselation with values ranging from $C/C_0 = 0.5$ (light gray) to $C/C_0 = 6$ (black) at the same time as (a) and (b).

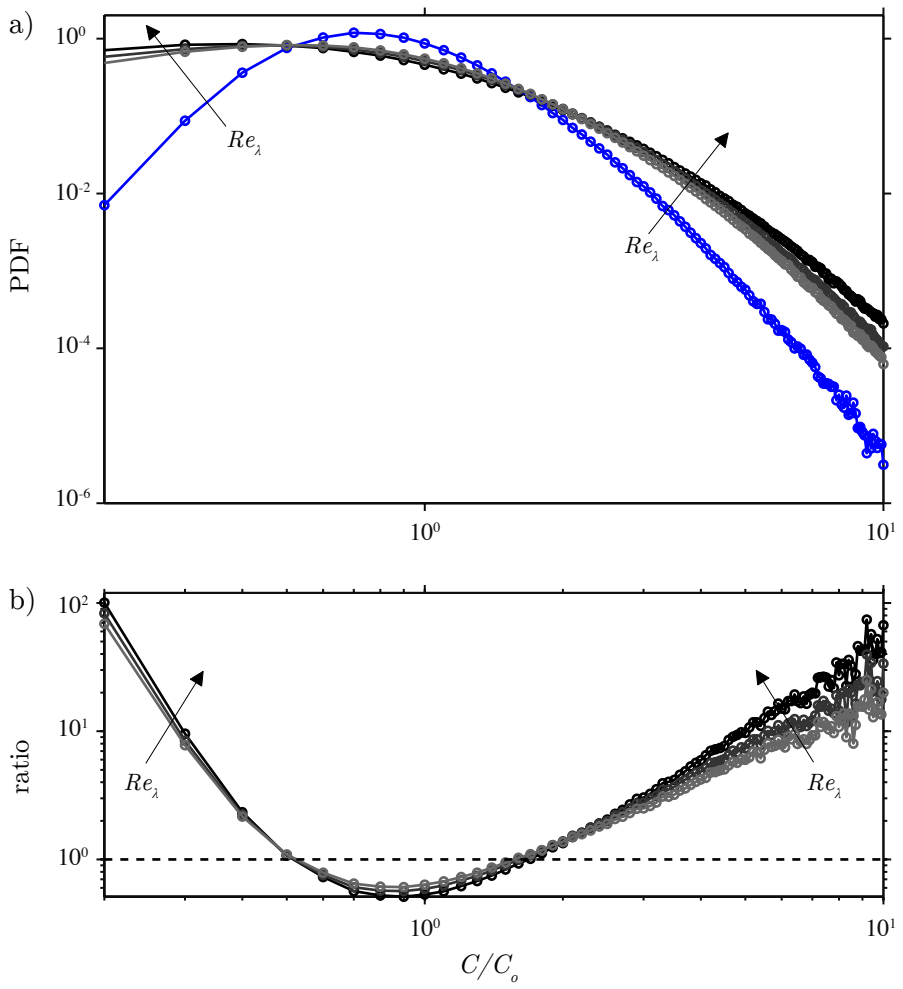

Figure 4.6: a) Particle concentration PDF computed from Voronoï tesselation for four flow cases: $Re_\lambda = 350$ (black), $Re_\lambda = 230$ (gray), $Re_\lambda = 130$ (light gray), and the quiescent case (blue). b) Turbulence concentration PDFs from (a) normalized by the quiescent case.

of the distributions increase as turbulence levels are intensified, which indicates an increase in the intensity of clustering.

We can repeat this approach for a range of interrogation region sizes, and the standard deviation of the resulting PDFs can be used to compute clustering index (Eq. 4.1) as a function of interrogation scale (Fig. 4.7b). The interrogation scale has been normalized by the Taylor microscale (Eq. 4.5). For all cases there is an identifiable interrogation scale at which CI reaches a maximum and then decays. Stronger turbulence levels result in a larger clustering index. The scale at which this peak occurs corresponds to the approximate size of the clusters that are forming. For all turbulence intensities, this scale is smaller than the Taylor microscale ($d/\lambda < 1$). At $d/\lambda << 1$, the curves collapse since sampling of the concentration field is occurring at a scale much smaller than the clusters. At $d/\lambda >> 1$, sampling is occurring at scales much larger than the cluster, and the clustering index will asymptote to zero.

4.4.2.3 Clustering on Lagrangian coherent structures

While clustering is often thought to coincide with downwelling regions in the flow, this is an Eulerian description that ignores the history of particle trajectories. Therefore, a Lagrangian approach is a more natural means of elucidating clustering processes; this latter approach allows us to discuss clustering in terms of Lagrangian coherent structures. To infer the influence of LCS on clustering, virtual particles (sizeless and massless) are advected using velocity fields obtained using PIV on the surface of the experimental facility. By using virtual particles, both the FTLE field and the concentration field can be computed simultaneously. Concentration contours of clustered virtual particles are computed for a random initial condition (Fig. 4.8a) and at two subsequent times as clusters form (Fig. 4.8b-c). The backward-time FTLE field computed at t_2 (Fig. 4.8d) shows a striking similarity to the pattern of particle clustering at the same time in Fig. 4.8c. The black lines (ridges) in the FTLE plot indicate regions of large strain and deformation, which correspond to attracting Lagrangian coherent structures. We therefore demonstrate here that attracting LCS act as a template for the clustering of initially well-mixed scalars in non-divergence-free flows.

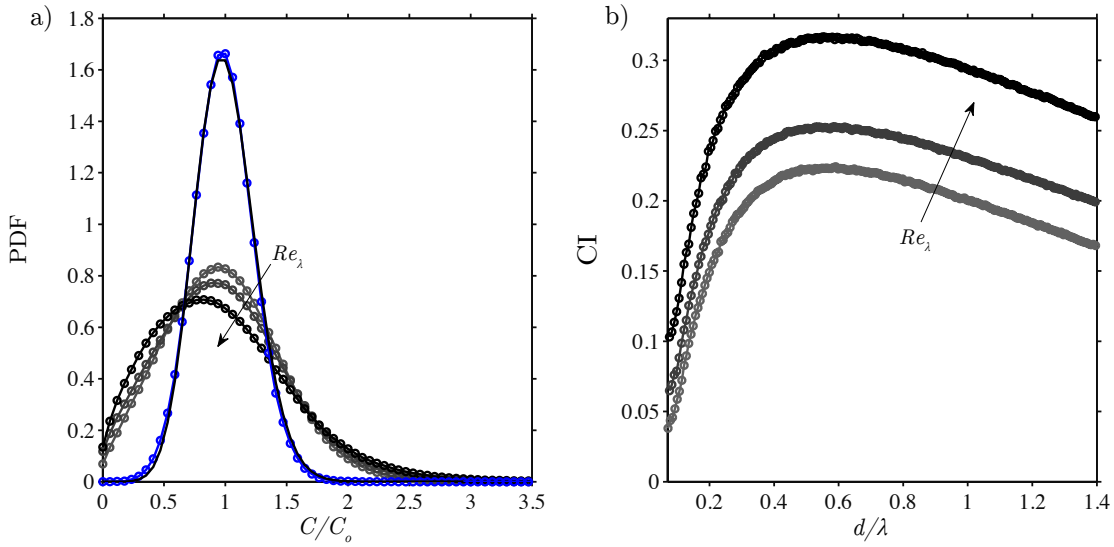

Figure 4.7: a) Concentration PDFs from the Monte Carlo technique for four flow cases: $Re_\lambda = 0$ (blue), $Re_\lambda = 130$ (light gray), $Re_\lambda = 230$ (gray) and $Re_\lambda = 350$ (black); also shown is the Poisson distribution with $\gamma = 17$ (solid black). b) Clustering index for turbulence cases as a function of interrogation scale, using same color coding as (a).

This cluster formation is inherently a Lagrangian process, where non-divergence-free velocity fields compress the scalar field, which results in clusters that are subsequently stretched and deformed along the LCS. To further investigate the clustering seen in the above experimental data, we next turn to numerical models to reinforce and expand upon the above work.

4.4.3 Clustering of initially well-mixed scalars: numerical

4.4.3.1 Non-divergence-free Taylor vortex model

To study the effects of non-divergence-free flows on particle clustering numerically, the interacting Taylor vortex model from Pratt et al. [67] was modified to include non-divergence-free behavior. The original divergence-free model consisted of a system of interacting Taylor vortices that result in a 2D incompressible chaotic flow. A Taylor vortex (Fig. 4.9a) centered at the origin has tangential velocity

$$u_\theta = Ur \exp\left(-\frac{r^2}{2r_0^2}\right),$$

where U is the strength of the vortex, r is the distance from its center, and r_0 is the radius of the core. A final velocity field is then computed through the superposition of velocities from all vortices present in the flow. The vortices move in a square doubly periodic domain with size $10r_0$. For the model, 36 vortices with a radius $r_0 = 1$ and strength $U = \pm.75$ are placed randomly in the domain; the sign of U is chosen randomly for each vortex and determines rotation direction.

Motivated by the work of Pérez-Muñuzuri [68], non-divergence-free effects are added to the model by incorporating a spatially periodic parameter, $\rho(x, y)$, that advects with and alters the velocity field of each Taylor vortex. This field is given by

$$\rho(x, y) = 1 + \kappa \sin(2\pi x/\Lambda) \sin(2\pi y/\Lambda),$$

where κ is a compressibility metric and Λ is the wavelength. For this study, $\Lambda = 5r_0$. The compressible velocity field (Fig. 4.9b) for each Taylor vortex is then

$$u_c = \frac{u_\theta}{\rho}.$$

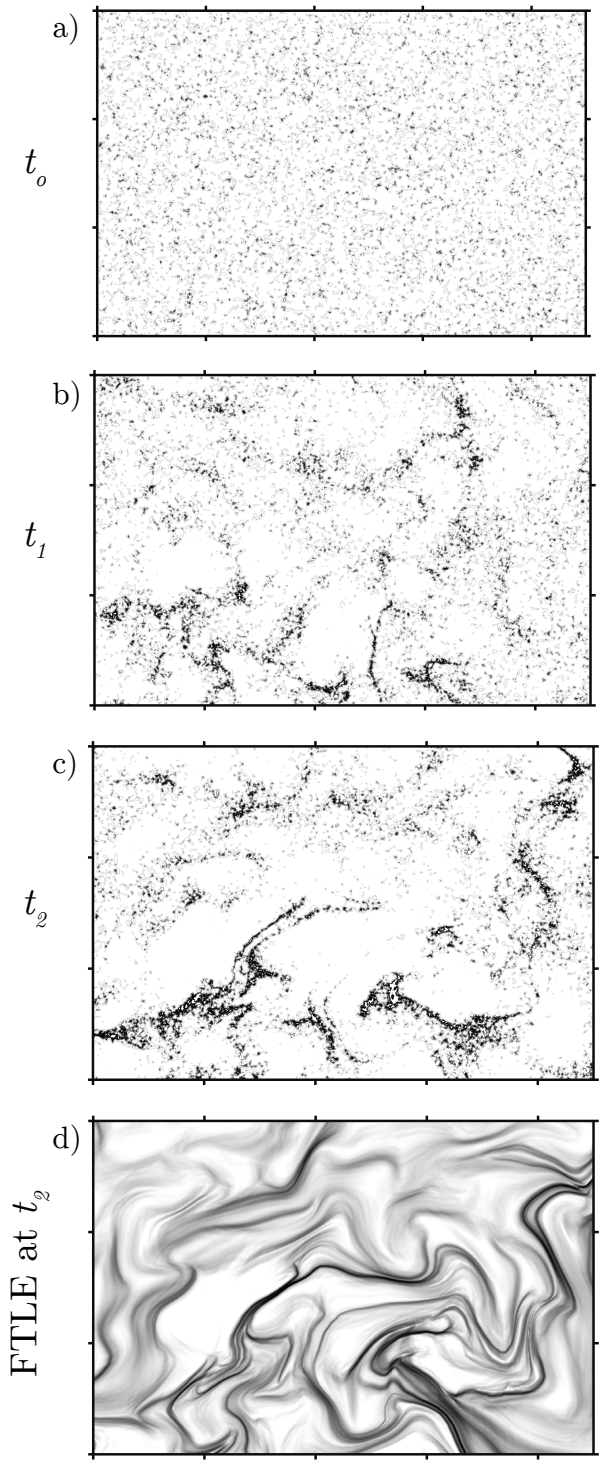

Figure 4.8: a-c) Concentrations of virtual particles using experimentally obtained free-surface velocities. Concentrations range from $C/C_0 = 0.5$ (light gray) to $C/C_0 = 3.5$ (black). The initial condition is shown in (a) with subsequent evolution shown in (b) and (c). d) The FTLE field corresponding to concentrations shown at t_2 in (c).

This alteration is repeated for all 36 vortices, and the velocity field is the superposition of these individual vorticies (Fig. 4.9c). Vortices are advected (by the superposed incompressible velocity at the vortex center) using a second-order improved Euler scheme.

Using the non-divergence-free Taylor vortex model, non-diffusive scalars are initialized in the well-mixed state and begin to cluster when exposed to the flow. Figure 4.10b shows the resulting concentration contours at three times during cluster development; the contours range from $C/C_0 = 0.5$ to $C/C_0 = 6$. The FTLE field (Fig. 4.10a) is overlayed on the concentration contours in Figure 4.10b, confirming that the FTLE, a Lagrangian metric, is capable of capturing this complex time history as clusters can be seen forming on the ridge lines (black), confirming results discussed in the experimental data (Sec. 4.4.2.3). Figure 4.10c shows the divergence at times corresponding to times shown in Fig. 4.10a. At early times, clusters begin forming in convergent regions of the flow (blue/solid lines), with large voids forming in divergent regions (red/dashed lines). As time progresses, clusters become more compact and are stretched by the surrounding flow. Due to the Eulerian nature of the divergence field, it no longer captures the regions where clusters are present as they now have a complex time history of compression and stretching.

The FTLE field used as a metric for LCS consists mathematically of the sum of both incompressible straining and compressible dilatation. The incompressible straining component alone is area-preserving and cannot unmix particles to form clusters; dilatation alone initiates the unmixing. Figure 4.11a shows concentration contours (left), the FTLE field (center), and the Lagrangian dilatation rate (right) for an incompressible flow field ($\kappa = 0$). For incompressible, divergence-free flows, clusters do not form and the LCS do not unmix initially well-mixed scalars. The Lagrangian dilatation rate (Eq. 5.2) is correspondingly zero throughout the domain, confirming that the flow is area-preserving. When moderate non-divergence-free effects are included ($\kappa = 0.2$, Fig. 4.11b), the Lagrangian dilatation rate becomes non-zero and regions of negative dilatation (areas of contraction) coincide with the presence of LCS. Increasing the compressibility further ($\kappa = 0.4$, Fig. 4.11c) leads to larger Lagrangian dilatation rates and increased clustering. In these non-divergence-free cases, the LCS possesses both a dilatation component that results in unmixing and the formation

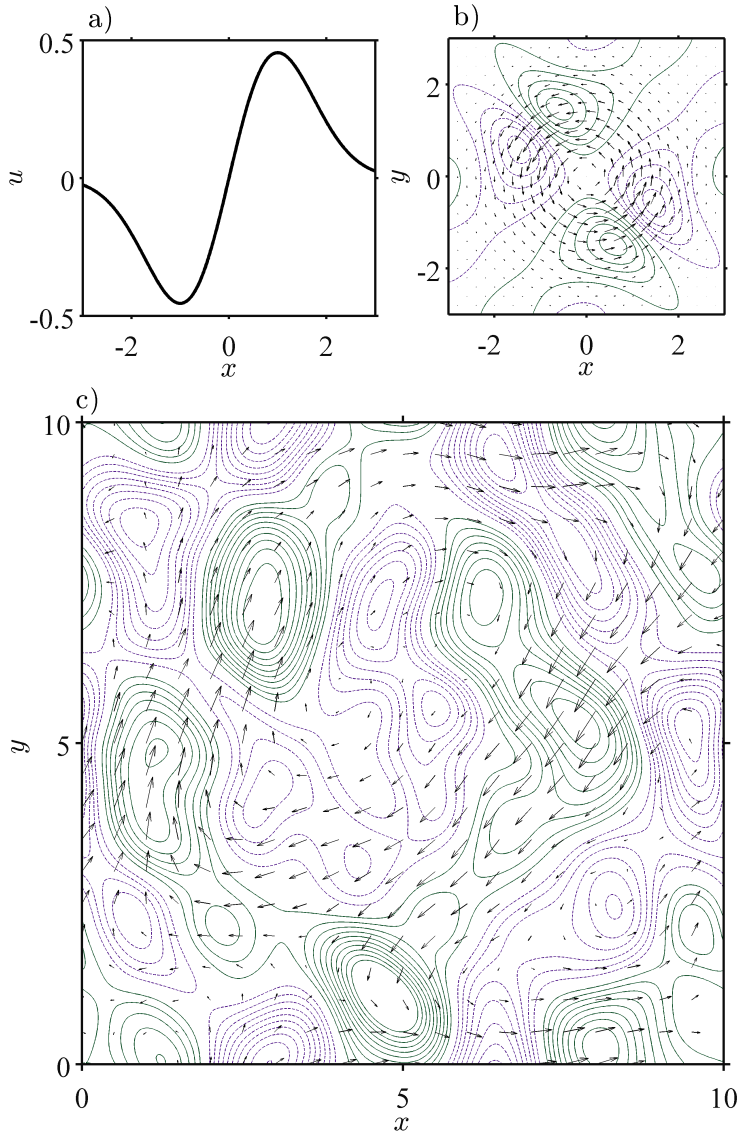

Figure 4.9: a) Horizontal transect of u_θ for an incompressible Taylor vortex. b) Velocity field (vectors) and divergence field (colored contours) for an individual compressible Taylor vortex. c) A representative velocity field (vectors) and divergence field (colored contours) for the superposition of 36 compressible Taylor vortices.

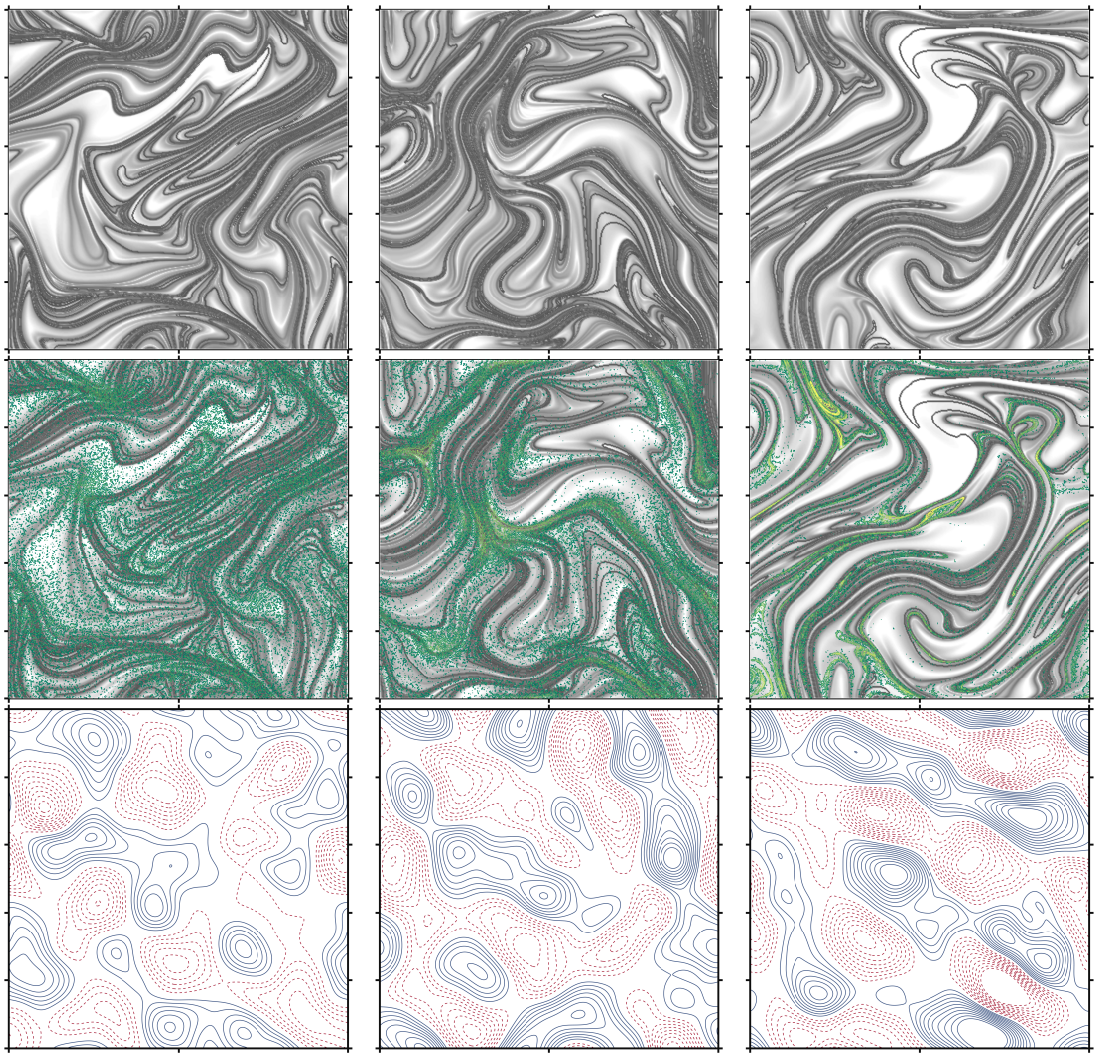

Figure 4.10: a) FTLE field at times $t = 0.5$, $t = 2.5$, and $t = 15$ (from left to right). b) Concentration contours from the non-divergence-free Taylor vortex model with concentrations ranging from $C/C_0 = 0.5$ (green) to $C/C_0 = 6$ (yellow) overlayed on the FTLE field from (a). c) Divergence field corresponding to times shown in (a) and (b). Red (dashed) contours indicate regions of divergence and blue (solid) contours indicate regions of convergence.

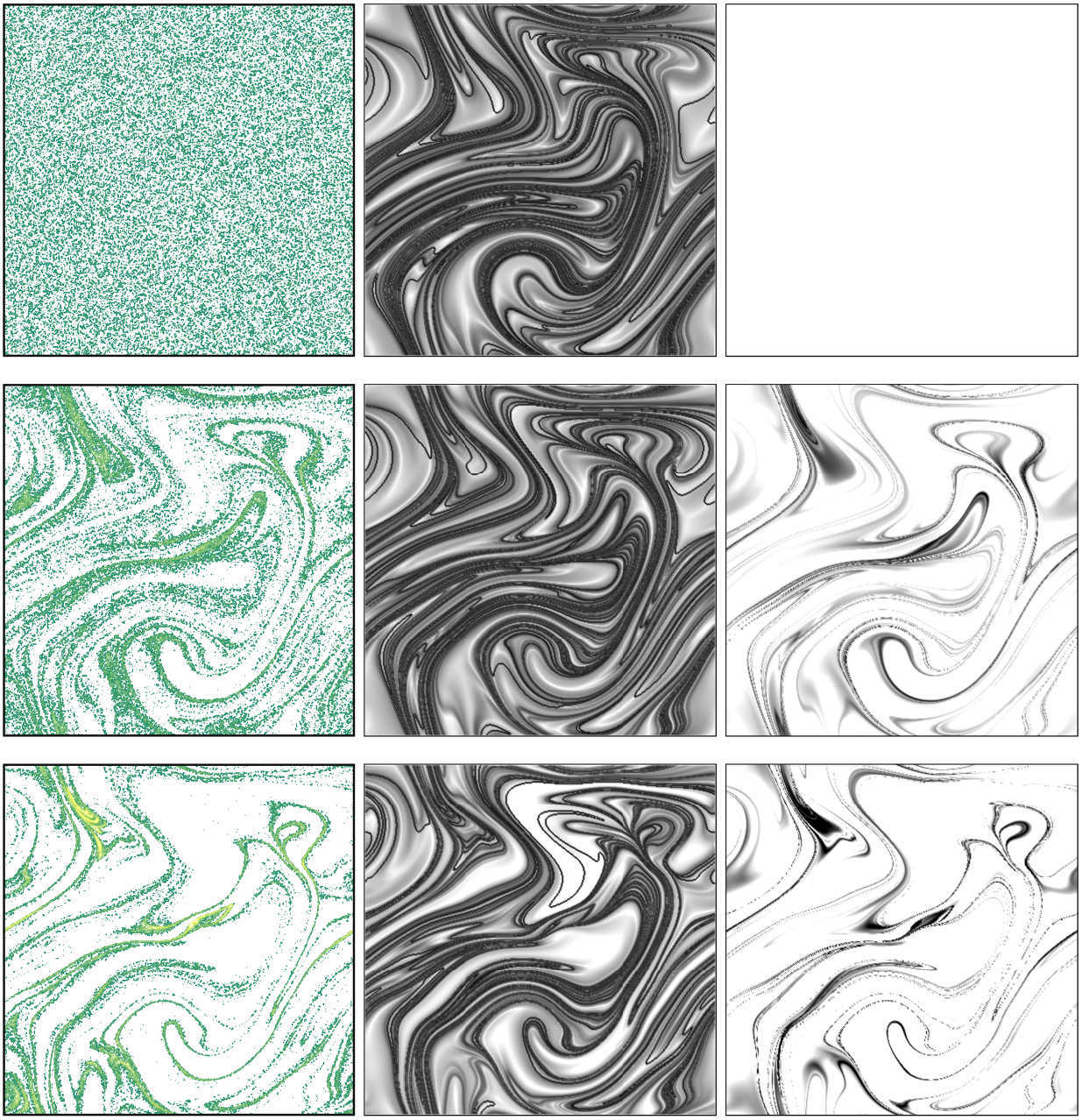

Figure 4.11: Concentration (left column), FTLE (middle column) and dilatation (right column) for a single instant of time as a function of increasing compressibility: a) $\kappa = 0$, b) $\kappa = 0.2$, and c) $\kappa = 0.4$.

of clusters on the LCS, in addition to a stretching component that subsequently stretches the clusters. Comparing the structure of the LCS in both incompressible and compressible cases, however, there is a dramatic similarity between the two. As compressibility is introduced, the dilatation

component of the LCS is strengthened while the structure remains largely unchanged. Without this dilatation component, the LCS cannot create clusters and scalars remain well-mixed.

4.5 Conclusions

Using both an experimental and numerical approach, we have demonstrated that LCS capture the dynamics of clustering in non-divergence-free flows due to the Lagrangian nature of their computation. Conversely, the divergence field is an inferior predictor for the development of voids and clusters due to the fact that it is an Eulerian computation. Eulerian metrics do not capture the complex time history of scalar transport. LCS are shown to possess both stretching and dilatation components in non-divergence-free flows that impact scalar clustering. This allows LCS to be used as a template to predict where clusters and corresponding areas of enhanced concentration will form in flows with non-divergence-free behavior.

4.6 Acknowledgments

This work was supported by the National Science Foundation (NSF) under grant PHY-1205816 to JPC. The authors thank Miguel Calpe for his assistance in coding the jet-firing algorithm and wiring of the jet array used in the turbulence tank.

Chapter 5

Non-divergence-free Flows Lead to Increased Likelihood of Reaction Enhancement

5.1 Abstract

In incompressible flows, Lagrangian coherent structures (LCS) are responsible for the coalescence of initially distant reactive scalars due to coherent stretching. This structured stirring can lead to reaction enhancements that far exceed the reaction rates of well-mixed, dilute scalars. In non-divergence-free flows, such as the free-surface of the ocean, LCS possess an additional dilatation component that results in clustering and unmixing. Using a chaotic, interacting Taylor vortex model and incorporating non-divergence-free effects, we demonstrate that the dilatation component of the LCS also increases the likelihood of observing reaction enhancement (by approximately two orders of magnitude) for scalars that were initially separated by a third non-reactive fluid. Additionally, an analytical model was developed to incorporate both stretching and dilatation in order to show that the dilatation component of the LCS facilitates filament coalescence due to fluid contraction along the LCS, thereby bringing distant filaments together and increasing reaction rates. For scalars that float on the free-surface of the ocean, such as oil and phytoplankton, these non-divergence-free effects increase the likelihood that initially distant scalars will eventually overlap in the same region of space while concentrations are still strong. While turbulent fluid flows have long been recognized as a superior means of diluting initial concentrations of scalars due to rapid stirring, the structures within these flows, especially one that is non-divergence-free, encourages scalar coalescence.

5.2 Introduction

Scalars that float on the surface of a turbulent three-dimensional fluid are transported by an effectively compressible velocity field [61, 62, 63]. While the fluid itself is incompressible, particle paths that are confined to the free-surface must be compressible since they are unable to follow fluid streamlines that have a vertical velocity component in downwelling regions. This non-divergence-free aspect of the flow leads to scalar clustering, whereby initially well-mixed scalars accumulate on the free-surface and form patches of enhanced concentrations [64, 65]. A simple example of this behavior on the free-surface of the ocean is the Langmuir circulation [66], where floating scalars (e.g., bubbles, seaweed) have been observed to aggregate in areas of down welling (convergence zone), forming long streaks on the ocean surface. These regions of enhanced concentrations can have numerous consequences, ranging from increased chemical reaction rates to altered predator/prey relations for clustering biota.

Of the studies that have looked at the transport of scalars on a turbulent free-surface, most have considered the tranport and clustering of single scalars [6] that are initialized in a well-mixed state. In this study, we are concerned with the transport and coalescence of two initially distant scalars. In this scalar topology, where two reactive scalars are seperated by a third non-reactive fluid, fluid stirring leads to reaction only if it causes the initially seperated scalars to come into contact [16, 1]. Many studies have already considered the topology where scalars share an interface, and fluid stirring instantly increases reactions due to exponential lengthening of the reaction interface [31, **?**, 11]. In many natural systems, such as the free-surface of the ocean, the initially distant topology occurs frequently, and fluid stirring must be present in order for reactions to be initiated. Examples of this topology include the fertilization of male and female gametes from broadcast spawners and the coalescence of phytoplankton blooms and pollutants (chemical spill, oil spill, plastic, etc).

5.2.1 Coalescence of initially distant scalars in divergence-free flows by LCS

Previously, both numerical [2, 5] and experimental [4] studies in incompressible flows have demononstrated that structured stirring of turbulent flows leads to coalescence events with reaction rates that can greatly exceed those predicted in a well-mixed system, a process referred to as reaction enhancement. Pratt et al. (2015) [67] demonstrated that the coalescence and reaction of concentrated filaments occurs on attracting Lagrangian coherent structures (LCS). LCS are defined as material lines or surfaces that either enhance or inhibit mixing [21, 30]. These surfaces can be either attracting or repelling in nature and are often referred to as the hidden skeleton of fluid flows because of how they shape the complex patterns of a passive tracer [23]. The persistent straining of an attracting LCS causes the contraction of initially distant filaments onto the LCS where the concentrations can be many orders of magnitude larger than in a well-mixed system. As time evolves, however, concentrations decay at an exponential rate (due to exponential stretching typically observed in chaotic flows) and the likelihood of reaction enhancement declines. Eventually, in a closed domain, scalar concentrations asymptote towards the well-mixed state.

Pratt et al. (2015) also showed that the initial placement of scalars influenced the likelihood of observing reaction enhancement. Those scalars that were placed on a repelling LCS at $t = 0$ were more likely to exhibit reaction enhancement. Repelling LCS act as barriers in flows, separating regions of the fluid and keeping segregated scalars from coalescing at early times. By initializing both scalars on a repelling LCS, there was a higher probability that scalars are on the same local branch of the manifold, which leads to early coalescence along the attracting LCS. When both scalars were not on a repelling manifold, they were potentially separated by a repelling LCS and there was a lag in the time in which these scalars could coalesce, which dramatically reduces the likelihood of reaction enhancement due to exponential decay in concentrations with time. This study expands upon Pratt et. al (2015) by including non-divergence-free effects that would typically be observed on the free-surface of the ocean.

5.2.2 Clustering of initially well-mixed scalars in non-divergence-free flows by LCS

The presence of non-divergence-free effects for buoyant scalars on a turbulent free-surface leads to unmixing and clustering, a reversal of the typical arrow of time in which turbulence acts to mix and dilute scalars. For non-steady-state turbulent free-surfaces, with downwelling and upwelling regions that are evolving rapidly in time, clustering has been shown to occur on Lagrangian coherent structures (LCS), due to the presence of a dilatation component that faciliates unmixing [54]. Therefore, in non-divergence-free flows, LCS possess both a stretching component (which is area preserving) and a dilatation component (which is not area preserving). The dilatation component is solely responsible for the clustering behavior, as stretching alone is not capable of unmixing.

For initially distant scalars in a non-divergence-free flow, coalescence events will be influenced by both of these components. Stretching will bring distant filaments together in an area-preserving manner (through exponential stretching and contraction of fluid) and dilatation will bring distant filaments together in a non-area-preserving manner (through exponential contraction of fluid). The aim of this study is to quantify whether there is an increased likelihood of reaction enhancement due to the addition of the dilatation component.

5.3 Methodology

5.3.1 Non-divergence-free Taylor vortex model

To study the effects of non-divergence-free flows, the interacting Taylor vortex model from Pratt et al. (2015) [67] was modified to include non-divergence-free behavior. This model was also utilized in Pratt et al. (2016) [**?**]. The original divergence-free model consisted of a system of interacting Taylor vortices that result in a 2D incompressible chaotic flow. A Taylor vortex centered at the origin has tangential velocity

$$u_\theta = Ur \exp\left(-\frac{r^2}{2r_0^2}\right),$$

where U is the strength of the vortex, r is the distance from its center, and r_0 is the radius of the core. The velocity field is then computed through the superposition of velocities from all vortices in the flow. The vortices move in a square doubly periodic domain with size $10r_0$. For the model, 36 vortices with a radius $r_0 = 1$ and strength $U = \pm.75$ are placed randomly in the domain; the sign of U is chosen randomly for each vortex and determines rotation direction.

Motivated by the work of Pérez-Muñuzuri [68], non-divergence-free effects are added to the model by incorporating a spatially periodic parameter, $\rho(x, y)$, that advects with and alters the velocity field of each Taylor vortex. This field is given by

$$\rho(x, y) = 1 + \kappa \sin(2\pi x/\Lambda) \sin(2\pi y/\Lambda),$$

where κ is a compressibility metric and Λ is the wavelength. For this study, $\Lambda = 5r_0$. The compressible velocity field for each Taylor vortex is then

$$u_c = \frac{u_\theta}{\rho}.$$

This alteration is repeated for all 36 vortices, and the velocity field is the superposition of these individual vorticies. Vortices are advected (by the superposed incompressible velocity at the vortex center) using a second-order improved Euler scheme. Representative snapshots of the divergence field at $t = 0$ are shown for three different compressibilities, $\kappa = 0$ (Fig. 5.1a), $\kappa = .2$ (Fig. 5.1b), and $\kappa = .4$ (Fig. 5.1c).

5.3.2 Calculating finite-time Lyapunov exponents and the dilatation rate

A standard technique for locating repelling and attracting LCS is the finite-time Lyapunov exponent (FTLE). The FTLE is a scalar field that is computed by advecting a uniform grid of tracers either forward (for repelling surfaces) or backward (for attracting surfaces) in time over an integration time T. Backward finite-time Lyapunov exponents are computed using the method of Shadden et al. [29]. A flow map $\phi_{t_0}^{t_0-T}$ is generated by advecting an initially uniform array of points (401×401) backwards from $t = t_0$ over an integration time T. Approximate derivatives of

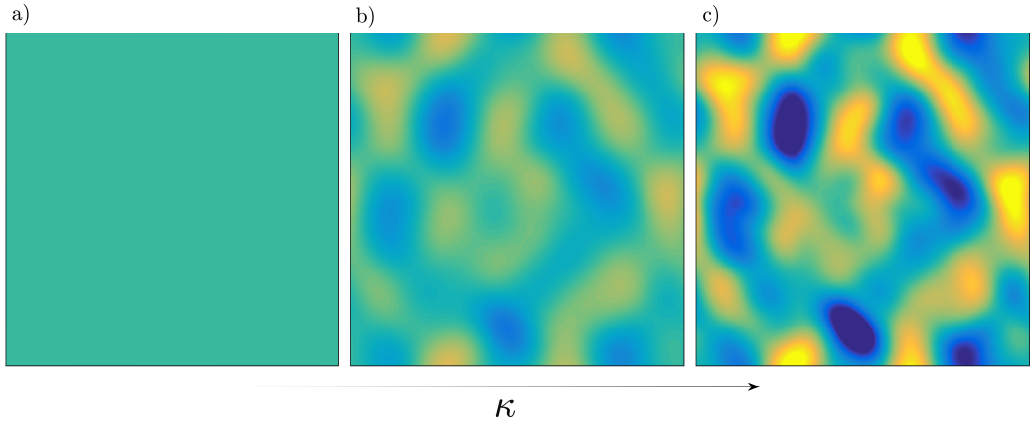

Figure 5.1: Divergence field at $t = 0$ for the incompressible divergence-free case (a) and two different compressibilities: b) $\kappa = .2$, c) $\kappa = .4$

$\phi_{t_0}^{t_0-T}$ with respect to initial conditions are computed using centered finite differences to generate the right Cauchy-Green deformation tensor

$$\Gamma = \frac{d\phi_{t_0}^{t_0-T}(\mathbf{x})}{d\mathbf{x}}^{*} \frac{d\phi_{t_0}^{t_0-T}(\mathbf{x})}{d\mathbf{x}}.$$

Finally, the FTLE is computed as

$$\sigma_{t_0}^{T}(\mathbf{x}) = \frac{1}{T} \ln\Big(\lambda_{max}(\Gamma)\Big), \tag{5.1}$$

where $\lambda_{max}(\Gamma)$ is the maximum eigenvalue of Γ. The topological ridge lines of the spatial distribution of the FTLE field correspond to attracting LCS, a region of strain which attracts nearby particle trajectories.

The Lagrangian dilatation rate is a metric that is equal to the average divergence experienced by a particle along its trajectory [54]. This is also equivalent to the rate at which material volumes are contracting or expanding over time. For incompressible flows, the dilatation rate is equal to zero, signifying an area preserving flow. Non-divergence-free flows, however, consist of regions of both expansion and contraction of fluid volumes, and therefore a non-zero dilatation rate. To compute the Lagrangian dilatation rate, a uniform grid of particles are advected backward in time for an integration time T and the integral is taken along the trajectory for each particle. The Lagrangian dilatation rate δ is then computed as

$$\delta(\mathbf{x}) = \frac{1}{T} \int_{t_0}^{t_0-T} \nabla \cdot \mathbf{u}(\mathbf{x}(\tau), \tau) d\tau. \tag{5.2}$$

In non-divergence-free flows, the FTLE field is equal to the average of the stretching and dilatation rates.

5.3.3 Calculating Reaction Rate Enhancement

Particles ($N_p = 100,000$) are advected forward in time by using the second order improved Euler method and then binned and counted to compute scalar concentrations. Reactions between scalars are computed using second order kinetics, with the reaction rate given by

$$R(x,t) = kC_1(x,t)C_2(x,t) \tag{5.3}$$

where k is the reaction rate constant, and C_1 and C_2 are the concentrations of the two scalars. For simplicity, and because we are interested fundamentally in the role of structured stirring in promoting reactant coalescence to enable reactions, we calculate reactions only in the low-Damköhler number limit, when reaction timescales are sufficiently slow relative to advective timescales that the reactions do not measurably deplete the associated reactants. [2] Because the Taylor vortex flow has a bounded domain, it is convenient to normalize the reaction rates using the steady-state rate

$$R_{ss} = kC_{1,ss}C_{2,ss}, \tag{5.4}$$

where $C_{i,ss}$ is the spatially constant, well-mixed concentration as $t \to \infty$, i.e., $C_{i,ss} = \frac{1}{A_D}\int C_i(x,0)dA$, where A_D is the area of the full domain. The reaction rate enhancement factor is then defined to be the ratio of the instantaneous, spatially averaged reaction rate to (5.4):

$$R^*(t) = \frac{1}{R_{ss}A_D}\int R(x,t)dA. \tag{5.5}$$

5.4 Results

5.4.1 Scalar coalescence on the LCS: Stretching and dilatation

Representative snapshots of the transport of two scalars (red and blue) are shown in Fig. 5.2a. As time progresses (from top to bottom), the scalars are stretched and folded and begin to overlap (purple) at some intermediate time. Due to non-divergence-free effects, the scalars do not reach a stable well-mixed state, but rather remain in a clustered state with enhanced concentrations. Fig. 5.2b shows an overlay of the FTLE field (gray) with the reaction field (purple) at the same instants of time as Fig. 5.2a. Similar to the incompressible cases discussed in Pratt et al. [67], coalescence of the initially distant scalars is occuring on the ridge lines of the FTLE field, indicators of the attracting LCS. Unlike the incompressible case, however, the dilatation field is non-zero for non-divergence-free flows. Reaction zones (purple) are overlaid on the dilatation field (gray) in Fig.5.2c, and it is evident that scalars are coalescing in the contracting regions of the flow. LCS in non-divergence-free flows, therefore, contain both a stretching component and a dilatation

component that facilitates scalar coalescence. At early times, both stretching and dilatation are responsible for scalar coalescence, while at later times, dilatation is responsible for maintaining the clustered state. This late time behavior is equivalent to the unmixing behavior that was discussed in Pratt et al. [**?**].

Due to the dilatation component of the LCS, scalar concentrations will not asymptote towards the well-mixed state, but will instead remain enhanced due to clustering, as seen in the bottom plot of Fig. 5.2a. At this time, red and blue scalars have completely overlapped in specific regions of the flow, regions where the LCS possesses a dilatation component. In non-divergence-free flows, the LCS is a scalar sink, attracting scalars from all parts of the flow. Therefore, regardless of initial scalar placement, all scalars will coalesce upon the LCS at later times while still in a clustered state (Fig. 5.3).

The convergence of initially distant scalars towards the same regions of the flow can be seen in the normalized reaction rate (Eq. 5.5) curves shown in Fig. 5.4b. While the behavior of these curves at early-intermediate times are vastly different, the curves converge as scalar filaments have collapsed on the LCS. Instead of asymptoting to the well-mixed state (as it does for the incompressible case shown in Fig. 5.4a), the scalars have organized themselves in a state where reaction enhancement is approximately 25 times greater than the well-mixed case.

5.4.2 Likelihood of Reaction Enhancement

While the long-term behavior of scalar coalescence is independent of scalar placement, early-intermediate behavior is highly sensitive to initial condition, as seen in the reaction rate curves in Fig. 5.4. Coalescence of filaments began much sooner for those curves shown in red, resulting in large reaction enhancements. For those curves shown in blue, coalescence took longer to occur, resulting in lower reaction rates. Because of this sensitivity to scalar initial conditions, Monte Carlo simulations were run to calculate the likelihood of reaction enhancement ($R^* > 1$). Initial conditions were varied randomly for each simulation and the peak reaction rate was recorded for each run. This is done for three compressibility levels; $\kappa = 0$, $\kappa = .3$, and $\kappa = .4$.

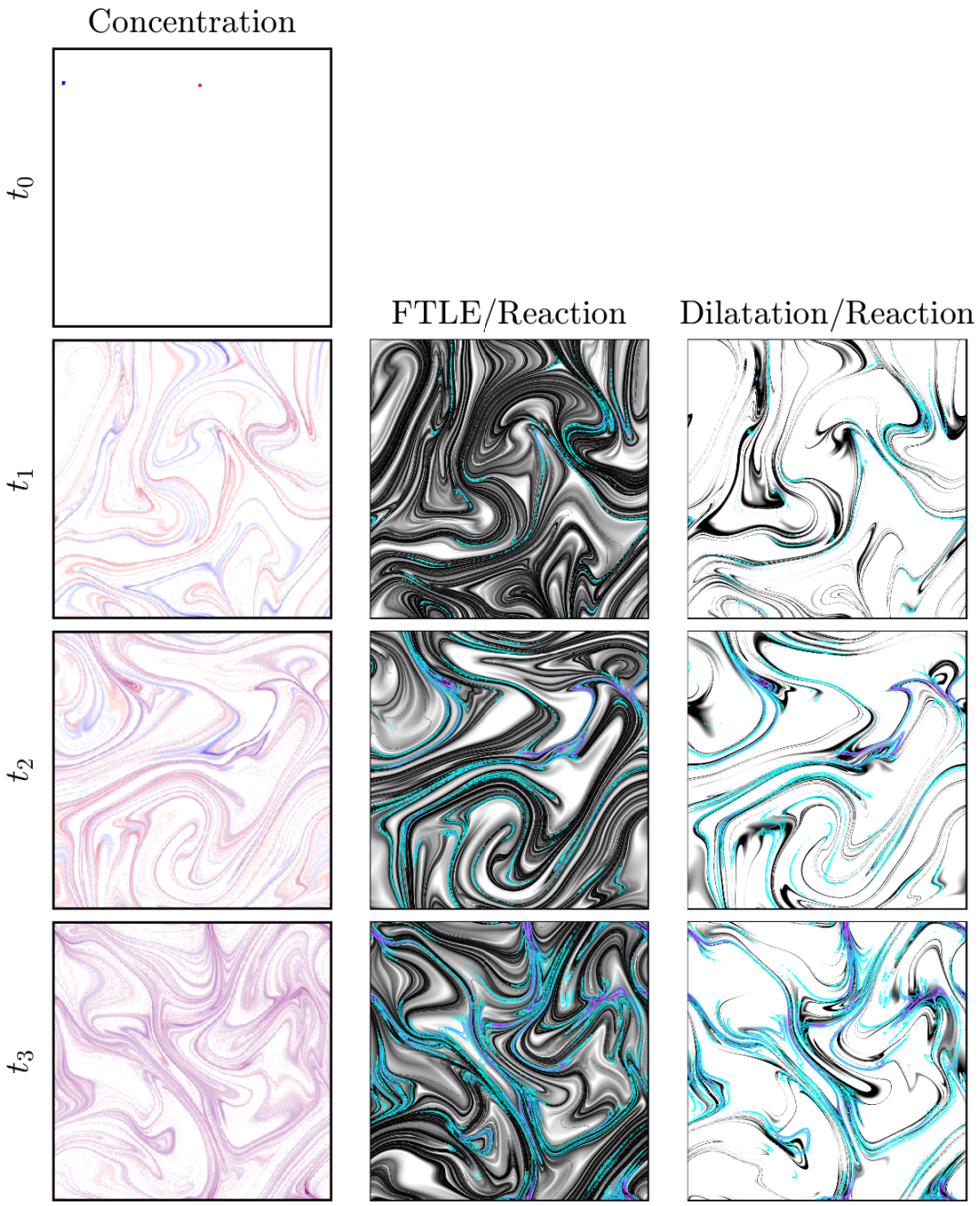

Figure 5.2: Coalescence of initially distant scalars (left) vs. time. center). Overlap of scalars on FTLE field. right) Overlap of scalars on dilatation field.

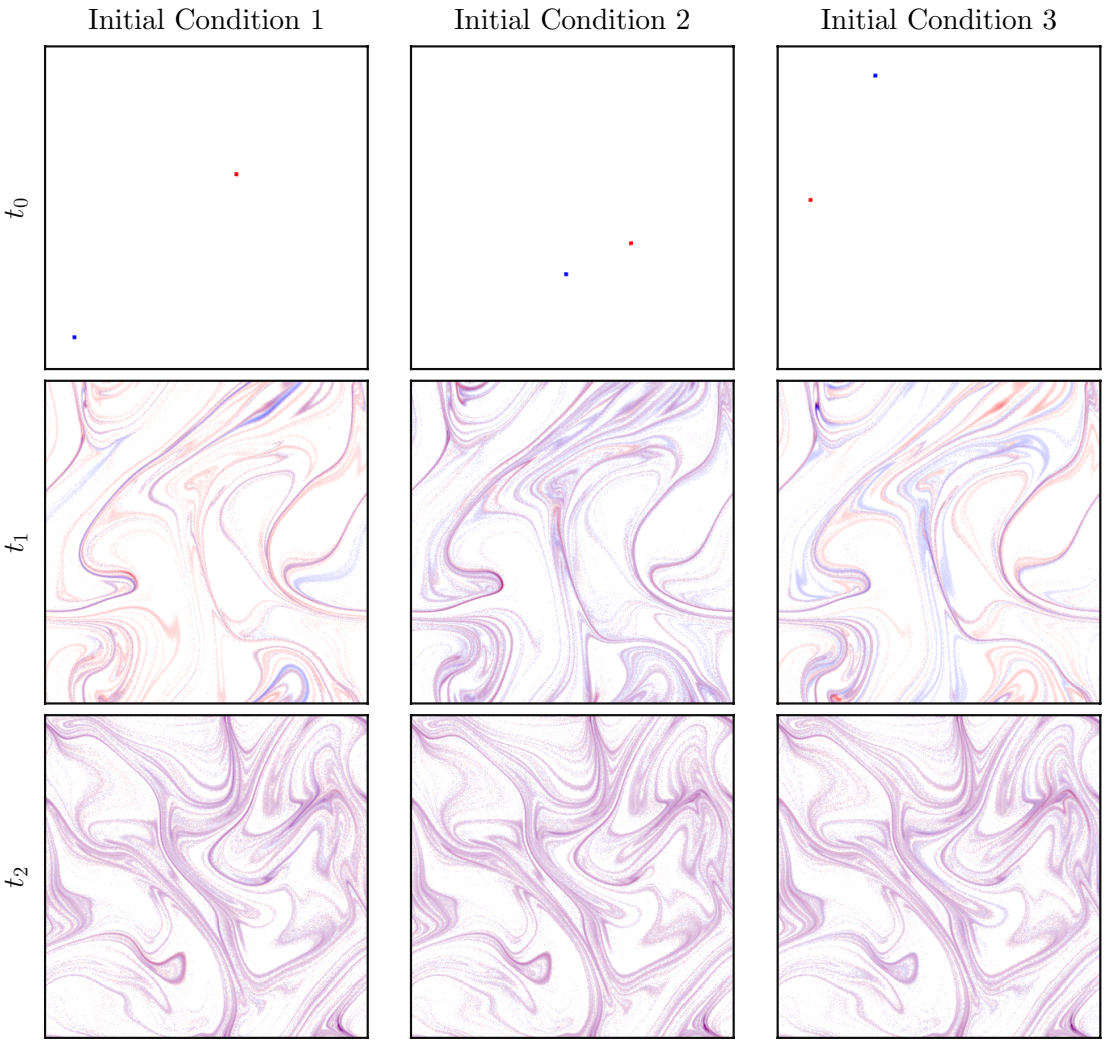

Figure 5.3: Coalescence of initially distant scalars for three different initial conditions (top).

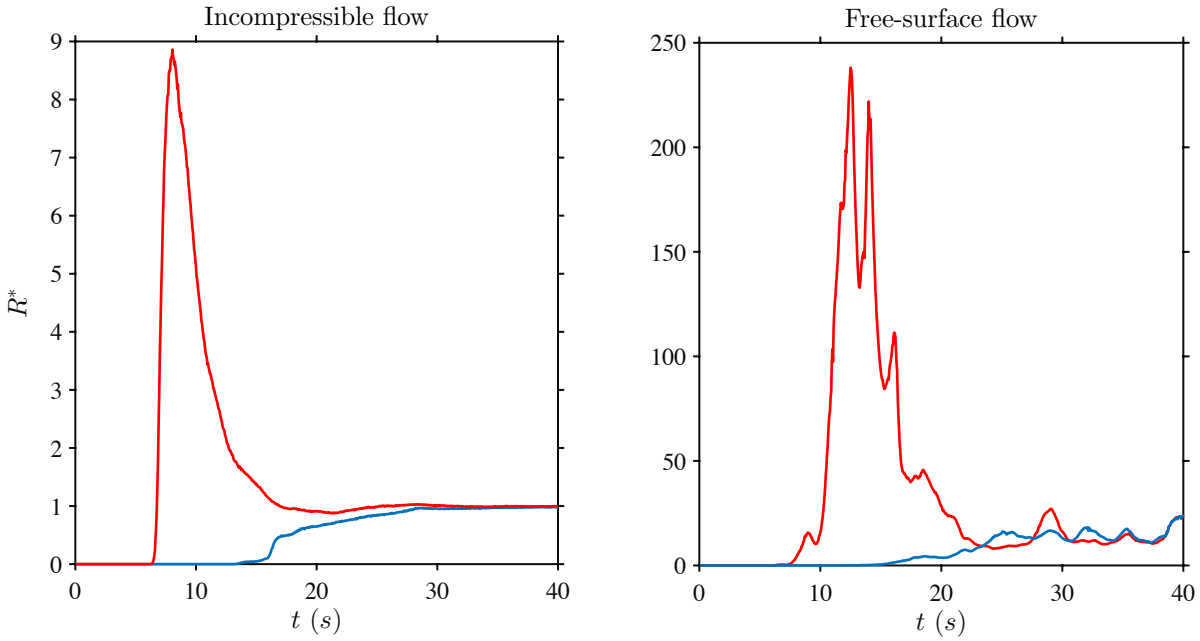

Figure 5.4: Normalized reaction rate for incompressible flow (left) and free-surface flow (right)

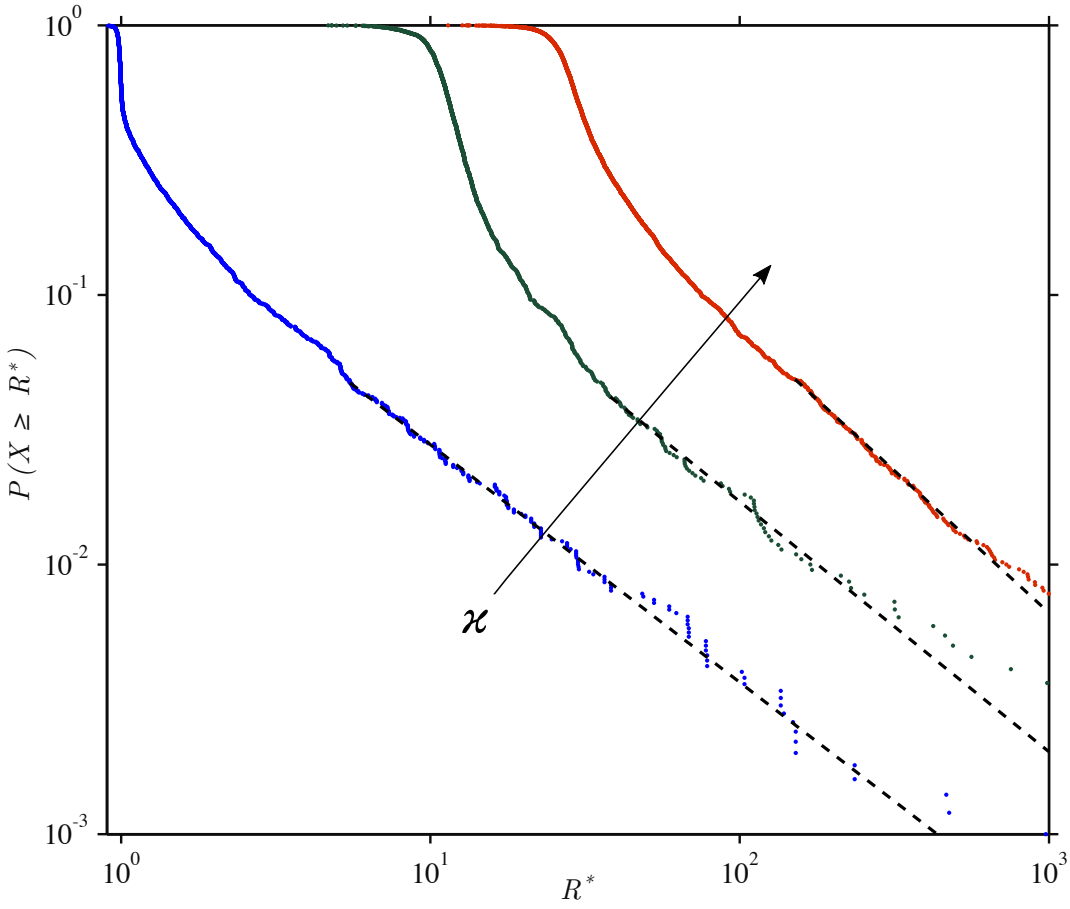

Figure 5.5: Likelihood of observing peak reaction rates for both incompressible and free-surface flow.

A CDF of peak reaction rates obtained from each simulation (Fig. 5.5) was then constructed to show the likelihood of observing reaction enhancement. Three curves are included in Fig. 5.5, each corresponding to a different compressibility. The blue curve shows the likelihood of reaction enhancement for the incompressible case. From this curve, the likelihood of observing a peak reaction rate of $R^* > 100$ is approximately .3 percent. As compressibility is gradually increased, the curves shift upwards and to the right, indicating there is a increased likelihood of observing a given reaction enhancement as compressibility is increased. For $\kappa = .3$ (green curve) the likelihood of observing $R^* > 100$ is approximately 2 percent, while for $\kappa = .4$ (red curve) the likelihood of observing $R^* > 100$ is approximately 10 percent. Therefore, for buoyant scalars floating on a turbulent free-surface, the likelihood of reaction enhancement can increase by many orders of magnitude, depending upon the strength of compressibility. Also notice that the steady state reaction rate, where $P(X \geq R^*) = 1$, also increases as compressibility is strengthened. This is indicative of the clustering that occurs in the long-term limit for non-divergence-free flows, with increased compressibility leading to more pronounced clustering and therefore increased reaction rates.

In Pratt et al. (2015) it was shown using a simple oscillating double gyre model that scalars placed on the repelling manifolds had an increased likelihood of reaction enhancement. This was repeated for this study using both the incompressible and compressible Taylor vortex model. Fig. 5.6a shows the likelihood of reaction enhancement in incompressible flows for both random initial conditions (blue curve) and those initial conditions placed on repelling LCS (purple curve). Confirming Pratt et at. (2015), there is an increased likelihood of reaction enhancement for those scalars that are initially placed on the repelling LCS. However, for the compressible case (Fig. 5.6b), there is no difference between random initial conditions (red curve) and placing scalars on the repelling LCS (purple curve). The reason for this is because in the non-divergence-free cases, the entire fluid is acting as a repelling manifold and forcing scalars on the attracting structures. Therefore, regardless of initial placement, scalars will coalesce on the attracting structures and not spend as much time being segregated by those repelling structures in the flow.

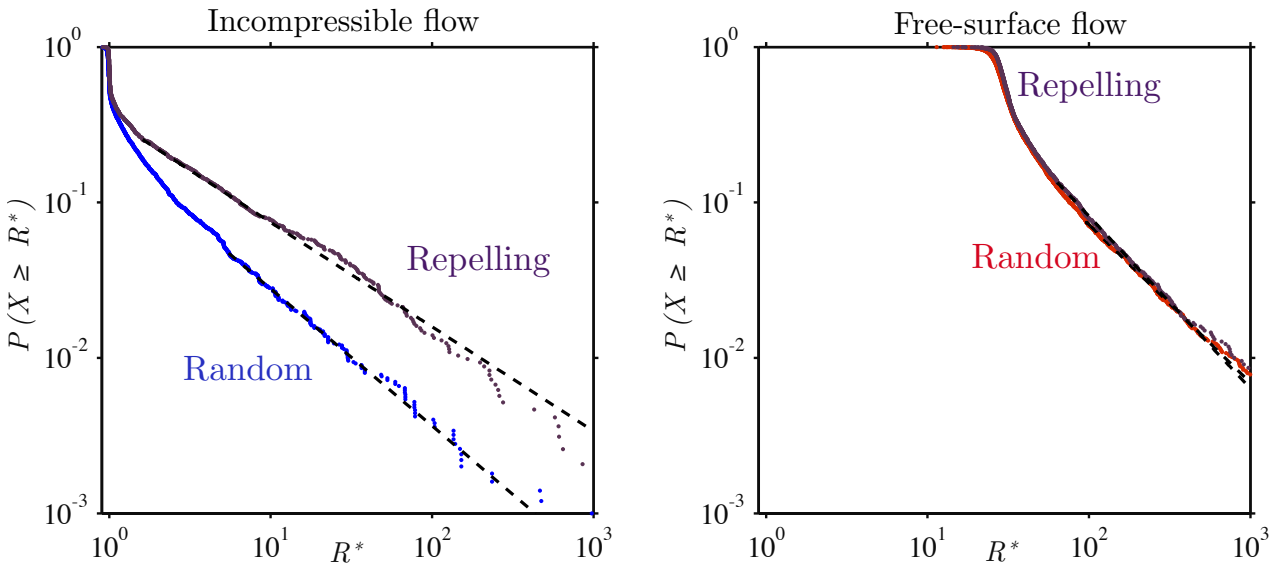

Figure 5.6: Likelihood of observing peak reaction rates for both incompressible and free-surface flow for random initial conditions and initial conditions placed on repelling manifolds ($T = 5$).

To expand upon the ideas discussed above, we now turn to an analytical model of scalar coalescence that incorporates the dilatation term.

5.4.3 Analytical Dilatation Model

The effects of dilatation on reaction enhancement can be included in the simple analytical model utilized in Pratt et. al (2015). In that model, stretching in a uniformly hyperbolic flow led to scalar coalescence as the initial separation distance between two scalars decreased at an exponential rate. The scalars themselves maintained a constant width (L_B) due to outward diffusion maintaining a stable width at the Batchelor scale. Stretching, however, leads to exponential lengthening of the scalars, which results in the area of each scalar growing as $A(t) = L_B^2 e^{\lambda t}$, and it concentration decaying as

$$C_1(t) = C_2(t) = C_0 e^{-\lambda t}.$$

This exponential decay will stop when the exponential stretching causes the scalar to fill the entire domain, i.e., the area A_D. Thus the decay is valid up to a "mixing time" when $A(t_M) = A_D$ or to

$$t_M = \frac{1}{\lambda} \log\left(\frac{A_D}{L_B^2}\right). \tag{5.6}$$

Adding a dilatation component (Δ) will not effect the concentration decay, as it only acts in the vertical direction (Fig. 5.7). Scalars will still maintain an equilibrium width due to outward diffusion.

The change in area of a fluid parcel (dotted line in Fig. 5.7) as it is advected in a non-divergence-free flow can be written as

$$\frac{DA_p}{Dt} = \int \nabla \cdot \underset{\sim}{u}\, dA_p.$$

Assuming the divergence experienced by the fluid parcel is uniform over it's area, this can be reduced to

$$\frac{DA_p}{Dt} = A_p(\nabla \cdot \underset{\sim}{u}).$$

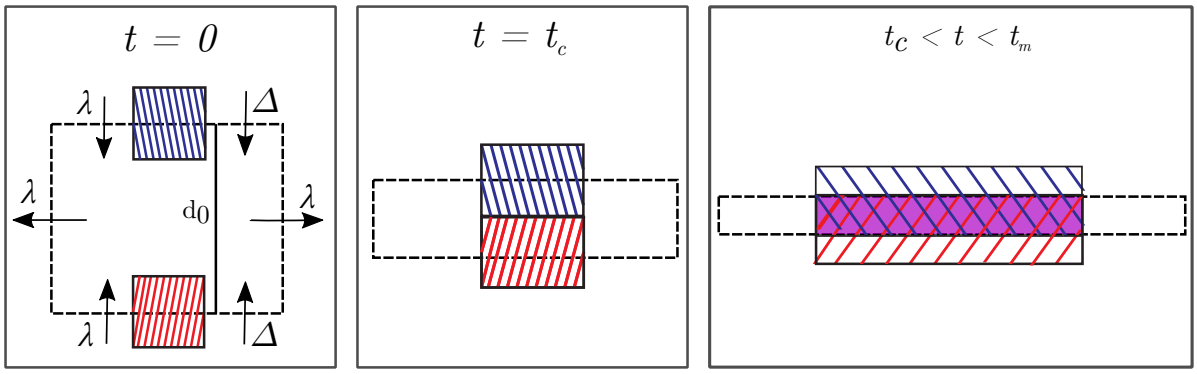

Figure 5.7: Dilatation and stretching along an LCS, resulting in the coalescence of two initially distant scalars.

Solving for $A_p(t)$;

$$A_p(t) = A_{p0} \exp\left(\int \nabla \cdot \underset{\sim}{u} \, dt \right).$$

This can be rewritten in terms of the Lagrangian dilatation rate (Δ) by substituting

$$\Delta = \frac{1}{t}\left(\int \nabla \cdot \underset{\sim}{u} \, dt \right)$$

to produce

$$A_p(t) = A_{p0} e^{-\Delta t}.$$

Assuming the fluid parcel experiences dilatation along only the transverse direction, the width decays as,

$$d(t) = d_0 e^{-\Delta t}$$

We assume that the scalars are initially separated a distance d_0 along the stable manifold (the vertical direction in Fig. 5.7), but they are at the same unstable location (i.e., there is no horizontal separation in Fig. 5.7). Given the exponential contraction in the stable direction from both uniform stretching (λ) and uniform contraction due to dilatation (Δ), the stable distance will decrease exponentially with time

$$d(t) = d_0 e^{-(\lambda+\Delta)t}. \tag{5.7}$$

When $d(t) = L_B$, the scalars come into contact; this is the "coalescence time",

$$t_C = \frac{1}{(\lambda + \Delta)} \log\left(\frac{d_0}{L_B}\right), \tag{5.8}$$

and the reaction is initiated. As the vertical distance between the centers of the scalars continues to decrease according to Eq. (5.7), they overlap, i.e., the purple/gray rectangle in Fig. 5.7. Generally, the overlap area is

$$A_o(t) = \begin{cases} 0, & 0 < t < t_C \\ L_B e^{\lambda t}(L_B - d(t)), & t_C < t < t_M \\ \frac{A_D}{L_B}(L_B - d(t)), & t_M < t \end{cases} .$$

The integrated reaction rate is thus $\int R(x,t)dA = kC_1(t)C_2(t)A_o(t)$. Since the steady state reaction rate is $R_{ss} = k(C_0 L_B^2/A_D)^2$, then the normalized rate becomes

$$R^*(t) = \begin{cases} 0, & 0 < t < t_C \\ e^{\lambda(t_M - t)}(1 - e^{-(\lambda+\Delta)(t-t_C)}), & t_C < t < t_M \\ 1 - e^{-(\lambda+\Delta)(t-t_C)}, & t_M < t \end{cases} . \tag{5.9}$$

The peak normalized reaction rate (R^*_{max}) can also be computed,

$$R^*_{max} = e^{\lambda(t_m - t_{max})}\left[1 - e^{-(\lambda+\Delta)(t_{max} - t_c)}\right] \tag{5.10}$$

where

$$t_{max} = \frac{1}{\lambda + \Delta}\left[\Delta t_c + \lambda t_c + \log\left(2 + \frac{\Delta}{\lambda}\right)\right]$$

In the pure stretching case, the exponential decay in separation distance between scalars is matched by a corresponding exponential decay in concentrations, since filament widths are lengthening exponentially. Through the addition of a dilatation term in Eq. 5.9, the rate at which scalars coalesce is increased (by a factor of $e^{-\Delta t}$) but concentrations remain unaffected. Therefore, by increasing the rate at which scalars coalesce, concentrations have not decayed as quickly and reaction rates increase due to the added dilatation term. This is observed in the curves of Fig. 5.8. As the strength of dilatation is gradually increased, the coalescence time decreases, and the reaction rates correspondingly increase. Dilatation, therefore, facilitates the coalescence of filaments onto LCS

which leads to significantly enhanced reaction rates compared to incompressible, divergence-free flows where there is no dilatation term.

5.5 Discussion

Composed of both a stretching and dilatation component, LCS facilitate the coalescence and clustering of initially distant scalars in non-divergence-free flows. This has ramifications for a variety of scalars that are transported and dispersed on the free-surface of the ocean. For example, beneficial blooms of buoyant phytoplankton, which play significant roles in oceanic biogeochemical cycles can more readily overlap with buoyant toxic spills due to contraction of distant filaments onto LCS before filament concentrations have had time to dilute due to turbulent stirring. With the likelihood of reaction enhancement increasing by two orders of magnitude, these non-divergence-free effects may help explain why broadcasting corals, whose gametes are released into the water column, have evolved to release buoyant gametes that fertilize on the ocean surface.

5.6 Acknowledgments

This work was supported by the National Science Foundation (NSF) under grant PHY-1205816 to JPC.

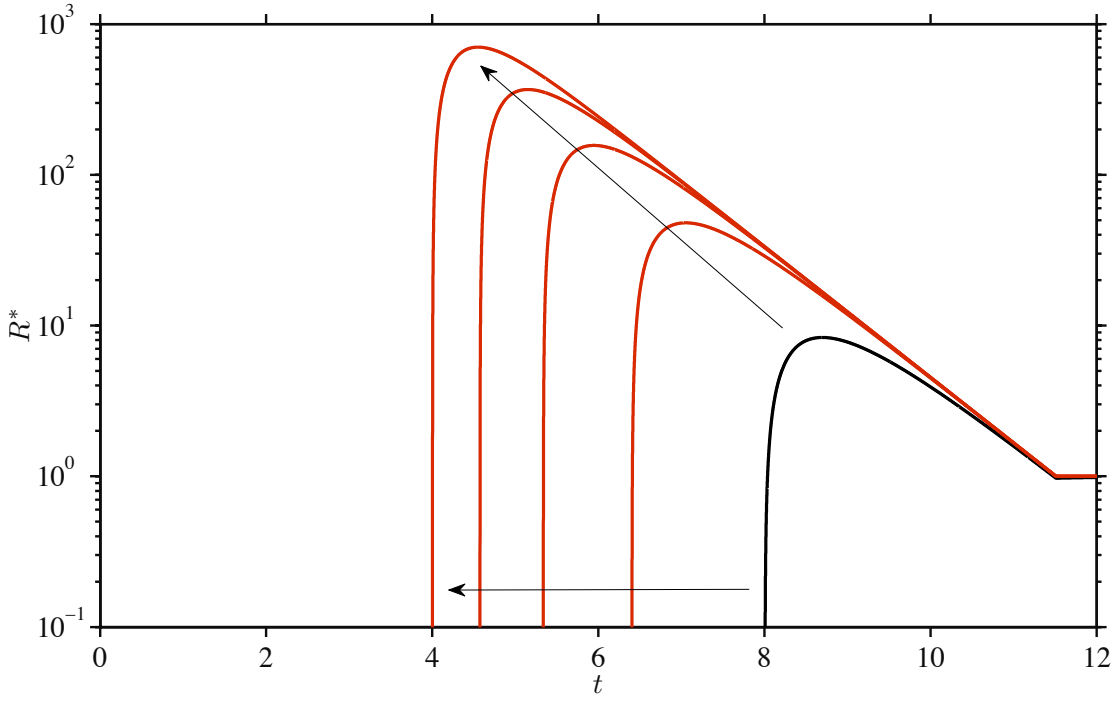

Figure 5.8: Reaction enhancement as a function of increased dilatation: $\Delta/\lambda = 0$,$\Delta/\lambda = .25$, $\Delta/\lambda = .5$,$\Delta/\lambda = .75$,$\Delta/\lambda = 1$. Initial separation distance $d_0/L_0 = 3000$. Area of domain, $A = 10$. x-axis is t/λ not t.

Chapter 6

Conclusions

6.1 Diffusion v. Structured Stirring

As a recap of previous chapters, the list below consists of the main findings from each chapter.

(1) Chapter 2

- Separation distance is the only factor that determines the magnitude of reaction enhancement in a pure diffusive flow.
- Beyond a certain separation distance, reaction enhancement was not possible.
- For randomly placed scalars, the likelihood of reaction enhancement had power law behavior with $p(R^*) \propto R^{*-2}$.

(2) Chapter 3

- Lagrangian coherent structures are responsible for the coalescence of initially distant scalars.
- For certain initial conditions, this coalescence could occur at a timescale quicker than that of dilution, thereby promoting reaction enhancement.
- Placement of scalars on repelling LCS was shown to increase the likelihood of scalar coalescence due to facilitating the time in which scalars coalesced.

(3) Chapter 4

- Scalars that float on the free-surface of a 3D turbulent fluid are able to unmix, forming clusters of enhanced concentrations.
- Lagrangian coherent structures possess a dilatation component that results in clustering and unmixing. Therefore, clusters form on the LCS.
- The divergence field is unable to capture the long term behavior of clustering because it is an Eulerian quantity. The LCS is best suited for this because it naturally has a time history.

(4) Chapter 5

- Regardless of initial placement, scalars will cluster on the LCS in the long-term limit.
- There is an increased likelihood of reaction enhancement of initially distant scalars in non-divergence-free flows compared to divergence-free flows.
- The dilatation component of the LCS facilitates scalar coalescence and reaction rates as it is able to bring distant filaments together without decaying concentrations.

By observing the likelihood of reaction enhancement for pure diffusive mixing, structured stirring, and structured stirring in non-divergence-free environments, we can begin to infer the importance of structure in turbulent flows. Fig. 6.1 shows the likelihood of reaction enhancement for these various cases. The black solid line indicates the likelihood of reaction enhancement for randomly placed scalars through diffusive mixing. The green curve is from the Taylor vortex flow with random initial conditions. It is evident that these curves fall on top of one another. Therefore, for randomly placed scalars, structured stirring does not seem to increase the likelihood of reaction enhancement. This does not mean, however, that the coalescence processes are the same.

In turbulent stirring, scalars can be initially close but separated by a repelling manifold. This manifold will keep scalars segregated as their concentrations continue to decay exponentially, resulting in a low likelihood of reaction enhancement. In a diffusive system, these initially close scalars will coalesce quickly, as there is no structure that impedes coalescence. The opposite,

however, is true for initially distant scalars that are further apart. The lack of structure in random diffusion means that distant scalars will have been sufficiently diluted by the time overlap occurs, making reaction enhancement impossible. In structured stirring, however, the presence of LCS can facilitate the coalescence of these scalars, increasing the likelihood of reaction enhancement. It is these trade offs that likely lead to the collapse of the two curves.

In many biological systems, such as broadcasting corals, there is a natural patchiness that exists. This indicates that there is a minimum separation distance that limits closer, more compact conditions. In limiting these compact placements, the large reaction rates that are observed in the pure diffusion case are negated. To investigate the impact of patchiness, separation distances are restricted below some threshold distance, as shown in the left plot of Fig 6.2. The likelihood of reaction enhancement in these "patchy" conditions for pure diffusion is shown in the center plot of Fig 6.2, for a variety of separation restrictions. As the minimum separation distance is gradually increased, the likelihood of reaction enhancement decreases, as the curves peel away from the zero threshold line and no longer resemble a power law as they do in the random case (solid blue line). To show the importance of structured stirring, a Monte Carlo simulation with restricted initial separation distances ($d/L_{max} \geq .28$) is run for the Taylor vortex flow. The likelihood of reaction enhancement is indicated by the red dots in the right plot of Fig. 6.2. Comparing this to the same threshold ($d/L_{max} \geq .28$) for the pure diffusion case (solid maroon line), the likelihood of reaction enhancement is much greater for the structured stirring case. This confirms that for far enough separation distances, structured stirring will far outperform unstructured diffusive mixing.

Additionally, by placing scalars intelligently on the repelling LCS, we can avoid the issue of segregation that significantly decreases the likelihood of reaction enhancement. The red curve of Fig. 6.1 shows the likelihood of reaction enhancement for scalars that were randomly placed on the repelling manifold. The likelihood increased by an order of magnitude. By taking advantage of the structure of turbulent flows, we can significantly increase the likelihood of observing reaction enhancement.

Finally, to increase the likelihood of reaction enhancement further, we can transition from an incompressible flow to a free-surface flow that has non-divergence-free effects, such as the surface of the ocean. For scalars placed randomly in a non-divergence-free flow (blue curve), the likelihood increased by approximately two orders of magnitude. This may be one reason why broadcasting corals have evolved to release buoyant gametes that are transported on the ocean surface. Rather than having to fertilize in a 3D incompressible fluid, corals can increase the likelihood of fertilization by releasing buoyant gametes that are transported in a 2D compressible fluid.

We began this thesis with the words of Vincent Van Gogh contemplating how he should begin painting all of the intricacies that he saw in the night sky. Science works in much the same way. How does one even begin to untangle something as complicated as a chaotic, turbulent flow? This thesis attempts to add color to a black and white painting, but of course the painting is never complete. There are more complex models, more sophisticated experiments, and more abstract theory that can be utilized to add layers to our painting. Large eddy simulation will add more elaborate brush strokes, three dimensional models will add depth, and additional experiments will add the necessary sheen. In the end, we know a little bit more about how the world works, and then we move on to the next painting.

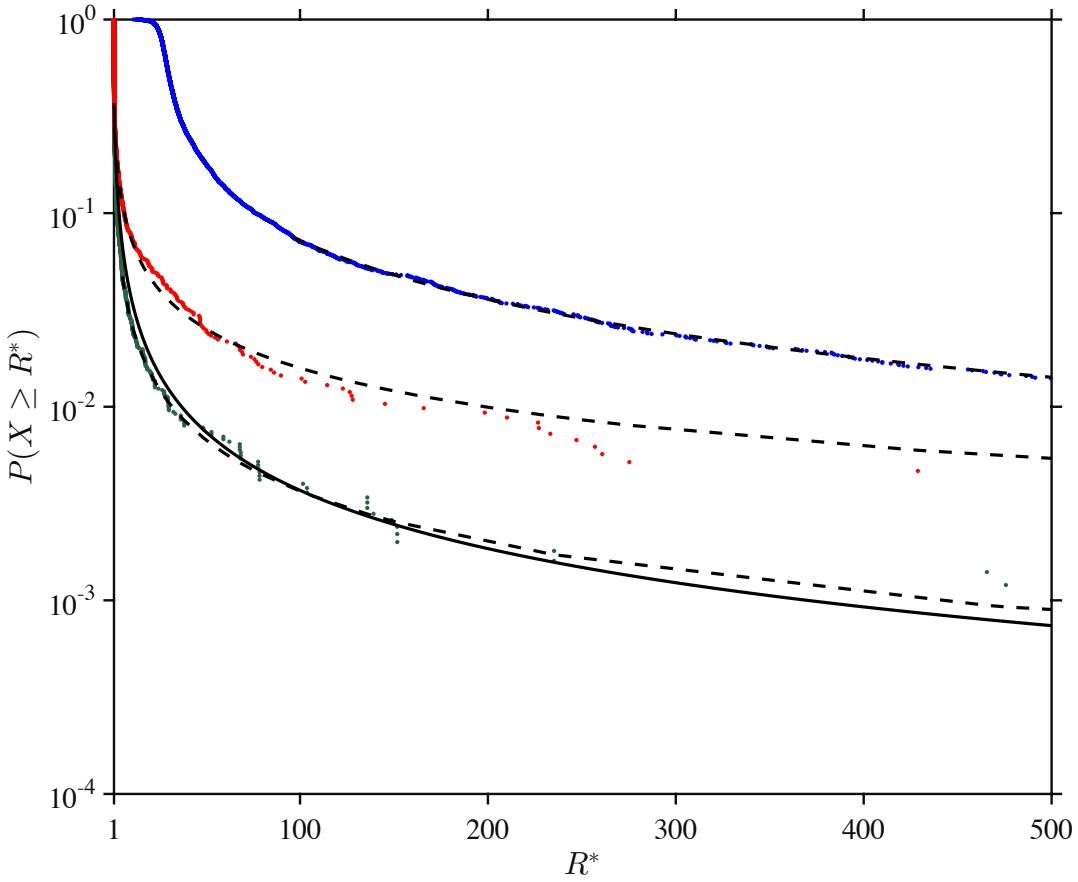

Figure 6.1: Likelyhood of reaction enhancement for pure diffusion with random initial conditions (solid black line), structured stirring with random initial conditions (green line), structured stirring with initial conditions placed on repelling manifolds (red line) and structured stirring in a non-divergence-free flow with random initial conditions.

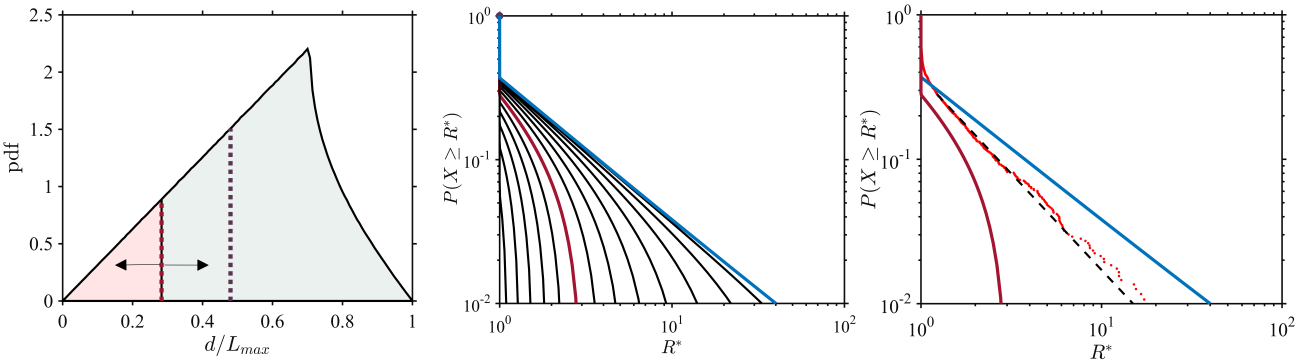

Figure 6.2: left) Limiting placement of scalars less than a given seperation distance. center) Likelyhood of reaction enhancement as seperation distances become more restrictive. The colored solid lines in the left, center, and right plots are for the same restrictive seperation distances; $d/L_{max} \geq .28$ (maroon) and $d/L_{max} \geq 0$ (blue). right) Likelyhood of reaction enhancement for $d/L_{max} \geq .28$ from the Taylor vortex flow overlayed on the colored curves from the center plot.

Bibliography

[1] J.P. Crimaldi and Browning H.S. A proposed mechanism for turbulent enhancement of broadcast spawning efficiency. J. Mar. Syst., 49:3–18, 2004.

[2] J.P. Crimaldi, J.R. Cadwell, and J.B. Weiss. Reaction enhancement of isolated scalars by vortex stirring. Phys. Fluids, 20(7):073605, 2008.

[3] M.A. Soltys, and J.P. Crimaldi. Scalar interactions between parallel jets measured using a two-channel PLIF technique. Exp Fluids,50(6):1625–1632, 2011.

[4] M. Soltys and J. Crimaldi. Joint Probabilities and Mixing of Isolated Scalars Emitted from Parallel Jets. J. Fluid Mech., DOI 10.1017/jfm.2015.113, 2015.

[5] J.P Crimaldi and T.R. Kawakami. Reaction of initially distant scalars in a cylinder wake. Phys. Fluids, 25:053604, 2013.

[6] E.R. Abraham. The generation of plankton patchiness by turbulent stirring. Nature, 391:577–580, 1998.

[7] N. Peters. Turbulent Combustion. Cambridge: Cambridge University Press, 2000.

[8] J.M. Ottino. Mixing, Chaotic Advection, and Turbulence. Annu. Rev. Fluid Mech., 22:207–253, 1990.

[9] H. Aref. Stirring by chaotic advection. J. Fluid Mech., 143:1–21, 1984.

[10] F.J. Muzzio and M. Liu. Chemical reactions in chaotic flows. Chem. Eng. J., 64:117–127, 1996.

[11] G. Károlyi. Effective dimensions and chemical reactions in fluid flows. Phys. Rev. E, 76:046315, 2007.

[12] G. Károlyi, Á. Péntek, Z. Toroczkai, T. Tél, and C. Grebogi. Chemical or biological activity in open chaotic flows. Phys. Rev. E, 59:5468–5481, 1999.

[13] Y. Tsang. Predicting the evolution of fast chemical reactions in chaotic flows. Phys. Rev. E, 80:026305, 2009.

[14] Z. Toroczkai, G. Károlyi, Á. Péntek, T. Tél, and C. Grebogi. Advection of Active Particles in Open Chaotic Flows. Phys. Rev. Let., 80(3):500–503, 1998.

[15] G. Károlyi, T. Tél, A. de Moura, and C. Grebogi. Reactive Particles in Random Flows. Phys. Rev. Let., 92(17):174101–1:4, 2004.

[16] J.P. Crimaldi and R.K. Zimmer. The physics of broadcast spawning in benthic invertebrates. Annu. Rev. Mar. Sci., 6:141–165, 2014.

[17] E. Franco, D. Pekarek, J. Peng, and J. Dabiri. Geometry of unsteady fluid transport during fluid-structure interactions. J. Fluid Mech., 589:125–145, 2007.

[18] M. Soltys and J. Crimaldi. Joint Probabilities and Mixing of Isolated Scalars Emitted from Parallel Jets. J. Fluid Mech., DOI 10.1017/jfm.2015.113, 2015.

[19] P. Holmes, Lumley J.L., G. Berkooz, and Rowley C.W. Coherent Structures, Dynamical Systems and Symmetry. Cambridge: Cambridge University Press, 2012.

[20] G. Haller and G. Yuan. Lagrangian coherent structures and mixing in two-dimensional turbulence. Physica D, 147(3-4):352–370, 2000.

[21] T. Peacock and J. Dabiri. Introduction to Focus Issue: Lagangian Coherent Structures. Chaos, 20:017501, 2010.

[22] M. Farazmand and G. Haller. Computing Lagrangian Coherent Structures from their variational theory. Chaos, 22:013128, 2012.

[23] T. Peacock and Haller G. Lagrangian Coherent Structures: The hidden skeleton of fluid flows. Physics Today, 66(2):41–46, 2013.

[24] T. Tél, A. de Moura, C. Grebogi, and G. Károlyi. Chemical and biological activity in open flows: A dynamical system approach. Phys. Rep., 413:91–196, 2005.

[25] F. Lekien, C. Coulliette, A.J. Mariano, E.H. Ryan, L.K. Shay, G. Haller, and J. Marsden. Pollution release tied to invariant manifolds: A case study for the coast of Florida. Physica D, 210:1–20, 2005.

[26] C.S. Harrison, D.A. Siegel, and S. Mitarai. Filamentation and eddy-eddy interactions in marine larval accumulation and transport. Mar Ecol Prog Ser, 472:27–44, 2013.

[27] E. Tew Kai, V. Rossi, J. Sudre, H. Weimerskirch, C. Lopez, E. Hernandez-Garcia, F. Marsac, and V. Garçon. Top marine predators track Lagrangian coherent structures. Proc. Nat. Acad. Sci., 106(20):8245–8250, 2009.

[28] Z. Neufeld and E. Hernández-García. Chemical and Biological Processes in Fluid Flows: A Dynamical Syste Imperial College Press, 2009.

[29] S.C. Shadden, F. Lekien, and J.E. Marsden. Definition and properties of Lagrangian coherent structures from finite-time Lyapunov exponents in two-dimensional aperiodic flows. Physica D, 212(3-4):271–304, 2005.

[30] G. Haller. Lagrangian Coherent Structures. Annu. Rev. Fluid Mech., 47:137–161, 2015.

[31] T.S. Tél, G. Károlyi, A. Péntek, Z. Toroczkai, C. Grebogi, and J. Kadtke. Chaotic advection, diffusion, and reactions in open flows. Chaos, 10:89–98, 2000.

[32] A.E. Perry, M.S. Chong, and T.T. Lim. The vortex-shedding process behind two-dimensional bluff bodies. J. Fluid Mech., 116:77–90, 1982.

[33] D.F. Carlson, E. Fredj, H. Gildor, and V. Rom-Kedar. Deducing an upper bound to the horizontal eddy diffusivity using a stochastic Lagrangian model. Envrion. Fluid Mech., 10:499–520, 2010.

[34] H. Aref. Point vortex dynamics: A classical mathematics playground. J. Math. Phys., 48:065401, 2007.

[35] R.L. Panton. Incompressible Flow. John Wiley Sons, Inc, 1996.

[36] A. Clauset, C.R. Shalizi, and M.E.J. Newman. Power law distributions in empirical data. SIAM Review, 51:661–703, 2009.

[37] D. Bargteil and T. Solomon. Barriers to front propagation in ordered and disordered vortex flows. Chaos, 22:037103, 20012.

[38] G.K. Batchelor. Small-scale variation of convected quantities like temperature in turbulent fluid. Fluid Mechanics, 5(1):113–133, 1959.

[39] H. Aref, J.R. Blake, M. Budišić, J.H.E. Cartwright, H.J.H. Clercx, U. Feudel, R. Golestanian, E. Gouillart, Y.L. Guer, G.F. van Heijst, et al. Frontiers of chaotic advection. arXiv preprint arXiv:1403.2953, 2014.

[40] G. Károlyi and T. Tél. Chemical Transients in Closed Chaotic Flows: The Role of Effective Dimensions. Phys. Rev. Let., 95:264501, 2005.

[41] E. Szalai, M. Alvarez, and F. Muzzio. Laminar Mixing: A dynamical systems approach, in Handbook of Indus
John Wiley and Sons Inc., 2003.

[42] Cressman J.R., J. Davoudi, W.I. Goldburg, and J. Schumacher. Eulerian and Lagrangian studies in surface flow turbulence. New J. Physics, 6, 2004.

[43] J. Schumacher and B. Eckhardt. Clustering dynamics of Lagrangian tracers in free-surface flows. Phys. Rev. E, 66:017303, 2002.

[44] J.C. Sommerer and E. Ott. Particles floating on a moving fluid: A dynamically comprehensible physical fractal. Science, 259:335–339, 1993.

[45] S. Leibovich. The form and dynamics of Langmuir circulations. Ann. Rev. Fluid Mech., 15:391–427, 1983.

[46] P.A. Davidson. Turbulence: An introduction for scientists and engineers. Oxford University Press, 1999.

[47] G. Boffetta, J. Davoudi, B. Eckhardt, and J. Schumacher. Lagrangian tracers on a surface flow: The role of time correlations. Phys. Rev. Lett., 93:134501, 2004.

[48] J.K. Eaton and J.R. Fessler. Preferential concentration of particles by turbulence. Int. J. Multiphase Flow, 20:169–209, 1994.

[49] W.M. Durham, E. Climent, M. Barry, F. De Lillo, G. Boffetta, M. Cencini, and R. Stocker. Turbulence drives microscale patches of motile phytoplankton. Nature Comm., 212(4):2148, 2013.

[50] J. Larkin, W. Goldburg, and M.M. Bandi. Time evolution of a fractal distribution: Particle concentrations in free-surface turbulence. Physica D, 239:1264–1268, 2010.

[51] J. Larkin, M.M. Bandi, A. Pumir, and W.I. Goldburg. Power-law distributions of particle concentration in free-surface flows. Phys. Rev. E, 80:066301, 2009.

[52] J. Larkin and W. Goldburg. Decorrelating a compressible turbulent flow: An experiment. Phys. Rev. E., 82:016301, 2010.

[53] S. Lovecchio, C. Marchioli, and A. Soldai. Time persistence of floating-particle clusters in free-surface turbulence. Phys. Rev. E., 88:033003, 2013.

[54] H.S. Huntley, B.L. Lipphardt Jr, G. Jacobs, and A.D. Kirwan Jr. Clusters, deformation, and dilation: Diagnostics for material accumulation regions. Journal of Geophysical Research: Oceans, 120:6622–6636, 2015.

[55] V. Pérez-Muñuzuri. Mixing and clustering in compressible chaotic stirred flows. Phys. Rev. E, 89:022917, 2014.

[56] K.R. Pratt, J.D. Meiss, and J.P. Crimaldi. Reaction enhancement of initially distant scalars by Lagrangian coherent structures. Phys. Fluids, 27, 2015.

[57] E.A. Variano and Cowen E.A. A random-jet-stirred turbulence tank. J. Fluid Mech, 604:1–32, 2008.

[58] R. Monchaux, M. Bourgoin, and A. Cartellier. Preferential concentration of heavy particles: A Voronoï analysis. Phys. Fluids, 22:103304, 2010.

[59] J.R. Fessler, J.D. Kulick, and J.K. Eaton. Preferential concentration of heavy particles in a turbulent channel flow. Phys. Fluids, 6:3742, 1994.

[60] R. Monchaux, M. Bourgoin, and A. Cartellier. Analyzing preferential concentration and clustering of inertial particles in turbulence. International Journal of Multiphase Flow, 40:1–18, 2012.

[61] G. Boffetta, J. Davoudi, B. Eckhardt, and J. Schumacher. Lagrangian tracers on a surface flow: The role of time correlations. Phys. Rev. Lett., 93:134501, 2004.

[62] J. Schumacher and B. Eckhardt. Clustering dynamics of Lagrangian tracers in free-surface flows. Phys. Rev. E, 66:017303, 2002.

[63] J.C. Sommerer and E. Ott. Particles floating on a moving fluid: A dynamically comprehensible physical fractal. Science, 259:335–339, 1993.

[64] Cressman J.R., J. Davoudi, W.I. Goldburg, and J. Schumacher. Eulerian and Lagrangian studies in surface flow turbulence. New J. Physics, 6, 2004.

[65] J. Larkin, M.M. Bandi, A. Pumir, and W.I. Goldburg. Power-law distributions of particle concentration in free-surface flows. Phys. Rev. E, 80:066301, 2009.

[66] S. Leibovich. The form and dynamics of Langmuir circulations. Ann. Rev. Fluid Mech., 15:391–427, 1983.

[67] K.R. Pratt, J.D. Meiss, and J.P. Crimaldi. Reaction enhancement of initially distant scalars by Lagrangian coherent structures. Phys. Fluids, 27, 2015.

[68] V. Pérez-Muñuzuri. Mixing and clustering in compressible chaotic stirred flows. Phys. Rev. E, 89:022917, 2014.

[69] T. Sapsis and G. Haller. Clustering criterion for inertial particles in two-dimensional time-periodic and three-dimensional steady flows. Chaos, 20:017515, 2010.

[70] M. Sudharsan and S.L. Brunton and J.J. Riley Lagrangian coherent structures and inertial particle dynamics. Phys. Rev. E, 93:033108, 2016.

[71] V. Pérez-Muñuzuri. Clustering of inertial particles in compressible chaotic flows. Phys. Rev. E, 91:052906, 2015.